Received: 9 April 2019 | Revised: 19 February 2020 | Accepted: 1 April 2020

DOI: 10.1111/jmg.12531

ORIGINAL ARTICLE

Journal of METAMORPHIC GEOLOGY WILEY

Coupling of *P–T–t–D* histories of eclogite and metagreywacke—Insights to late Ordovician–Silurian crustal folding events recorded in the Beishan Orogen (NW China)

Jérémie Soldner[1,2] | **Pavla Štípská**[3,4] | **Karel Schulmann**[3,4] | **Chao Yuan**[1] | **Robert Anczkiewicz**[5] | **Dariusz Sala**[5] | **Yingde Jiang**[1] | **Yunying Zhang**[6] | **Xinyu Wang**[1]

[1]State Key Laboratory of Isotope Geochemistry, Guangzhou Institute of Geochemistry, Chinese Academy of Sciences, Guangzhou, China

[2]University of Chinese Academy of Sciences, Beijing, China

[3]Institut de Physique du Globe de Strasbourg, UMR 7516, University of Strasbourg/EOST, CNRS, Strasbourg, France

[4]Center for Lithospheric Research, Czech Geological Survey, Praha 1, Czech Republic

[5]Institute of Geological Sciences, Polish Academy of Sciences, Kraków, Poland

[6]Department of Earth Sciences, The University of Hong Kong, Hong Kong, China

Correspondence
Jérémie Soldner, State Key Laboratory of Isotope Geochemistry, Guangzhou Institute of Geochemistry, Chinese Academy of Sciences, Guangzhou, China.
Email: jeremie.soldner@gmail.com

Funding information
Guangdong Special Support Program; National Natural Science Foundation of China, Grant/Award Number: 41573025 and 41711530147; Grantová Agentura České Republiky EXPRO, Grant/Award Number:GACR 19-27682X; CNRS-NSFC, Grant/Award Number: PRC1413; National Key R&D Program of China, Grant/Award Number: 2017YFC0601205-2; International Partnership Program of the CAS, Grant/Award Number: 132744KYSB20190039

Abstract

The Beishan complex is composed of orthogneiss and metagreywacke that both enclose bodies of eclogite and serves as a unique example for comparative petrological study of all these lithologies. The rocks show the earliest regional steep N-S striking fabric (S2) preserved in low strain domains that are reworked by ubiquitous steep N-NE dipping cleavage (S3). The eclogite shows an almost isotropic fabric defined by an M1 assemblage of Grt–Cpx–Amp–Qz–Rt–Ilm that is locally retrogressed to M2-3 amphibolite facies mineral assemblages, with *P–T* peak at 20–21 kbar and 750–775°C and retrogression to 2–3 kbar and 530–550°C. The typical mineral assemblage of the host metagreywackes is Bt–Ms–Pl–Qz−Chl–Ilm±Grt. Rare Al-rich metagreywacke layers are composed of Grt–Ky–St±Sil−And–Bt–Ms–Pl–Qz±Chl±Rt–Ilm giving a *P–T* path with peak at 8–8.5 kbar and ~670°C correlated with the S2 fabric and retrogression to ~2.5 kbar and 525–550°C correlated with the S3 foliation. In two eclogite samples, the garnet-whole rock-clinopyroxene Lu–Hf isochrons give ages of 461.9±1.6 Ma and 462.0±6.2 Ma interpreted as reflecting average age of garnet formation, and Sm–Nd isochrons give ages of 453.6±2.7 Ma and 452.8±3.0 Ma interpreted as dating near-peak metamorphism. In metagreywacke, in-situ U–Pb dating of monazite gives two groups of ages of 445–440 Ma (Mnz cores) and 436–429 Ma (Mnz rims), interpreted as reflecting the metamorphic peak and retrogression. Our results show that eclogite was formed during Ordovician by subduction of a continental crust (D1). Eclogite and metagreywacke underwent partly decoupled *P–T–t–D* paths until their juxtaposition at mid-crustal levels during a first late Ordovician–early Silurian D2 shortening. Coupling of their *P–T–t–D* paths occurred during exhumation in the Silurian and a second and orthogonal D3 shortening event. The data from the Beishan Orogen are consistent with a collisional intra-Gondwanan orogen located south of the Central Asian Orogenic Belt.

KEYWORDS

Beishan Orogen, CAOB, eclogite, in-situ monazite U–Pb dating, *P–T–t–D* paths

1 | INTRODUCTION

Eclogites are important indicators of oceanic and continental subduction processes along convergent margins throughout Earth's tectonic history (Brown, 2007; Ernst, 2001). In the modern plate tectonics paradigm, eclogites mainly develop along the following two main subduction-orogenic systems: (a) Alpine-type subduction-collisional orogenic belts formed by subduction of oceanic and continental crust during closure of short-lived 'interior' oceanic basins surrounded by continental blocks. These systems are characterized by imbrication of passive margin sediments mainly involving carbonates and silico-clastics and oceanic slivers (Ernst, 2005). (b) Pacific-type belts that originate due to long-lasting subduction of giant peripheral oceans leading to accretion of oceanic sediments, cherts and basalts, and disaggregated ophiolites. The Pacific peripheral system is more often represented by Franciscan type mélange of blueschists and eclogites with sedimentary or serpentinite matrix (Cawood et al., 2009). By contrast, the subduction-collisional systems are associated with the burial of continental crustal rocks to ultrahigh-pressure (UHP) conditions and their exhumation in the form of coherent units as described in the Norwegian Caledonides (Andersen, Jamtveit, Dewey, & Swensson, 1991), the Western Alps (Chopin, Henry, & Michard, 1991), the Dabie-Sulu Terrane (Hacker et al., 1997) or in the Himalaya (Lombardo & Rolfo, 2000). However, in certain (U)HP terranes like the Sivrihisar Massif in Turkey (Whitney, Teyssier, Toraman, Seaton, & Fayon, 2011) or the Bohemian massif (Štípská et al., 2012; Štípská, Schulmann, & Powell, 2008), the oceanic crust derived eclogites are mixed with continental host rocks that preserve lower pressures pointing to a complex subduction–collisional history (e.g. Schulmann, Lexa, Janousek, Lardeaux, & Edel, 2014).

Therefore, a problem arises as to whether eclogites and their surrounding rocks are characterized by shared, partly shared or entirely decoupled *P–T* histories (Štípská, Pitra, & Powell, 2006). Often, HP to UHP assemblages are preserved only in mafic rocks that provide straightforward insights to their *P–T* metamorphic history but rarely in their felsic counterparts. This is because felsic gneiss might react less during prograde metamorphism due to the lack of H_2O or might undergo stronger overprinting during retrogression inducing loss of their HP mineral assemblage (Guiraud, Powell, & Rebay, 2001; Heinrich, 1982; Proyer, 2003). Many studies argue for non-equilibration (Palin, Reuber, White, Kaus, & Weller, 2017; Young & Kylander-Clark, 2015) and explain it by kinetic arguments (Koons, Rubie, & Fruch-Green, 1987), or by lack of fluid or deformation (Rubie, 1986). In these rocks the only evidence of eventual (U)HP stage is represented by mineral inclusions in garnet or preserved garnet composition (e.g. Chopin et al., 1991; Štípská et al., 2019).

The Central Asian Orogenic Belt (CAOB) represents one of the Earth's largest accretionary orogens characterized by numerous HP to UHP rocks with ages ranging from Late Proterozoic (e.g. Khain et al., 2003 and references therein; Ozorbaev et al., 2010), early Palaeozoic (e.g. Štípská, Schulmann, Lehmann,Lexa, & Tomurhuu, 2010; Volkova & Sklyarov, 2007) and Late Palaeozoic (e.g. Gao & Klemd, 2003). The northernmost Late Proterozoic–early Palaeozoic subduction system in Kazakhstan, Western Sayans and Mongolia is commonly represented by blueschists and eclogites associated with ophiolite slivers typical for Pacific-type subduction of a giant Palaeo-Asian Ocean (e.g. Dobretsov & Buslov, 2007; Safonova & Santosh, 2014 and references therein). By contrast, the southern Kyrgyz and Chinese Tianshan Carboniferous UHP rocks are represented by volcano-sedimentary units which resemble incomplete Alpine-type sequences pointing to final collisional stage (Gao, Ki, Xiao, Tang, & He, 1998; Gao & Klemd, 2003). The Beishan Orogen at the southernmost boundary of the CAOB represents a specific domain where the Ordovician *c*. 467 Ma Gubaoquan eclogite lenses enclosed in granitic gneiss have been described (Liu, Chen, Jahn, Wu, & Liu, 2010; Qu et al., 2011; Mei et al., 1998; Yang, Wu, Chen, Shi, & Zhang, 2006). The age of eclogite facies metamorphism led Qu et al. (2011) to propose a model of initiation of northward subduction of the Palaeo-Asian Ocean north of the Tarim-North China cratonic blocks. Whether the Gubaoquan eclogite has an oceanic or a continental origin has significant implications for the Early Palaeozoic tectonic evolution of the Beishan Orogen and the CAOB and therefore it requires detailed investigations. Here, elucidation of the petrogenesis of eclogites (Liu, Chen, et al., 2010; Liu, Gao, et al., 2010; Mao, Xiao, Windley, et al., 2012; Qu et al., 2011; Saktura et al., 2017) and thermo-chronological relations to the host gneisses may further constrain the geodynamic character of the southern margin of the CAOB.

In this paper we provide a comparative study of *P–T–t–D* histories of the Gubaoquan eclogite and its host gneisses. We carried out a petro-structural study to constrain the spatial relations between both rock types and define the structures related to different deformation events recorded in the area. Metamorphic studies were further combined with *P–T* pseudosection calculations, garnet Lu–Hf and Sm–Nd and in-situ monazite U–Pb dating in order to constrain the timing of these different events. Finally, the results of this comparative study are used to propose a new tectonic model of the southern Beishan Orogen with regard to the nature of the Palaeo-Asian ocean and its affinity to subduction/collisional or subduction accretionary oceanic systems.

2 | GEOLOGICAL SETTING

The Beishan Orogen is located in the southern part of the CAOB, connecting the South Tianshan suture in the west to the Solonker suture in the east. It is bounded by the South Mongolia accretionary system to the north and the Dunhuang block to the south. The Beishan Orogen is formed by polyphased accretion and amalgamation of different microcontinents, magmatic arcs and ophiolitic belts (Liu & Wang, 1995; Xiao, Mao, et al., 2010; Zuo, Liu, & Liu, 2003; Zuo, Zhang, He, & Zhang, 1991; Zuo et al., 1990). The orogen is commonly subdivided from north to south as follows: the Querrshan arc, the Heiyingshan-Hanshan arc, the Mazhongshan arc-accretionary terrane and the Huanishuan-Shuangyingshan arc (Figure 1a).

The Huanishuan-Shuangyingshan arc is bounded by the Hongliuhe-Xichangjing ophiolitic mélange to the north and the Liuyuan mélange to the south (Figure 1b). The Liuyuan mélange is considered either as an ophiolitic fore-arc sliver (Mao, Xiao, Windley, et al., 2012; Xiao, Mao, et al., 2010) or a Carboniferous-Permian rift (Jiang et al., 2007; Zhao, Guo, Han, Wang, & Liu, 2006; Zuo, Liu, & Liu, 2003; Zuo et al., 1990). Medium- to high-grade metamorphic rocks occurring throughout the Beishan Orogen from the Hongshishan area in the north to the Liuyuan area in the south are referred to as the 'Beishan complex' (BGMRG, 1993; Mei, Yu, & Li, 1997; Mei et al., 1998; Song, Xiao, Windley, Han, & Yang, 2016; Xiao, Mao, et al., 2010; Zheng, Li, Xiao, & Zhang, 2018; Zuo, Zhang, He, & Zhang, 1991; Zuo et al., 1990). In the area around city Liuyuan (Figure 1b), the Beishan complex is composed of up to amphibolite facies granitic gneiss, migmatite, amphibolite and micaschist (Song et al., 2016; Zong et al., 2017). In the studied Gubaoquan area (Figure 2), the Neoproterozoic (*c*. 900 Ma) augen gneiss host several bodies of Ordovician eclogite and retrograde amphibolite (Liu, Chen, et al., 2010; Liu, Gao, et al., 2010; Mei et al., 1998; Qu et al., 2012; Yang et al., 2006). The gneiss-eclogite complex is intruded by a granodiorite body at 438 ± 5 Ma (Liu, Chen, et al., 2010; Liu, Gao, et al., 2010), granitic veins at 424 ± 8.6 Ma (Saktura et al., 2017) and by Permian doleritic dykes (Zhang et al., 2015).

The eclogite chondrite-normalized REE and HFSE patterns are typical of E- and N-MORB protoliths, characteristic of seamounts and oceanic crust (Qu et al., 2011). Mei et al. (1998) constrained peak and retrograde metamorphic conditions at 16–18 kbar and 700–800°C and 10–12 kbar and 650°C respectively, based on Grt–Cpx and Grt–Hbl geothermobarometers. Qu et al. (2011) used thermodynamic modelling to define a clockwise *P*–*T* path from >15.5 kbar and 700–800°C to 12–14 kbar and 700–750°C. The protolith age of the eclogites was constrained by zircon U–Pb method at 1,007 ± 20 Ma and 819 ± 21 Ma (Yang et al., 2006), 881 ± 12 Ma (Qu et al., 2011) and 886 ± 4 Ma (Liu, Chen, et al., 2010). The age of metamorphism was constrained by zircon U-Pb dating at 465 ± 10 Ma (Liu, Chen, et al., 2010; Liu, Gao, et al., 2010), 467 ± 16 Ma (Qu et al., 2011) and 466 ± 27 Ma (Saktura et al., 2017). ^{39}Ar–^{40}Ar biotite age of 428.9 ± 3.8 Ma in an augen gneiss is interpreted to date the gneiss and eclogite exhumation (Qu et al., 2011). Based on Mesoproterozoic and Neoproterozoic zircon ages and zircon $\mathcal{E}_{Hf}(t)$ values (−8.0 to 10.1), He, Klemd, Yan, and Zhang (2018) proposed that the eclogite host gneiss formed the 'Liuyuan continental terrane' during the Precambrian.

3 | STRUCTURAL ANALYSIS

In the studied area, a large eclogite boudin (~300m long and 100m wide) is enclosed within metagreywacke and paragneiss and smaller eclogite and amphibolite lenses occur within metagreywacke, paragneiss and felsic orthogneiss (Figures 2 and 3a,b). The eclogite has massive and isotropic texture and macroscopically does not exhibit any fabrics, therefore the eclogite facies assemblage is referred as M1 here. The structural relations between the metabasites and their gneissic host rocks have been investigated and two macroscopic fabrics have been identified. The steeply to moderately inclined N-S trending S2-M2 mineral fabric is mainly preserved in the metagreywacke and paragneiss as a metamorphic schistosity defined by two micas- and chlorite-rich layers within a quartz matrix (Figure 2). The S2 foliation is reworked by metric to centimetric open to isoclinal symmetric (Figure 3d–f) to asymmetric (Figure 3g) F3 folds with fold axes plunging moderately to steeply to N or NE and axial-planes dipping to the N or NE at moderate to steep angles (Figures 2 and 3d–g). Oriented biotite and white mica define the moderately NE or E plunging intersection L3 lineation parallel to the fold or crenulation axes (Figure 2b). The F3 folding is associated with the formation of axial-planar cleavage that leads to almost complete transposition into the S3-M3 mineral fabric in the majority of gneisses and metagreywackes (Figure 3c). The S3 fabric dips moderately to steeply to the N-NE and is defined by alternations in quartz-rich and two-mica-, chlorite- and andalusite-rich domains in metagreywacke and alternation in quartz and biotite bands in orthogneiss (Figure 2a,b). Leucogranitic veins intrude the D2 structures in the gneisses as well as the main eclogite body (see figure 3a in Liu, Chen, et al., 2010; Liu, Gao, et al., 2010). All fabrics and leucogranitic veins are crosscut and intruded by plurimetric subvertical E–W and ENE–WSE striking doleritic dikes that are undeformed (Figure 2 and see figure 2 in Zhang et al., 2015).

4 | METHODOLOGY AND ANALYTICAL METHODS

The rocks enclosing the metabasites are dominated by orthogneiss, the Al-rich metagreywacke and paragneiss are

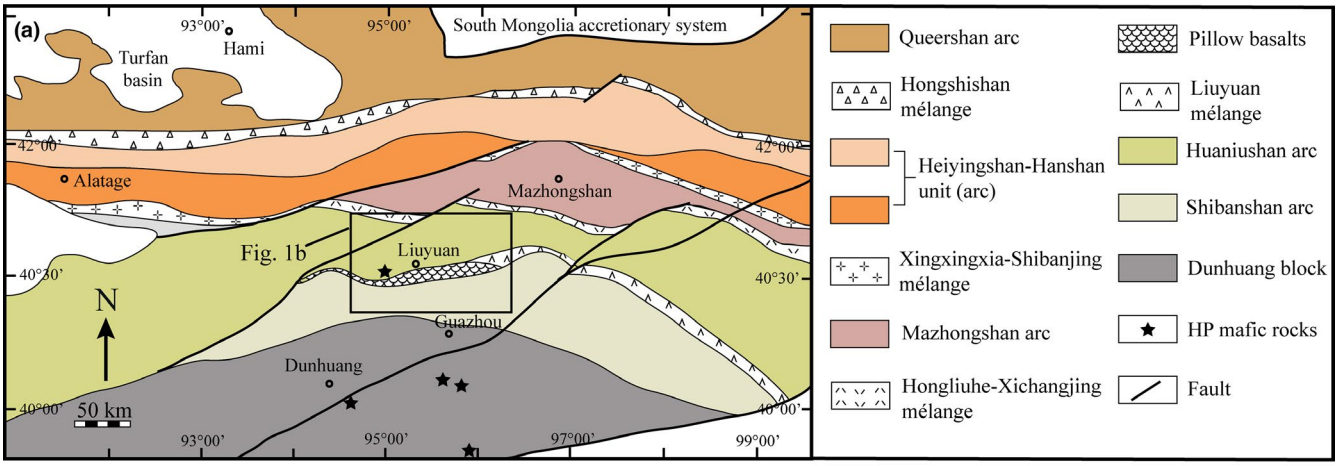

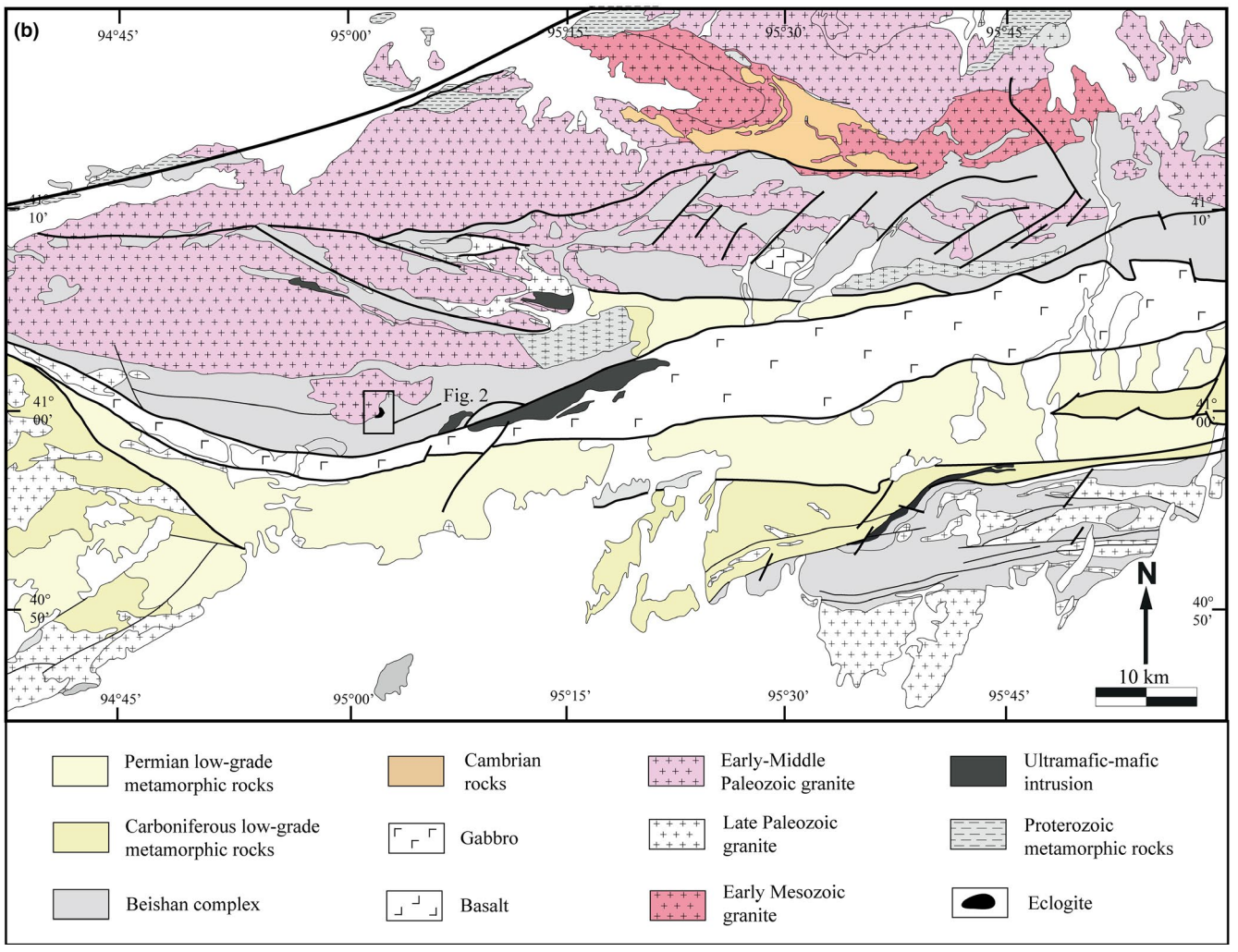

FIGURE 1 (a) Tectonic map of the Beishan orogen showing the position of the different arcs modified after Liu and Wang (1995), Nie et al. (2002) and Mao, Xiao, Windley, et al. (2012). (b) Simplified geological map of the Shuangyingshan (or Huaniushan arc) area with the main stratigraphic units and intrusive rocks (modified after GSBGMR, 1989; Mao, Xiao, Windley, et al., 2012; Nie et al., 2002; Zuo et al., 1990)

subordinate (Figure 2b). As the metagreywacke samples contain assemblages sensitive to *P–T* evolution, they were chosen as representative of the evolution of the gneiss complex. We show petrography of representative samples of eclogite (16JS79-4, XIGB04), amphibolite (16JS79-2) and metagreywacke (13GB01, 13GB10, 16JS87). The eclogite samples used for mineral equilibria modelling (16JS79-4) and garnet Lu–Hf and Sm–Nd dating (16JS79-4 and XIGB02) were collected at the same location in the main eclogite body (40°59′15.5″N, 95°02′19.4″E). Amphibolite (16JS79-2) and metagreywacke

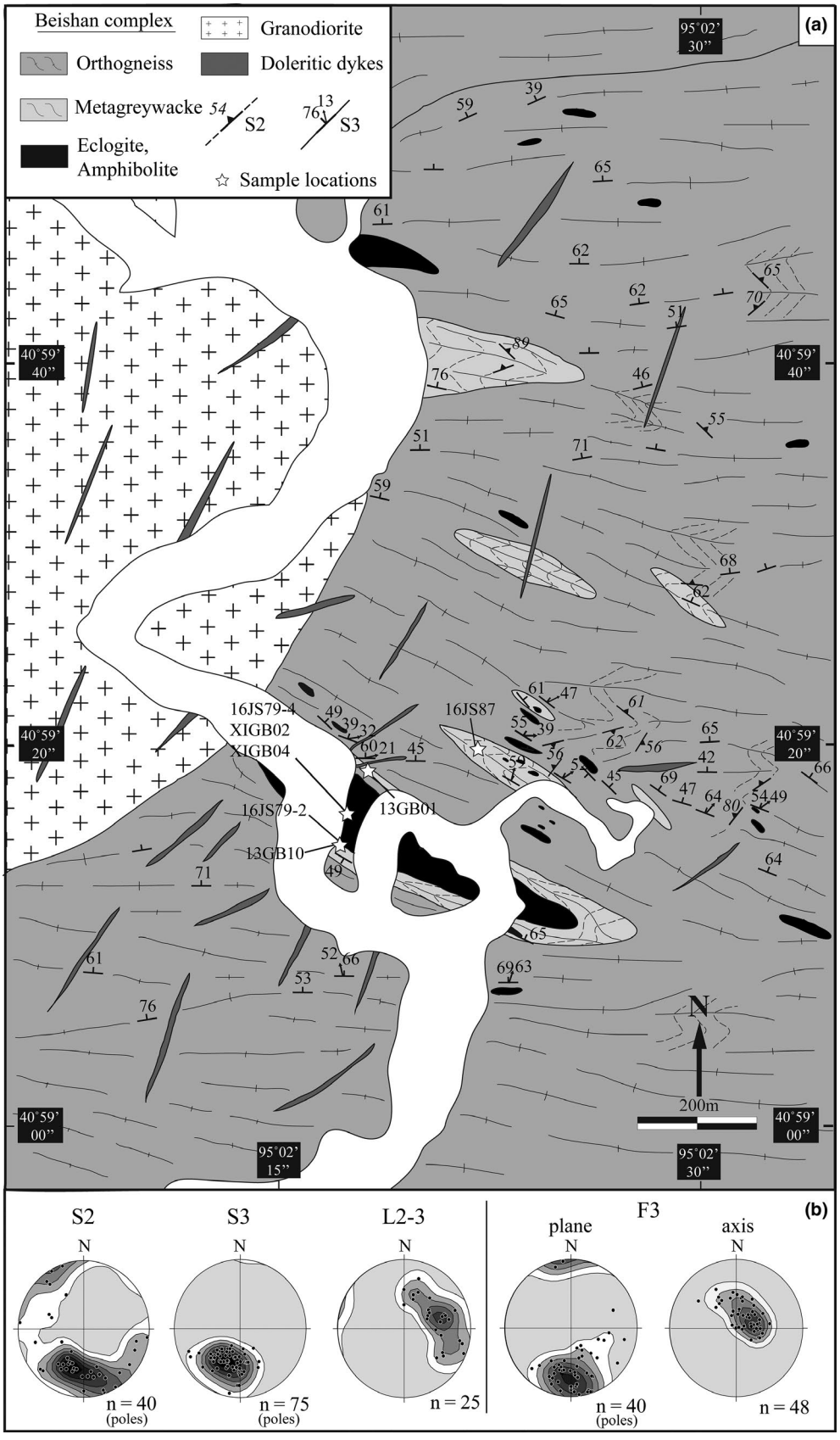

FIGURE 2 (a) Geological map of the Gubaoquan area located in the southern Beishan. Locations of the samples for petro-structural and geochronological analysis are indicated. (b) Equal area, lower hemisphere stereonets showing planar and linear structures in the area

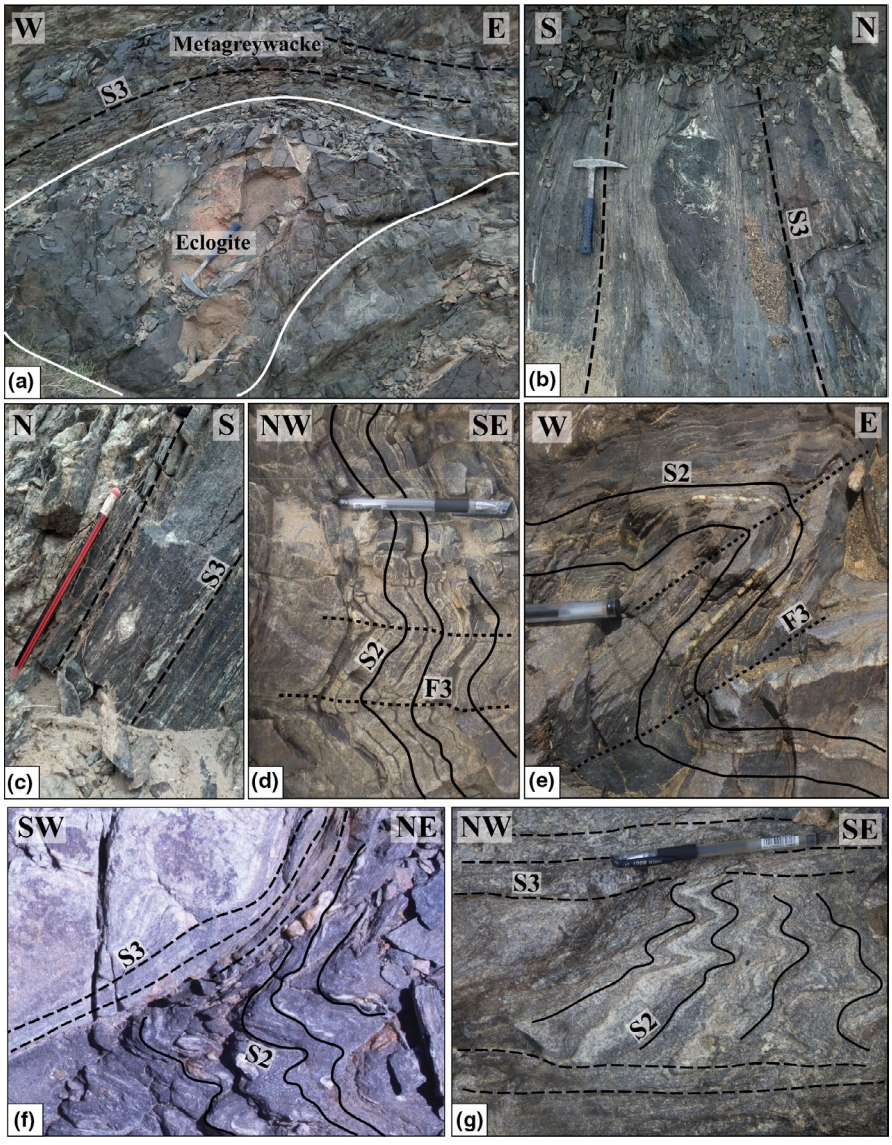

FIGURE 3 Field photographs of the tectono-structural features. (a, b) Eclogite boudins occurring in S3 in metagreywacke. (c) Subvertical S3 fabric in orthogneiss. (d–g) Structural succession of the S2 and S3 fabrics. S2 fabric is reworked by symmetric to rarely asymmetric F3 folds which have fold axes plunging moderately to steeply to N or NE and axial planes dipping to N or NE under moderate to steep angles

(13GB10) samples used for mineral equilibria modelling and in-situ monazite U–Pb dating were sampled at the southern edge of the eclogite body (40°59′14.2″N, 95°02′19.00″E). The metagreywackes 13GB01 (40°59′20.0″N, 95°02′19.4″E) and 16JS87 (40°59′21.8″N, 95°02′33.75″E) used for in-situ monazite U–Pb dating were sampled to the north of the main eclogite body.

Whole-rock major element geochemistry for homogeneous eclogite and amphibolite samples and the least retrogressed metagreywacke samples used for pseudosection calculations was determined at the State Key Laboratory of Isotope Geochemistry (SKLaBIG) at Guangzhou Institute of Geochemistry Chinese Academy of Sciences (GIGCAS) using XRF spectrometry. Major element compositions of minerals and monazite mapping for Y, La, Th and U were performed using a JEOL JXA-8100 electron microprobe (EPMA) at Key Laboratory of Mineralogy and Met allogeny (KLaBMM) at GIGCAS.

Lu–Hf and Sm–Nd garnet dating were conducted in the Kraków Research Center, Institute of Geological Sciences, Polish Academy of Sciences. Sample digestions, columns chemistry and mass spectrometry procedures are given in Thirlwall and Anczkiewicz (2004) and Anczkiewicz, Platt, Thirlwall and Wakabayashi (2004) and references therein. Reproducibility of the analyses estimated by repetitive measurements of JMC475 Hf standard yielded $^{176}Hf/^{177}Hf = 0.282162 \pm 5$ ($n = 5$) over the course of analyses. The measured Hf isotope ratios were normalized to $^{179}Hf/^{177}Hf = 0.7325$. Similarly, JNd-1 measured over the course of analyses yielded $^{143}Nd/^{144}Nd = 0.512102 \pm 6$ ($n = 6$) and the ratios were normalized to $^{146}Nd/^{144}Nd = 0.7219$. Age calculations were conducted using decay constants $\lambda_{176Lu} = 1.865 \times 10^{-11}$ (Scherer, Munker, & Mezger, 2001) and $\lambda_{147Sm} = 6.02 \times 10^{-12}$ year^{-1} (Lugmair & Marti, 1978). In order to facilitate interpretation of the isotope systematics we additionally conducted LA–ICP–MS analyses of major

and trace element distribution in garnet in sample XIGB02. The analyses were conducted in the Kraków Research Center, Institute of Geological Sciences, Polish Academy of Sciences, using and excimer (ArF) laser RESOlution M50 by Resonetics (now Australian Scientific Instruments) coupled with ICPMS XSeriesII by Thermo Scientific.

The trace element compositions of rutile and garnet (in eclogite sample 16JS79-4 and metagreywacke samples) were measured in-situ by LA-ICP-MS (Resonetics RESOlution S-155 laser+Agilent 7900) in the KLabMM at GIGCAS. Helium gas carrying the ablated sample aerosol is mixed with argon carrier gas and nitrogen as additional diatomic gas to enhance sensitivity. Prior to analysis, the LA-ICP-MS system was optimized using NIST610 ablated with 29 μm spot size and 5 μm/s scan speed to achieve maximum signal intensity and low oxide rates. Each analysis included ~20 to 30 s of background acquisition (from a gas blank) followed by 50 s of data acquisition from the sample with a spot size of 43 μm. The multiple reference materials (BCR-2G, BHVO-2G and BIR-1G) were used as external calibration reference and Si was used as the internal standard to quantify elemental concentrations in samples. The offline selection and integration of the background and analytical signals, time-drift correction and quantitative calibration were performed using ICPMSDataCal (Lin, Liu, Yang, & Hu, 2016; Liu, Chen, et al., 2010; Liu, Gao, et al., 2010; Liu et al., 2008).

In-situ monazite U–Pb and trace elements analysis were acquired at the State Key Laboratory of Geological Processes and Mineral Resources, China University of Geosciences, Wuhan. Sample ablation was performed in thin section using an ArF excimer GeoLas 2005 193 μm connected to an Agilent 7500a ICP-MS instrument. Helium was used as carrier gas. Detailed operating conditions and analytical procedure followed methods described by Liu et al. (2008).

All concordia diagrams, weighted mean and isochron calculations were performed using Isoplot 3.75 (Ludwig, 2003). All ages are quoted with 2σ uncertainty. Details for all analytical procedures may be found in Appendix S1.

5 | PETROGRAPHY, MINERAL COMPOSITIONS AND MICROSTRUCTURES

The petrography of metabasic rocks and metagreywackes is shown in Figures 4 and 5, and crystallization–deformation relations are summarized in Figure 6. The mineral composition of garnet is shown in Figure 7, and of pyroxene, amphibole and plagioclase in Figure 8. Representative mineral analyses are given in Tables 1 and 2.

Mineral abbreviations are after Whitney and Evans (2010). Alm = $Fe^{2+}/(Fe^{2+}+Mg+Ca+Mn)$, Prp = $Mg/(Fe^{2+}+Mg+Ca+Mn)$, Grs=$Ca/(Fe^{2+}+Mg+Ca+Mn)$, Sps=$Mn/(Fe^{2+}+Mg+Ca+Mn)$, Jd = Na/(Na+Ca), An=Ca/(Ca+Na+K), Ab=Na/(Ca+Na+K), Or=K/(Ca+Na+K), *X*Fe=$Fe^{2+}/(Fe^{2+}+Mg)$, *X*Mn=$Mn/(Fe^{2+}+Mg+Mn)$, En=$Mg/(Mg+Fe^{2+})$.

5.1 | Petrography and mineral chemistry of eclogite samples

The eclogite is a massive coarse- to medium-grained rock without obvious preferred orientation of minerals (Figure 4a). Samples 16JS79-4 and XIGB04 have the mineral assemblage of Grt–Cpx–Pl–Amp–Qz–Rt–Ilm with some clinopyroxene–plagioclase and amphibole–plagioclase symplectites. The proportions of minerals are approximately: garnet (~40 vol.%), omphacite (25–30 vol.%), green amphibole (~5 vol.%) and quartz (<5 vol.%), clinopyroxene-plagioclase and amphibole-plagioclase symplectites (~20 vol.%) and accessory rutile and ilmenite. Garnet (100–500 μm in size, Figure 4a–d) contains inclusions of omphacite, amphibole, quartz, plagioclase, rutile and ilmenite (Figure 4d), garnet in sample XIGB04 also includes orthopyroxene. Matrix omphacite (0.2–1 mm) has clinopyroxene-plagioclase symplectite (symp I) locally developed along mineral cleavage or at grain boundaries (Figure 4c). Amphibole–plagioclase symplectites (symp II) occur mainly along the boundaries of omphacite and around clinopyroxene-plagioclase symplectite (Figure 4c). Garnet is commonly surrounded by amphibole–plagioclase kelyphite (kely I) or amphibole (Figure 4b,c). Amphibole is fine-grained in the symplectite and up to 200–600 μm in the matrix (Figure 4b). Ilmenite occurs around rutile in the matrix and within the kelyphite around garnet (Figure 4d).

Garnet is compositionally zoned. In sample 16JS79-4, from core ($Alm_{0.54–0.58}$ $Grs_{0.18–0.24}$ $Prp_{0.21–0.23}$ $Sps_{0.01}$*X*$Fe_{0.71–0.72}$) to mantle grossular increases and pyrope and almandine decrease ($Alm_{0.52-0.57}$ $Grs_{0.22–0.27}$ $Prp_{0.20–0.21}$ $Sps_{0.01}$*X*$Fe_{0.72–0.74}$), and from mantle to rim grossular decreases and almandine increases ($Alm_{0.54–0.57}$ $Grs_{0.21–0.25}$ $Prp_{0.19–0.21}$ $Sps_{0.01}$*X*$Fe_{0.73–0.75}$; Figure 7a,e). In sample XIGB04, garnet is also compositionally zoned. Form core ($Alm_{0.52–0.54}$ $Grs_{0.23–0.26}$ $Prp_{0.21–0.22}$ $Sps_{0.01}$*X*$Fe_{0.71}$) to mantle grossular increases and pyrope and almandine decrease ($Alm_{0.50–0.54}$ $Grs_{0.23–0.29}$ $Prp_{0.20–0.22}$ $Sps_{0.01}$*X*$Fe_{0.70–0.72}$), and from mantle to rim grossular decreases and pyrope and almandine increase ($Alm_{0.52–0.56}$ $Grs_{0.20–0.24}$ $Prp_{0.21–0.23}$ $Sps_{0.01}$*X*$Fe_{0.70–0.73}$; Figure 7b,f). In both samples, matrix pyroxene is unzoned omphacite (Jd = 0.24–0.31, Ca = 0.65–0.72 p.f.u., *X*Fe = 0.28–0.32), clinopyroxene included in garnet is omphacite (Jd = 0.27–0.30, Ca = 0.65–0.68 p.f.u., *X*Fe = 0.26–0.32), clinopyroxene in symplectite I is diopside (Jd = 0.06–0.09, Ca = 0.87–0.92 p.f.u., *X*Fe = 0.22–0.30; Figure 8a). Orthopyroxene included in garnet in XIGB04 is enstatite (En = 0.45–0.50,

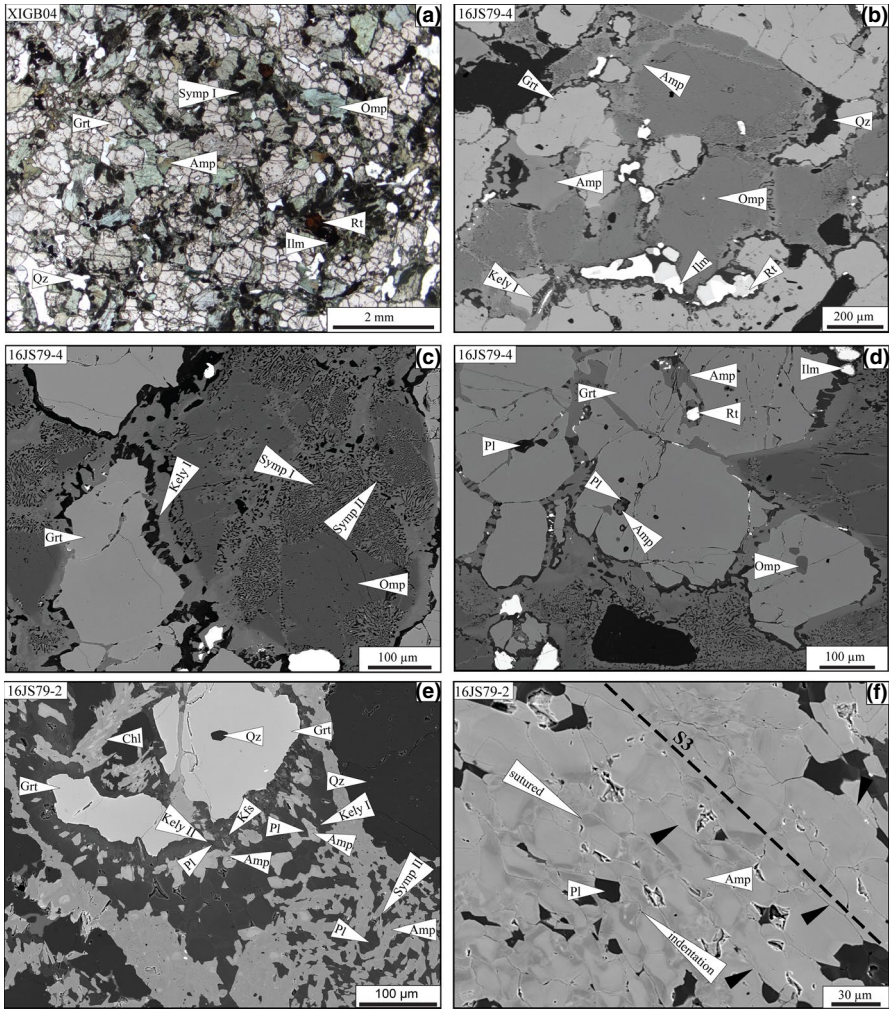

FIGURE 4 Thin section microphotographs and backscattered electron (BSE) images of the Gubaoquan metabasites. (a) Isotropic texture in eclogite XIGB04. (b) Matrix Grt–Cpx–Amp–Pl–Ilm–Qz assemblage in eclogite 16JS79-4. (d) Multiple mineral inclusions in garnet in 16JS79-4. (e) Symplectite I (clinopyroxene+plagioclase) and symplectite II (amphibole+plagioclase) in the matrix, and kelyphite (amphibole+plagioclase) around garnet in 16JS79-4. (e) Kelyphite (amphibole+plagioclase+K-feldspar) around garnet and symplectite II in the matrix in 16JS79-2. (f) Recrystallized fine-grained amphibole defining S3 in amphibolite 16JS79-2. Sutured and indented grain boundaries occur between amphibole grains parallel to S3

*X*Fe = 0.50–0.55; Figure 8b). Amphibole in the matrix, symplectite II and kelyphite is mainly edenite, pargasite and hornblende sensu *lato* (Si = 5.90–7.01 p.f.u., Ca = 1.75–1.84 p.f.u., Al^{IV} = 0.92–2.09 p.f.u.), amphibole included in garnet is edenite, pargasite and hornblende sensu *lato* (Si = 5.84–7.37 p.f.u., Ca = 0.50–2.00 p.f.u., Al^{IV} = 0.66–2.06 p.f.u.; Figure 8c,d). Plagioclase in symplectite I and II has a lower albite component (Ab = 0.68–0.83) compared to plagioclase in kelyphite (Ab = 0.91; Figure 8e). Plagioclase included in garnet has a similar composition range (Ab = 0.64–0.95; Figure 8e; Table 1).

5.2 | Petrography and mineral chemistry of amphibolite

Amphibolite 16JS79-2 represents the retrogressed amphibolitic rim of the main eclogite body and is characterized by the mineral assemblage Grt–Amp–Pl–Chl–Qz–Kfs–Rt–Ilm (Figure 4e,f). The sample is composed of garnet (~15 vol.%), amphibole–plagioclase symplectite (symp II, identical to symp II in eclogite, 50–60 vol.%), amphibole–plagioclase kelyphite (kely I) and amphibole–plagioclase-alkali feldspar kelyphite (kely II; <5 vol.%), quartz (5–10 vol.%) and matrix amphibole (10–15 vol.%). Garnet includes plagioclase, amphibole, quartz, rutile and ilmenite, and has fractures filled with chlorite (Figure 4e). Amphibole occurs either as recrystallized grains in the matrix orintergrowth with plagioclase (symp II) containing locally also ilmenite. Coarse-grained matrix amphibole (150–600 µm) is dynamically recrystallized into fine-grained amphibole (25–100 µm) with strong shape preferred orientation (Figure 4f). Recrystallized grains display core–rim structures with sutured and indented grain boundaries, parallel to the S3 fabric (Figure 4f).

Garnet is compositionally zoned with pyrope and almandine increasing and grossular decreasing from core ($Alm_{0.501–0.49}$ $Grs_{0.27–0.22}$ $Prp_{0.25–0.22}$ $Sps_{0.01}XFe_{0.69–0.67}$) to rim ($Alm_{0.54-0.51}$ $Grs_{0.24–0.18}$ $Prp_{0.27–0.24}$ $Sps_{0.01}XFe_{0.68–0.67}$; Figure 7c,g). Amphibole included in garnet is pargasite and hornblende sensu *lato* (p.f.u.: Si = 6.47–8.14, Na = 0.39–0.59, Mg = 1.17–2.38, Al^{IV} = 1.08–1.73), amphibole in symplectite II is actinolite (p.f.u.: Si = 7.68–7.69, Na = 0.09–0.11, Mg = 2.93–3.24, Al^{IV} = 0.31–0.32). Amphibole in kelyphite II is actinolite (p.f.u.: Si = 7.71–7.81,

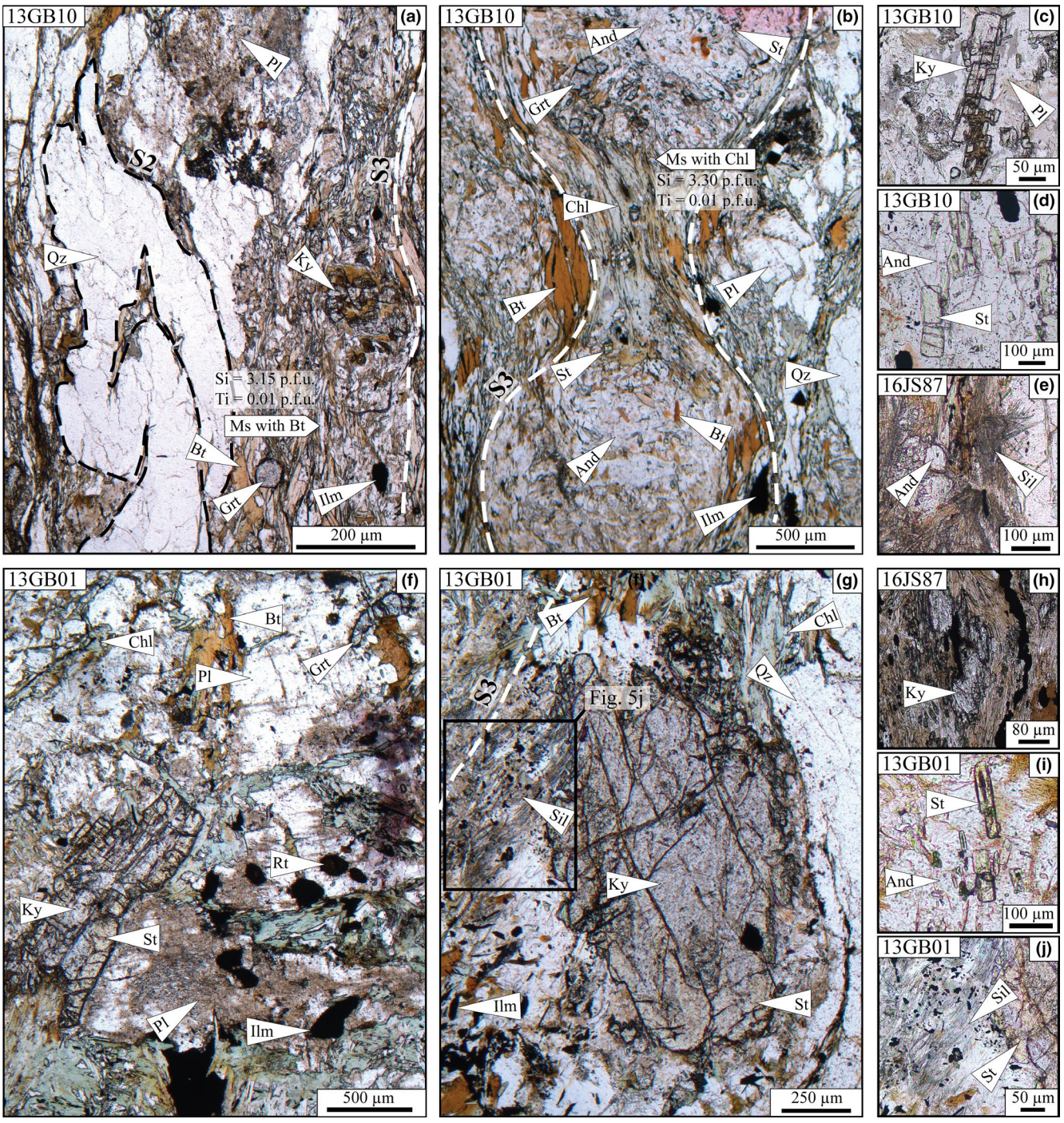

FIGURE 5 Thin section microphotographs and BSE images of representative metagreywacke samples. (a) S2 relict in the form of folded quartz ribbon in 13GB10. (b) Subvertical S3 fabric mainly formed by biotite, muscovite and andalusite in 13GB10. Chlorite and biotite in pressure shadows around andalusite. Andalusite porphyroblasts show multiple inclusions of garnet, staurolite and biotite. Close-up views of (c) kyanite in the matrix in 13GB10, (d) staurolite included in andalusite in 13GB10. (e) Close-up view of sillimanite and andalusite in the S3 fabric in 16JS87. (f) Kyanite inclusion in staurolite in the matrix in 13GB01. Garnet, biotite and rutile inclusions in plagioclase. (g) Kyanite inclusion in staurolite, surrounded by sillimanite in the S3 fabric in 13GB01. Close up views of (h) kyanite surrounded by the S3 fabric in the matrix in 16JS87, (i) staurolite inclusions in andalusite in 13GB01, (j) sillimanite in S3 around staurolite including kyanite in 13GB01

Na = 0.07–0.09, Mg = 3.04–3.06, Al^{IV} = 0.19–0.29). Amphibole in kelyphite I is mainly edenite and pargasite (p.f.u.: Si = 6.10–6.82, Na = 0.28–0.59, Mg = 1.56–2.16, Al^{IV} = 0.19–1.18; Figure 8c,d). Matrix recrystallized grains have edenite core (p.f.u.: Si = 6.44–6.78, Na = 0.49–0.54, Mg = 2.30–2.42, Al^{IV} = 1.22–1.56) and actinolite rim (p.f.u.: Si = 7.56–7.81, Na = 0.07–0.17, Mg = 3.01–3.27, Al^{IV} = 0.19–0.44). Plagioclase in symplectite II has higher

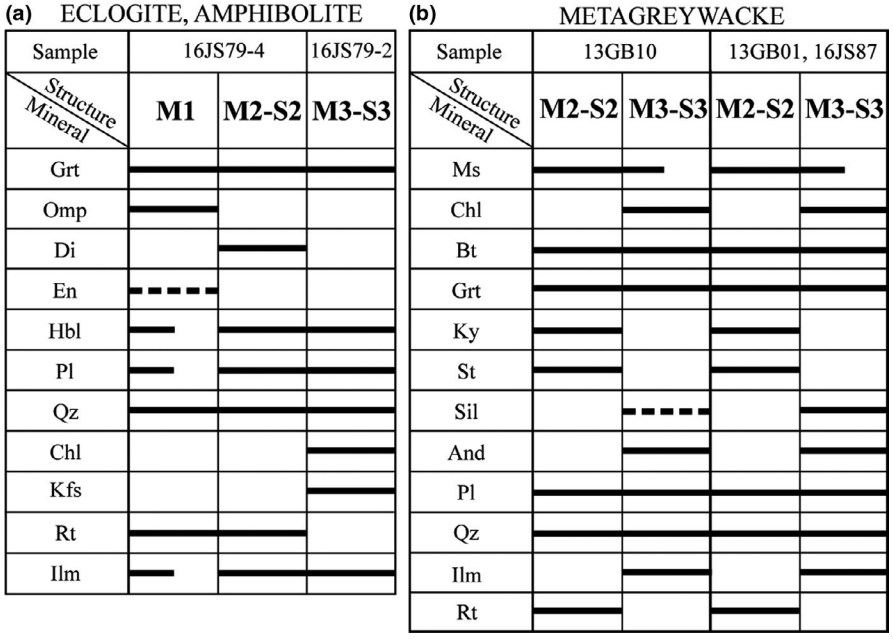

FIGURE 6 Crystallization–deformation relationships. (a) Eclogite sample 16JS79-4 and amphibolite sample 16JS79-2. (b) Metagreywacke samples 13GB10, 13GB01 and 16JS87. Dashed lines with question marks indicate uncertain stability. See text for details

albite content (Ab = 0.82–0.87) than plagioclase in kelyphite I (Ab = 0.72–0.77) and in kelyphite II (Ab = 0.42–0.47; Figure 8e; Table 1).

5.3 | Petrography and mineral chemistry of metagreywacke

The metagreywackes are characterized by monomineralic ribbons of recrystallized quartz alternating with biotite–muscovite-rich layers. Garnet, plagioclase, kyanite, staurolite, sillimanite and andalusite locally occur in the mica-rich layers. Most samples are retrogressed to a variable degree, in most samples chlorite, chlorite-muscovite aggregates and fine-grained muscovite occur.

Sample 13GB10 has the mineral assemblage Grt–Ky–St–And–Bt–Ms–Pl–Qz–Chl–Rt–Ilm and samples 13GB01 and 16JS87 additionally contain sillimanite. Because of the strong S3 overprint, the crystallization–deformation relations are not straightforward to decipher, and are described first for the S3 fabric. The S3 fabric is mainly defined by alternation in mica- and quartz-rich layers and by preferred orientation of biotite, muscovite and ilmenite (Figure 5a,b,g). Parallel to this fabric is also oriented sillimanite and as sillimanite was not observed folded, it is interpreted as part of the S3 fabric evolution (Figure 5e,g,j). Plagioclase porphyroblasts in places include kyanite, rutile and ilmenite. Andalusite porphyroblasts commonly enclose staurolite, biotite and ilmenite (Figure 5b,d,i) and also the S3 inclusion trails of biotite and ilmenite. The S3 pressure shadows around andalusite contain biotite and sillimanite. Biotite is locally chloritized, and biotite and chlorite occur in the S3 pressure shadows around andalusite and plagioclase porphyroblasts indicating that the S3 deformation continued after andalusite and plagioclase growth at decreasing temperature (Figure 5b,f). Therefore, the metamorphic succession involves early garnet, kyanite and rutile, followed by staurolite, and then within the S3 fabric the stability of the assemblage And–Bt–Ms–Pl–Ilm–Qz, then Sill–Bt–Ms–Pl–Ilm–Qz followed by the assemblage with Chl–Ms–Ilm.

The quartz layers show folded domains interpreted as relicts of the S2 fabric (Figure 5a). The garnet, kyanite, staurolite and rutile do not have oriented inclusion trails nor are clearly oriented which would help to associate them with either the S2 or S3 fabric. However, succession of crystallization among these minerals can be partly deciphered (Figure 6b). Garnet and plagioclase include in places rutile, and plagioclase porphyroblasts include also kyanite, which indicates that at least some parts of garnet and plagioclase grew in the rutile and kyanite stability fields (Figure 5c,f). Kyanite occurs surrounded by staurolite or by white mica in the matrix suggesting that kyanite is replaced by these minerals (Figure 5f–h). Replacement of kyanite by staurolite is epitaxial as confirmed by the EBSD (Figure S1), leaving in places only domains of kyanite in staurolite (see also Cesare & Grobety, 1995). It is thus likely that the kyanite–garnet–rutile–plagioclase-bearing assemblage can be associated with the S2 fabric. Staurolite replaces kyanite and is commonly included in andalusite suggesting that staurolite belongs to the late stages of the S2 fabric or to the early stages of the S3 fabric development.

In 13GB10, garnet is characterized by almandine and spessartine increase and pyrope and grossular decrease from core (henceforth Grt I, $Alm_{0.70–0.68}$ $Grs_{0.10–0.08}$

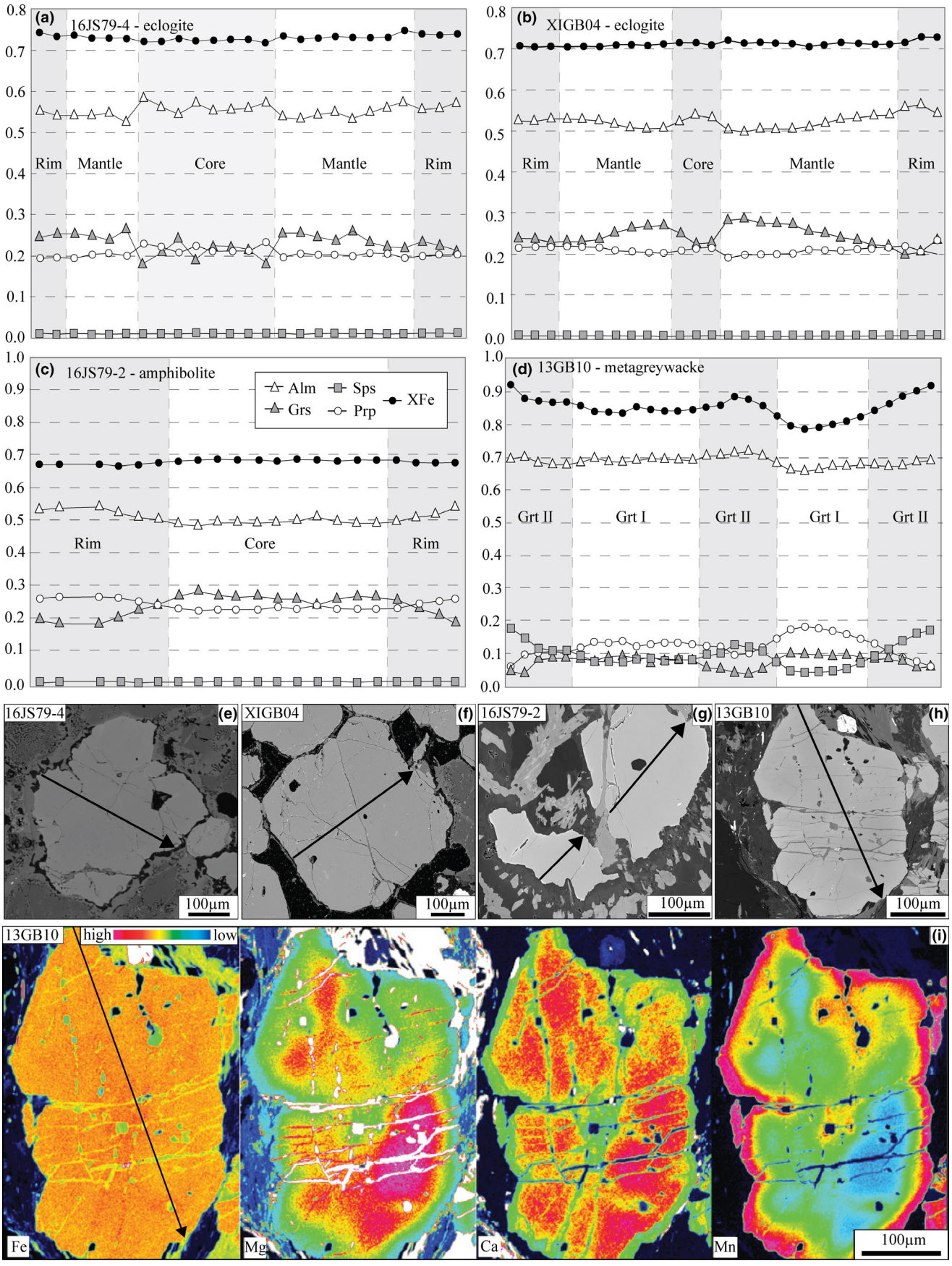

FIGURE 7 Compositional profiles of garnet in (a) eclogite 16JS79-4, (b) eclogite XIGB04, (c) amphibolite 16JS79-2, (d) metagreywacke 13GB10. BSE images of garnet in (e) eclogite 16JS79-4, (f) eclogite XIGB04, (g) amphibolite 16JS79-2, (h) metagreywacke 13GB10. (i) Compositional maps (Fe, Mg, Ca, Mn) of garnet in 13GB10, presented in (d) and (h)

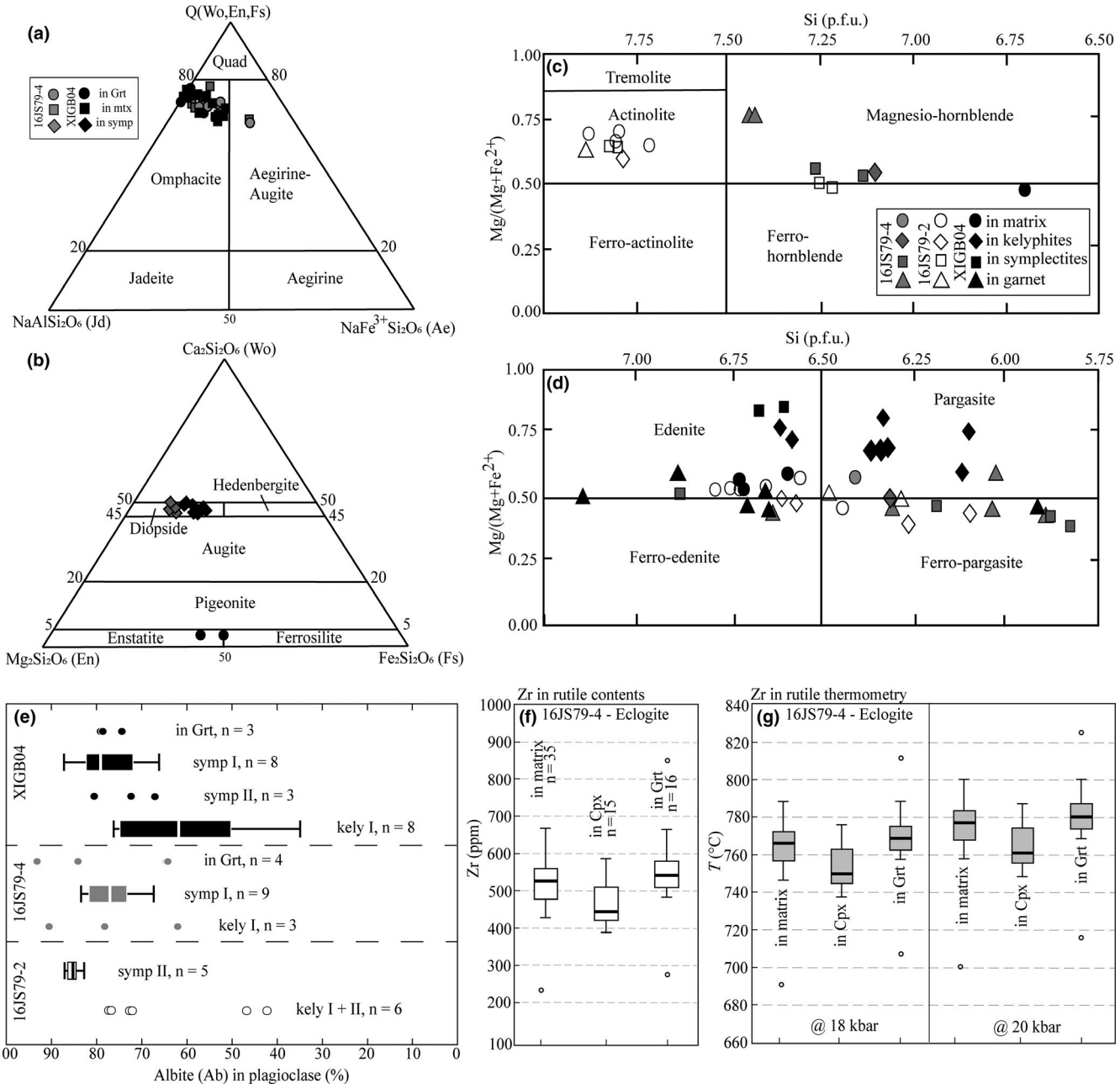

FIGURE 8 (a) Composition of clinopyroxene in Q(Wo-En-Fs)-Jd-Ae diagram after Morimoto (1988). (b) Composition ranges of the Ca-Mg-Fe clinopyroxene and orthopyroxene in the Wo-En-Fs diagram after Morimoto (1988). (c, d) Compositions and classification of amphibole in the diagram after Leake (1978). (e) Albite content (%) in plagioclase in different textural positions in metabasites. The results are given in the form of boxplots. (f) Zr content in rutile and (g) calculated temperature from the Zr in rutile thermometer after Tomkins et al. (2007) for eclogite 16JS79-4. For the box and whisker diagrams in (e–g), the line across the box represents the median value of the data and ranges are the interquartile ranges (differences between third and first quartile, Q3–Q1). Dots are analysis points beyond whiskers (outliers). The number of analysis is marked

$Prp_{0.19–0.12}$ $Sps_{0.10–0.05}XFe_{0.85–0.78}$) to rim (henceforth Grt II, $Alm_{0.72–0.67}$ $Grs_{0.10–0.05}$ $Prp_{0.15–0.06}$ $Sps_{0.18–0.07}XFe_{0.91–0.82}$; Figure 7d,h,i), and is affected by crack-like zones where the composition is comparable to the rim, and is therefore interpreted as being re-equilibrated during retrogression (Grt II). The garnet zonation characterized by high Mn rims is similar to compositional zoning resulting from retrograde diffusional re-equilibration (Tuccillo, Essene, & van der Plujim, 1990) and from preferential retention of Mn in garnet during its resorption (Grant & Weiblen, 1971). Staurolite compositional range is Fe^{2+} = 2.77–3.01 p.f.u., $XFe_{0.84–0.85}$ and $XMn_{0.03}$ (Table 2). Biotite in the S3 matrix, included in plagioclase and garnet, has XFe = 0.53–0.58 and Ti = 0.05–0.10 p.f.u. White mica associated with biotite (Ms–Bt) in the S3 matrix has Si = 3.09–3.18 p.f.u. whereas fine-grained sericite associated with chlorite

TABLE 1 Representative mineral analyses of eclogites 16JS79-4 and XIGB04 and amphibolite 16JS79-2

Mineral	Grt	Grt	Grt	Grt	Grt	Omp	Omp	Omp	Cpx	Opx	Amp	Amp	Amp	Amp	Amp	Amp	Amp	Amp	Amp	Pl	Pl	Pl	Pl
Sample	16JS79-4	16JS79-4	16JS79-4	XIGB04	XIGB04	16JS79-4	16JS79-4	XIGB04	16JS79-4	XIGB04	16JS79-4	19JS79-4	19JS79-4	19JS79-4	19JS79-2	19JS79-2	19JS79-2	19JS79-2	19JS79-2	19JS79-4	19JS79-4	16JS79-2	16JS79-2
Position	Core	Mantle	Rim	Mantle	Rim	Inc Grt	Mtx	Mtx	Symp	Inc Grt	Inc Grt	Mtx	Symp	Kely	Symp II	Kely I	Kely II	Mtx—core	Mtx—rim	Inc grt	Symp II	Kely I	Kely II
SiO_2	36.97	37.11	36.98	37.81	37.68	52.78	53.97	53.42	52.35	52.22	43.84	42.19	38.34	41.69	52.79	46.09	53.99	45.75	53.70	64.99	63.75	61.46	55.99
TiO_2	0.04	0.01	0.04	0.06	0.01	0.11	0.08	0.12	0.14	0.00	0.04	0.48	0.10	0.19	0.14	1.72	0.05	0.28	0.05	0.00	0.00	0.00	0.00
Al_2O_3	21.45	21.77	21.38	21.42	21.34	6.38	6.28	7.19	2.01	0.23	17.94	11.12	17.71	12.65	2.40	9.08	1.82	10.59	2.94	22.04	21.96	24.12	28.16
Cr_2O_3	0.02	0.02	0.00	0.00	0.00	0.09	0.00	0.07	0.04	0.00	0.00	0.00	0.00	0.00	0.00	0.00	0.00	0.00	0.00	0.00	0.00	0.00	0.00
FeO	27.12	26.20	27.48	26.36	27.51	9.66	6.94	8.39	9.12	32.53	17.11	19.18	20.97	19.54	15.35	18.96	15.47	17.71	13.52	0.91	0.47	0.20	0.14
MnO	0.48	0.42	0.54	0.50	0.54	0.04	0.05	0.04	0.03	0.35	0.11	0.09	0.11	0.09	0.19	0.14	0.17	0.10	0.10	0.03	0.00	0.00	0.01
MgO	5.30	5.12	5.06	5.63	5.18	9.80	9.32	9.72	12.46	15.09	6.98	11.73	6.67	9.27	14.30	9.81	14.20	10.49	15.20	0.13	0.00	0.00	0.00
CaO	7.74	8.32	7.85	8.25	7.70	17.16	16.82	16.78	22.26	0.18	8.87	8.90	11.01	11.28	12.04	11.52	12.07	11.58	12.24	3.27	3.85	5.73	10.91
Na_2O	0.00	0.00	0.00	0.00	0.00	3.77	4.20	3.68	1.26	0.03	3.48	1.91	2.68	2.52	0.25	0.99	0.19	1.85	0.41	9.47	9.57	8.27	5.48
K_2O	0.00	0.00	0.00	0.00	0.00	0.00	0.00	0.00	0.00	0.00	0.06	0.12	0.08	0.07	0.06	0.34	0.04	0.38	0.10	0.03	0.02	0.06	0.03
F	0.00	0.00	0.00	0.00	0.00	0.00	0.00	0.00	0.00	0.00	0.00	0.00	0.00	0.00	0.00	0.00	0.00	0.00	0.00	0.00	0.00	0.00	0.00
Cl	0.00	0.00	0.00	0.00	0.00	0.00	0.00	0.00	0.00	0.01	0.04	0.01	0.00	0.00	0.00	0.00	0.00	0.00	0.00	0.00	0.00	0.00	0.00
Total	99.13	98.97	99.32	100.02	99.97	99.79	97.66	99.41	99.65	100.62	98.46	95.73	97.68	97.30	97.52	98.66	97.99	98.73	98.26	100.85	99.62	99.83	100.73
Cations																							
Si	2.918	2.927	2.919	2.948	2.952	1.939	1.975	1.966	1.951	2.034	6.395	6.407	5.829	6.313	7.686	6.819	7.806	6.740	7.687	2.855	2.829	2.736	2.507
Ti	0.003	0.001	0.002	0.003	0.001	0.003	0.002	0.003	0.004	0.000	0.005	0.055	0.011	0.022	0.015	0.191	0.006	0.031	0.005	0.000	0.000	0.000	0.000
Cr	0.001	0.001	0.000	0.000	0.000	0.003	0.000	0.002	0.001	0.000	0.000	0.000	0.000	0.000	0.000	0.000	0.000	0.000	0.000	0.000	0.000	0.000	0.000
Al	1.996	2.023	1.989	1.968	1.971	0.276	0.271	0.312	0.088	0.010	3.085	1.990	3.174	2.258	0.413	1.583	0.310	1.839	0.495	1.141	1.148	1.266	1.486
Fe^{3+}	0.162	0.121	0.169	0.130	0.124	0.105	0.072	0.010	0.093	0.000	0.142	0.500	0.339	0.323	0.127	0.159	0.127	0.148	0.110	0.000	0.016	0.000	0.000
Fe^{2+}	1.610	1.593	1.626	1.574	1.665	0.191	0.212	0.248	0.191	1.059	1.946	1.936	2.326	2.152	1.742	2.186	1.743	2.033	1.508	0.033	0.000	0.007	0.005
Mn	0.032	0.028	0.036	0.033	0.036	0.001	0.002	0.001	0.001	0.011	0.013	0.012	0.014	0.012	0.023	0.018	0.020	0.012	0.012	0.001	0.000	0.000	0.000
Mg	0.623	0.602	0.595	0.655	0.605	0.536	0.508	0.533	0.692	0.876	1.518	2.654	1.512	2.091	3.103	2.162	3.059	2.304	3.242	0.008	0.000	0.000	0.000
Ca	0.655	0.703	0.664	0.689	0.647	0.675	0.660	0.662	0.888	0.007	1.386	1.447	1.794	1.830	1.878	1.826	1.870	1.827	1.877	0.154	0.183	0.273	0.523
Na	0.000	0.000	0.000	0.000	0.000	0.269	0.298	0.263	0.091	0.002	0.983	0.563	0.789	0.738	0.070	0.283	0.052	0.528	0.112	0.806	0.823	0.714	0.476
K	0.000	0.000	0.000	0.000	0.000	0.000	0.000	0.000	0.000	0.000	0.011	0.024	0.016	0.013	0.012	0.064	0.008	0.072	0.019	0.001	0.001	0.003	0.002
*X*Fe	0.72	0.73	0.73	0.71	0.73	0.26	0.29	0.32	0.22	0.55	0.56	0.42	0.61	0.51	0.36	0.50	0.36	0.47	0.32				
Alm (An)	0.55	0.54	0.56	0.53	0.56															0.16	0.18	0.28	0.52
Grs (Ab)	0.22	0.24	0.23	0.23	0.22															0.84	0.82	0.72	0.48
Prp (Or)	0.21	0.21	0.20	0.22	0.21															0.00	0.00	0.00	0.00
Sps (Al^{IV})	0.01	0.01	0.01	0.01	0.01						1.60	0.45	1.03	0.60									
Jd (En)						0.28	0.31	0.28	0.09	0.45					0.31	1.18	0.19	1.26	0.31				

TABLE 2 Representative mineral analyses of metagreywackes 13GB10 and 13GB01

Mineral:	Grt	Grt	Grt	Grt	St	St	Bt	Bt	Bt	Ms	Ms	Ms	Pl	Pl	Pl
Sample:	13GB10	13GB10	13GB01	13GB01	13GB10	13GB10	13GB10	13GB10	13GB01	13GB10	13GB10	13GB01	13GB10	13GB10	13GB01
Location:	Grt I	Grt II	Grt I	Grt II	Core	Rim	Inc Grt	Mtx	Mtx	Ms–Bt[a]	Ms–Chl[a]	Ms–Bt[a]	Core	Rim	Mtx
SiO_2	38.28	37.47	36.33	36.74	27.12	27.84	36.85	35.70	35.50	48.38	48.57	46.70	59.86	58.32	56.04
TiO_2	0.00	0.01	0.05	0.00	0.44	0.73	0.41	1.75	1.80	0.31	0.02	0.18	0.01	0.01	0.02
Al_2O_3	20.55	19.91	20.79	21.56	55.68	53.18	19.76	18.47	20.67	35.74	34.07	35.81	27.01	27.60	27.93
Cr_2O_3	0.03	0.01	0.02	0.08	0.00	0.00	0.00	0.00	0.00	0.00	0.00	0.00	0.00	0.00	0.00
FeO	31.49	30.72	26.36	30.59	12.96	12.37	13.57	20.69	19.65	1.43	1.12	1.20	0.05	0.11	0.13
MnO	2.29	7.70	12.49	5.46	0.42	0.41	0.15	0.16	0.24	0.01	0.04	0.00	0.01	0.00	0.03
MgO	4.64	1.67	1.37	2.65	1.32	1.33	14.99	9.85	9.17	0.51	0.13	0.52	0.00	0.00	0.00
CaO	3.83	2.49	2.73	3.25	0.00	0.00	0.00	0.00	0.00	0.00	0.02	0.00	8.79	9.72	10.32
Na_2O	0.00	0.00	0.00	0.00	0.05	0.02	0.41	0.17	0.12	0.76	0.05	0.66	6.39	5.72	5.52
K_2O	0.00	0.00	0.00	0.00	0.01	0.02	8.56	8.33	8.87	10.35	10.27	9.20	0.04	0.05	0.06
ZnO	0.00	0.00	0.00	0.00	0.00	0.00	0.00	0.00	0.00	0.00	0.00	0.00	0.00	0.00	0.00
F	0.00	0.00	0.00	0.00	0.00	0.00	0.00	0.00	0.13	0.00	0.00	0.00	0.00	0.00	0.00
Cl	0.00	0.00	0.00	0.00	0.69	0.58	0.00	0.03	0.10	0.00	0.00	0.00	0.00	0.00	0.00
Total	101.11	99.97	100.14	100.33	98.66	96.46	94.71	95.15	96.24	97.49	94.28	94.27	102.17	101.52	100.04
Cations															
Si	3.01	3.05	2.95	2.95	7.46	7.85	2.78	2.80	2.76	3.15	3.30	3.15	2.63	2.59	2.53
Ti	0.00	0.00	0.00	0.00	0.09	0.16	0.02	0.10	0.10	0.01	0.00	0.01	0.00	0.00	0.00
Cr	0.00	0.00	0.00	0.01	0.00	0.00	0.00	0.00	0.00	0.00	0.00	0.00	0.00	0.00	0.00
Al	1.91	1.91	1.99	2.04	18.06	17.68	1.76	1.71	1.89	2.75	2.73	2.85	1.40	1.45	1.48
Fe^{3+}	0.07	0.00	0.09	0.06	0.00	0.00	0.00	0.00	0.00	0.00	0.00	0.00	0.00	0.00	0.00
Fe^{2+}	1.99	2.09	1.69	1.98	2.98	2.92	0.86	1.36	1.28	0.08	0.06	0.07	0.00	0.00	0.00
Mn	0.15	0.53	0.86	0.37	0.10	0.10	0.01	0.01	0.02	0.00	0.00	0.00	0.00	0.00	0.00
Mg	0.54	0.20	0.17	0.32	0.54	0.56	1.69	1.15	1.06	0.05	0.01	0.05	0.00	0.00	0.00
Ca	0.32	0.22	0.24	0.28	0.00	0.00	0.00	0.00	0.00	0.00	0.00	0.00	0.41	0.46	0.50
Na	0.00	0.00	0.00	0.00	0.03	0.01	0.06	0.03	0.02	0.10	0.01	0.09	0.55	0.49	0.48
K	0.00	0.00	0.00	0.00	0.00	0.01	0.82	0.83	0.88	0.86	0.89	0.79	0.00	0.00	0.00
*X*Fe	0.79	0.91	0.91	0.86	0.85	0.84	0.34	0.54	0.55	0.61	0.83	0.57			
Alm (Ab)	0.66	0.69	0.57	0.67	0.82	0.82							0.57	0.51	0.49

(Continues)

TABLE 2 (Continued)

Mineral:	Grt	Grt	Grt	Grt	St	St	Bt	Bt	Bt	Ms	Ms	Ms	Pl	Pl	Pl
Sample:	13GB10	13GB10	13GB01	13GB01	13GB10	13GB10	13GB10	13GB10	13GB01	13GB10	13GB10	13GB01	13GB10	13GB10	13GB01
Location:	Grt I	Grt II	Grt I	Grt II	Core	Rim	Inc Grt	Mtx	Mtx	Ms–Bt[a]	Ms–Chl[a]	Ms–Bt[a]	Core	Rim	Mtx
Grs (An)	0.11	0.07	0.08	0.09	0.00	0.00							0.43	0.48	0.51
Prp (Or)	0.18	0.07	0.06	0.11	0.15	0.16							0.00	0.00	0.00
Sps	0.05	0.17	0.29	0.13	0.03	0.03									

Note: Grt I: garnet mantle in reequilibrated garnet. Grt II: garnet rim in reequilibrated garnet.

[a]Ms–Bt: fine-grained muscovite with biotite in S3. Ms–Chl: fine-grained muscovite with chlorite around andalusite.

around andalousite (Ms–Chl) and associated with chlorite has Si = 3.29−3.36 p.f.u. Plagioclase has a compositional range of Ab = 0.40–0.57 (Table 2).

6 | METAMORPHIC EVOLUTION

In order to constrain the metamorphic evolution of both metabasites and metagreywackes, a combined approach using Zr in rutile thermometry, conventional thermobarometry and *P–T* and *P–X* calculations has been applied to representative eclogite sample 16JS79-4, amphibolite sample 16JS79-2 and metagreywacke sample 13GB10.

6.1 | Zr in rutile thermometry for eclogite

Zr in rutile is used to constrain metamorphic temperatures based on the eclogite sample where the mineral assemblage contains both zircon and quartz. The Zr content in rutile (Tomkins, Powell, & Ellis, 2007) was used to constrain temperature in the eclogite 16JS79-4. Box plots of Zr contents and calculated temperatures at 20 and 21 kbar are shown in Figure 8 and listed in Table S1. Thirty-five rutile grains in the matrix have Zr = 226−662 ppm. Fifteen rutile grains in omphacite have Zr = 429−585 ppm. Sixteen rutile grains in garnet have Zr = 273−849 ppm (Figure 8f). At 18 kbar, for rutile inclusions in garnet, calculated temperature range is 707−813°C. At 20 kbar temperature range for rutile in matrix, in omphacite and in garnet is 701−799°C, 748−786°C and 717−824°C respectively (Figure 8g). According to Tomkins et al. (2007), a conservative estimate of the temperature might be given by the upper end of the box plot's box with a temperature uncertainty corresponding to approximately half of the interquartile. Consequently, we consider a conservative estimate of equilibration temperature for the matrix for peak metamorphism to be 770–780°C.

6.2 | Conventional thermobarometry

Temperature and pressure estimates were calculated for the eclogite 16JS79-4 and for the amphibole 16JS79-2 samples. Mineral compositions used for calculations and results are given in Table 3.

In the eclogite the following thermobarometers were applied. The Grt–Cpx thermometer of Krogh-Ravna (2000) applied to garnet mantle and matrix omphacite yields 738–755°C (±40°C). The Grt–Amp thermometer of Ravna (2000) applied to garnet rims and amphibole in eclogite symplectite yields 674–738°C (±75°C). The Grt–Amp thermometer of Graham and Powell (1984) combined to the Grt–Amp–Pl–Qz

TABLE 3 Results of conventional thermobarometry for eclogite 16JS79-4 and amphibolite 16JS79-2

Sample [mineral/textural position]	Method	Grt				Cpx		Amp			
		Grs	Prp	Alm	Sps	X_{Fe}	Jd	X_{Fe}	Al [C]	Na [B]	Na [A]
16JS79-4 [Grt-Omp/matrix]	Grt–Cpx	0.20	0.23	0.56	0.01	0.32	0.29	—	—	—	—
16JS79-4 [Grt-Omp/matrix]	Grt–Cpx	0.21	0.22	0.56	0.01	0.32	0.31	—	—	—	—
16JS79-4 [Grt-Omp/matrix]	Grt–Cpx	0.21	0.22	0.56	0.01	0.32	0.30	—	—	—	—
16JS79-4 [Grt-Amp/sympI]	Grt–Hbl	0.23	0.20	0.56	0.01	—	—	0.48	1.05	0.00	0.48
16JS79-4 [Grt-Amp/sympI]	Grt–Hbl	0.24	0.18	0.58	0.01	—	—	0.48	1.11	0.01	0.50
16JS79-4 [Grt-Amp/sympI]	Grt–Hbl	0.22	0.20	0.57	0.01	—	—	0.44	0.92	0.06	0.40
16JS79-4 [Grt-Amp/sympII]	Grt–Hbl	0.23	0.25	0.51	0.01	—	—	0.36	0.31	0.01	0.06
16JS79-4 [Grt-Amp/sympII]	Grt–Hbl	0.24	0.24	0.51	0.01	—	—	0.34	0.29	0.09	0.00
16JS79-4 [Grt-Amp/sympII]	Grt–Hbl	0.22	0.25	0.52	0.01	—	—	0.38	0.32	0.08	0.01
16JS79-2 [Amp-Pl/kelyI]	Amp–Pl	—	—	—	—	—	—	0.51	1.39	0.05	0.43
16JS79-2 [Amp-Pl/kelyII]	Amp–Pl	—	—	—	—	—	—	0.57	1.90	0.00	0.52
16JS79-2 [Amp-Pl/kelyI]	Amp–Pl	—	—	—	—	—	—	0.52	1.43	0.10	0.41
16JS79-2 [Amp-Pl/kelyII]	Amp–Pl	—	—	—	—	—	—	0.61	1.74	0.07	0.52
16JS79-2 [Amp/matrix core]	Amp	—	—	—	—	—	—	0.47	1.29	0.05	0.46
16JS79-2 [Amp/matrix core]	Amp	—	—	—	—	—	—	0.47	1.26	0.07	0.46

Note: GC-GCP after Krogh-Ravna (2000); GH20 after Ravna (2000); GP84 after Graham and Powell (1984); KS90 after Kohn and Spear (1990); HB94 after Holland and Blundy (1994); M15 after Molina et al. (2015); Hbl—*PT* after Gerya et al. (1997).

barometer of Kohn and Spear (1990) applied to garnet rims and amphibole in symplectite yield 688–727°C (±40°C) and 8.9–11.7 kbar (±0.5 kbar).

In the amphibolite the following thermobarometers were applied. The Grt–Amp thermometer of Ravna (2000) applied to garnet rims and amphibole in symplectite yields 645–707°C (±75°C). The Grt–Amp thermometer of Graham and Powell (1984) combined to the Grt–Amp–Pl–Qz barometer of Kohn and Spear (1990) applied to garnet rims and amphibole in symplectite yield 683–712°C (±40°C) and 8.7–10.4 kbar (±0.5 kbar). The Amp–Pl thermometer of Holland and Blundy (1994) combined to the barometer of Molina, Morena, Castro, Rodríguez and Fershtater (2015) applied for amphibole and plagioclase in kelyphite yield 650–707°C (±40°C) and 8.0–10 kbar (±1.5 kbar). The monomineralic geothermobarometer of Gerya, Perchuk, Troboulet, Audrem and Sez'Ko (1997) has been applied to recrystallized matrix amphibole cores where it yields 582–587°C (±37°C) and 4.5 kbar (±1.2 kbar).

6.3 | *P–T* and *P–X* calculations

In order to constrain the *P–T* evolution of the Gubaoquan eclogite and host metagreywacke, we compared the observed mineral assemblages, modes and mineral compositions as well as the textural relationships with calculated *P–T* pseudosections. Whole-rock compositions used for pseudosection calculations are given in Table S2.

Eclogite 16JS79-4, amphibolite 16JS79-2 and metagreywacke 13GB10 have been chosen for phase equilibria calculations using PerpleX version 6.8.1 software package (Connolly, 2005) with the upgraded thermodynamic database DS6.22 from Holland and Powell (2011).

Pseudosections of mafic samples are calculated for the Na_2O–CaO–FeO–MgO–Al_2O_3–SiO_2–H_2O–TiO_2–Fe_2O_3 (NCFMASHTO) system. Preliminary calculations using a MnO-bearing system result in the garnet-in boundary on the diagrams being at lower pressures compared to calculations omitting MnO in the system. No significant effect on stability or compositions of the main phases (i.e. garnet, pyroxene and amphibole) at higher pressure and temperature conditions is observed between calculated pseudosections using both systems. Therefore, because the Mn content is very low in garnet in metabasites, the Mn has been omitted in the pseudosection calculation for mafic rocks in order to simplify the calculations. The activity-solution models used are garnet, orthopyroxene and chlorite (White, Powell, Holland, Johnson, & Green, 2014), clinopyroxene, amphibole and metabasic melt (Green et al., 2016), epidote (Holland & Powell, 2011), plagioclase (Newton, Charlu, & Kleppa, 1980) and ilmenite (White, Powell, Holland, & Worley, 2000). For the pseudosections of metabasites, the Fe_2O_3 was set to be 14%

Pl		GC-GCP	GH20	GP84 + KS90		HB94 + M15		Hbl—*PT*	
Ab	An	*T* (±40°C)	*T* (±75°C)	*T* (±40 °C)	*P* (±0.5 kbar)	*T* (±40 °C)	*P* (±1.5 kbar)	*T* (±37 °C)	*P* (±1.2 kbar)
—	—	738	—	—	—	—	—	—	—
—	—	750	—	—	—	—	—	—	—
—	—	755	—	—	—	—	—	—	—
0.83	0.17	—	738	727	11.6	—	—	—	—
0.82	0.18	—	711	716	11.7	—	—	—	—
0.73	0.27	—	674	688	8.9	—	—	—	—
0.83	0.16	—	677	696	8.7	—	—	—	—
0.86	0.13	—	645	683	9.4	—	—	—	—
0.87	0.13	—	707	712	10.4	—	—	—	—
0.73	0.26	—	—	—	—	676	8.4	—	—
0.87	0.13	—	—	—	—	650	8.0	—	—
0.72	0.28	—	—	—	—	666	9.4	—	—
0.48	0.52	—	—	—	—	707	10	—	—
—	—	—	—	—	—	—	—	587	4.5
—	—	—	—	—	—	—	—	582	4.5

and 10% of the total FeO for eclogite 16JS79 and amphibolite 16JS79-2 respectively, using *P*–*X*(H_2O) and *T*–*X*(H_2O) pseudosection calculations (data not shown here). These values are compatible with the values of 13.1%–15.4% for Fe^{3+} obtained for continental eclogite samples from the Dabie orogen (Li et al., 2016) and of 9% obtained for ocean floor basalts (Rebay, Powell, & Diener, 2010; Sun & McDonough, 1989). The isopleth notations used for calculations are as follows: z(g)=Ca/(Ca+Fe^{2+}+Mg) and y(g)=Mg/(Ca+Fe^{2+}+Mg) and x(g)=Fe^{2+}/(Ca+Fe^{2+}+Mg) for garnet, j(cpx)=Na/(Na+Ca) for clinopyroxene, Ca and Mg (p.f.u.) in amphibole and ab(pl)=Na/(Na+Ca) for plagioclase.

The pseudosection for the metagreywacke 13GB10 is calculated in the MnO–Na_2O–CaO–K_2O–FeO–MgO–Al_2O_3–SiO_2–H_2O–TiO_2–O (MnNCKFMASHTO) system. The activity–solution models applied are the same as for the mafic rocks except for staurolite, biotite, white micas, melt (White et al., 2014) and alkali feldspar (Waldbaum & Thompson, 1968). H_2O is taken to be in excess. Because Fe^{3+}-rich oxides are not observed in sample 13GB10, the Fe_2O_3 (O value) has been set to 0.01 to reflect the general reduced character of the metasedimentary rocks. The isopleth notations are as follows: *X*Fe=Fe^{2+}/(Fe^{2+}+Mg), z(g)=Ca/(Ca+Fe^{2+}+Mg+Mn), m(g)=Mn/(Ca+Fe^{2+}+Mg+Mn) and y(g)=Mg/(Ca+Fe^{2+}+Mg+Mn) for garnet, Fe (p.f.u.) in staurolite and Si (p.f.u.) in muscovite. Labelled black lines indicate which mineral appears/disappears when crossing the line.

6.4 | H_2O-undersaturated P–T pseudosection for eclogite 16JS79-4

Continual fractionation of garnet during prograde growth can have significant effect on phase equilibria (e.g. Marmo, Clarke, & Powell, 2002). Calculations of garnet fractionation involving bulk-rock readjustment by garnet core removal (data not shown here) show that garnet fractionation mainly shifts the garnet-in line towards higher pressure conditions with limited effect on phase equilibria for garnet-present stability fields and on topologies of compositional isopleths of major phases. The effect of possible H_2O undersaturation was examined using *P*–*M*(H_2O) pseudosection (data not shown), which confirmed compatibility between petrological observations and predicted mineral assemblages and compositional isopleths for H_2O-undersaturated conditions.

A H_2O-undersaturated pseudosection is presented in Figure 9 and is contoured with calculated compositional isopleths for garnet, clinopyroxene, amphibole and plagioclase. Garnet includes omphacite, hornblende, plagioclase, rutile and ilmenite. These minerals have to be stable before and/or during garnet growth, suggesting a prograde *P*–*T* path from the Grt−Cpx−Hbl–Pl–Qz–Ilm–Rt and beginning of garnet growth at ~12 kbar (Figure 9a). Observed matrix assemblage Grt–Cpx–Hbl–Qz–Rt indicates peak conditions in the stability of hornblende and outside the stability field of plagioclase and at subsolidus conditions, calculated above 15–16 kbar. Rutile, ilmenite, hornblende and plagioclase inclusions in garnet

TABLE 4 Summary of the Lu–Hf and Sm–Nd isotopic results for eclogites 16JS79-4 and XIGB02

Sample label	Sample wt (mg)	Lu (ppm)	Hf (ppm)	$^{176}Lu/^{177}Hf$	$^{176}Hf/^{177}Hf$ (±2σ)	Age (Ma)	Sm (ppm)	Nd (ppm)	$^{147}Sm/^{144}Nd$	$^{143}Nd/^{144}Nd$ (±2σ)	Age (Ma)
XIGB02											
Garnet 1 (Grt-1)	94.23	0.656	0.093	1.0039	0.291413 ± 11	461.9 ± 1.6	1.558	1.555	0.6058	0.513865 ± 8	453.6 ± 2.7
Garnet 2 (Grt-2)	94.14	0.644	0.092	0.9962	0.291335 ± 8		1.509	1.663	0.5486	0.513704 ± 9	
Garnet 3 (Grt-3)	78.86	0.588	0.084	0.9966	0.291356 ± 21		1.440	1.610	0.5408	0.513687 ± 13	
Whole rock (WR)	100.20	0.377	0.646	0.0826	0.283431 ± 7		3.536	14.052	0.1521	0.512523 ± 5	
16JS79-4											
Garnet 1 (Grt-1)	75.03	0.567	0.082	0.9780	0.291026 ± 18	462.0 ± 6.2	1.892	1.936	0.5911	0.513756 ± 10	452.8 ± 3.0
Garnet 2 (Grt-2)	74.14	0.560	0.079	1.0042	0.291306 ± 19		1.803	1.604	0.6801	0.514011 ± 12	
Garnet (Grt-3)	—	—	—	—	—		1.719	1.732	0.6001	0.513787 ± 15	
Clinopyroxene (Cpx)	77.65	0.036	0.802	0.0064	0.282643 ± 4		2.318	5.896	0.2377	0.512703 ± 4	
Whole rock (WR)	100.38	0.273	0.530	0.0727	0.283197 ± 7		2.318	6.108	0.2294	0.512687 ± 8	

Note: Uncertainties on Hf and Nd isotope ratio measurements are 2*SE* (standard errors) and refer to the last significant digits. $^{176}Lu/^{177}Hf$ errors are 0.5%, JMC475 yielded 0.282162 ± 5 2*SD* (standard deviation) over the course of analyses. Mass bias correction to $^{179}Hf/^{177}Hf = 0.7325$. $^{144}Sm/^{147}Nd$ errors are 0.3%, JNd-1standard yielded 0.512102 ± 6 (2*SD*) over the course of analyses. Age calculations were conducted using decay constants $\lambda^{176}Lu = 1.865 \times 10^{-11}$ year^{-1} (Scherer et al., 2001) and $\lambda^{147}Sm = 6.02 \times 10^{-12}$ year^{-1} (Lugmair & Marti, 1978). Age uncertainties are 2σ.

(Figure 4d) suggest garnet growth from the Grt−Cpx−Hbl−Pl−Qz−Rt−Ilm stability field at 12−13 kbar and 675−700°C. In this *P*−*T* range, garnet calculated isopleths are compatible with measured garnet core composition (Grs = 0.18–0.24; Prp = 0.21–0.23; Alm = 0.54–0.58; Figure 9b,c). The presence and composition of hornblende (Ca = 1.39 p.f.u.) and plagioclase (Ab = 0.84) inclusions in garnet suggest prograde crystallization of garnet along the indicated *P*−*T* path (Figure 9e,f). Composition of garnet mantle (Grs = 0.22–0.27, Prp = 0.20–0.21 and Alm = 0.52–0.57) correlates well with garnet compositional isopleths (z(g) = 0.24, y(g) = 0.21 and x(g) = 0.55) at subsolidus conditions of 750−760°C and ~20 kbar suggesting peak assemblage in the Grt–Cpx–Hbl–Qz–Rt–H_2O stability field (Figure 9a). Compatibility between composition of matrix omphacite (Jd = 0.28–0.30) and compositional isopleths (j(cpx) = 0.28) suggest peak conditions of at least 21 kbar and ~775°C (Figure 9d).

6.5 | H_2O-undersaturated *P*–*T* pseudosection for amphibolite 16JS79-2

In order to discuss exhumation of the eclogite, we sampled an amphibolite at the rim of the main eclogite body in contact with metagreywacke (16JS79-2, Figure 10). The effect of possible H_2O saturation was examined using a *P*–*M*(H_2O) pseudosection (data not shown), which confirmed compatibility between petrological observations and predicted mineral assemblages and compositional isopleths for H_2O-undersaturated conditions. The H_2O-undersaturated pseudosection is contoured with calculated compositional isopleths for amphibole and plagioclase (Figure 10a–d).

The observed matrix assemblage is Grt–Hbl–Act–Pl–Chl–Qz–Kfs–Ilm, garnet is surrounded by amphibole–plagioclase kelyphite (kely I) and amphibole–plagioclase-K-feldspar kelyphite (kely II) and garnet fractures are filled with chlorite. The matrix is formed by recrystallized amphibole of edenitic (core) and actinolitic (rim) composition, amphibole–plagioclase symplectites.

The observed assemblage and composition of plagioclase (Ab = 0.72−0.77) and hornblende (Mg = 2.16 p.f.u.) in kelyphite I suggest its formation in the Grt−Hbl−Pl−Qz−Rt−H_2O field (Figure 10b,d). The composition of matrix hornblende core (Mg = 2.30−2.42 p.f.u.) is also compatible with growth in this field, at 10−12 kbar and 620−690°C (Figure 10b). Plagioclase (Ab = 0.42−0.47) and hornblende (Mg = 3.04−3.06 p.f.u.) composition in kelyphite II are correlated with isopleths of Mg = 3.10 p.f.u. and ab(pl) = 0.48 suggesting further re-equilibration below 4.5 kbar and 570°C in the Hbl−Act−Pl−Ilm−Qz or the Chl−Hbl−Act−Pl−Ilm−Qz fields (Figure 10c,d). Matrix actinolite rim (Mg = 3.01−3.27 p.f.u.) and presence of chlorite suggest partial re-equilibration in the

Chl–Hbl–Act–Pl–Ilm–Qz stability field at 2−3 kbar and 530–550°C (Figure 10c).

6.6 | H_2O-saturated *P–T* pseudosection for metagreywacke 13GB10

In order to discuss the metamorphic evolution of the metagreywacke and evaluate the succession of the observed assemblages and fabrics, a H_2O-saturated *P–T* pseudosection for the sample 13GB10 has been calculated (Figure 11). Because of the close whole-rock compositions of samples 13GB10 and 13GB01 the pseudosection is also used to discuss the appearance of sillimanite.

The sample 13GB10 is characterized by the presence of Grt–Ky–St–And–Bt–Ms–Pl–Qz–Chl–Rt–Ilm and a S3 fabric dominated by andalusite and biotite. Based on crystallization–deformation relationships, the assemblages contain successively Grt−Pl−Ky−Rt (presumably in the S2 fabric), followed by staurolite growth, and then in the S3 fabric by Sill−Bt and And−Bt (in samples 13GB01), followed by Chl−Ms.

Garnet core to mantle composition (Grt I, *X*Fe = 0.78–0.85, Grs = 0.08–0.10, Sps = 0.05–0.10, Prp = 0.12–0.19) and the presence of kyanite and rutile are compatible with isopleths (*X*Fe = 0.78, z(g) = 0.08, m(g) = 0.05, y(g) = 0.19) at 8–8.5 kbar and ~670°C in the Grt–Ky–Ms–Bt–Pl–Qz–Rt stability field (Figure 11a–d). Garnet thus would represent diffusionally re-equilibrated composition in the kyanite stability, not preserving a prograde garnet zoning. Relative incompatibility between muscovite compositional range (Si = 3.09–3.18 p.f.u.) and the predicted muscovite composition (Si = 3.07 p.f.u.) might also be related to re-equilibration at lower pressures (Figure 11f). Replacement of kyanite by staurolite (Fe = 2.76–3.01 p.f.u.) is compatible with decompression and cooling to ~600°C (Figure 11e). In sample 13GB01, staurolite growth is followed by sillimanite-biotite, indicating further heating to >630°C. Crystallization succession is followed by andalusite growth, compatible with decompression below 3.5 kbar. Chlorite growth in andalusite pressure shadows indicates entering to the Grt–And–Bt–Pl–Chl–Ilm–Qz stability field at ~2.5 kbar and 525–550°C (Figure 11a). Garnet rim (Grt II, *X*Fe = 0.82–0.91, Grs = 0.05–0.10, Sps = 0.07–0.18, Prp = 0.06–0.15) is compatible with predicted garnet composition at these conditions (*X*Fe = 0.91, m(g) = 0.18, z(g) = 0.05 and y(g) = 0.08; Figure 11).

7 | GARNET LU–HF AND SM–ND GEOCHRONOLOGY AND TRACE ELEMENT CHEMISTRY

Garnet trace elements analysis results for representative grains from XIGB02 and 16JS79-4 eclogites are presented in Figure 12e–h. The average Lu abundance in garnet is rather small, <1 ppm (Figure 12e,g). In both samples, Lu shows depletion in cores and small rise in mantle followed by gentle drop in concentration towards the garnet edges. Hf zonation profiles are fairly monotonous and show typical of metamorphic garnet 100–200 ppb concentration (Figure 12e,g). Large, irregular peaks or spikes in Figure 12e correspond to contamination by accessory minerals like zircon or rutile (responsible for Hf peaks). Large, irregular Sm and Nd peaks or spikes (data not shown) correspond to contamination by accessory minerals like allanite. Nd and Sm show depletion in garnet core and mantle with a significantly higher abundance in rim, which reflects a behaviour typical of incompatible elements (Figure 12f,h).

The Lu–Hf isochrons for the eclogites XIGB02 and 16JS79-4 are presented in Table 4 and Figure 12. For eclogite XIGB02, Lu–Hf isotope dilution analyses conducted on three garnet and one whole-rock fractions define an isochron of 461.9 ± 1.6 Ma (Figure 12a). Sm–Nd isotope dilution analyses on the same fractions define an isochron of 453.6 ± 2.7 Ma (Figure 12b). For eclogite 16JS79-4, Lu–Hf isotope dilution analyses conducted on two garnet, one clinopyroxene (omphacite) and whole rock fractions define an isochron of 462.0 ± 6.2 Ma (Figure 12c). Sm–Nd isotope dilution analyses on three garnet, one clinopyroxene (omphacite) and whole rock fractions define an isochron of 452.8 ± 3.0 Ma (Figure 12d).

7.1 | Interpretation of Lu–Hf and Sm–Nd garnet ages

Comparison of isotope dilution data with laser ablation ICP-MS shows very good agreement in Lu and Hf concentration estimates (Figure 12; Table 4). This demonstrates that our dating results were not significantly affected by inclusions. Garnet in both samples shows little zonation either in Lu nor in Hf, and thus the three garnet fractions yielded almost the same $^{176}Lu/^{177}Hf$ and $^{176}Hf/^{177}Hf$ ratios (Figure 12e,g). Stronger zonation is observed for Nd and Sm which show higher abundance towards the garnet edges (Figure 12f,h). Larger variations between core and rim resulted in larger spread among the analyses of garnet fractions which represent random mixtures of various, crushed garnet crystal fragments. Nevertheless, variations in $^{147}Sm/^{144}Nd$ and $^{143}Nd/^{144}Nd$ ratios are still rather modest (Figure 12; Table 4).

Notably, there is *c*. 8–11 Ma difference in ages between the two geochronometers observed in both samples. Such differences are not uncommon and have been described previously (e.g. Anczkiewicz et al., 2007; Collett et al., 2018; Kylander-Clark et al., 2007; Scherer, Cameron, & Blitcher-Toft, 2000; Smit, Scherer, Bröcker, & van Roermund, 2010; Walczak, Anczkiewicz, Szczepański, Rubatto, & Košler, 2017). They

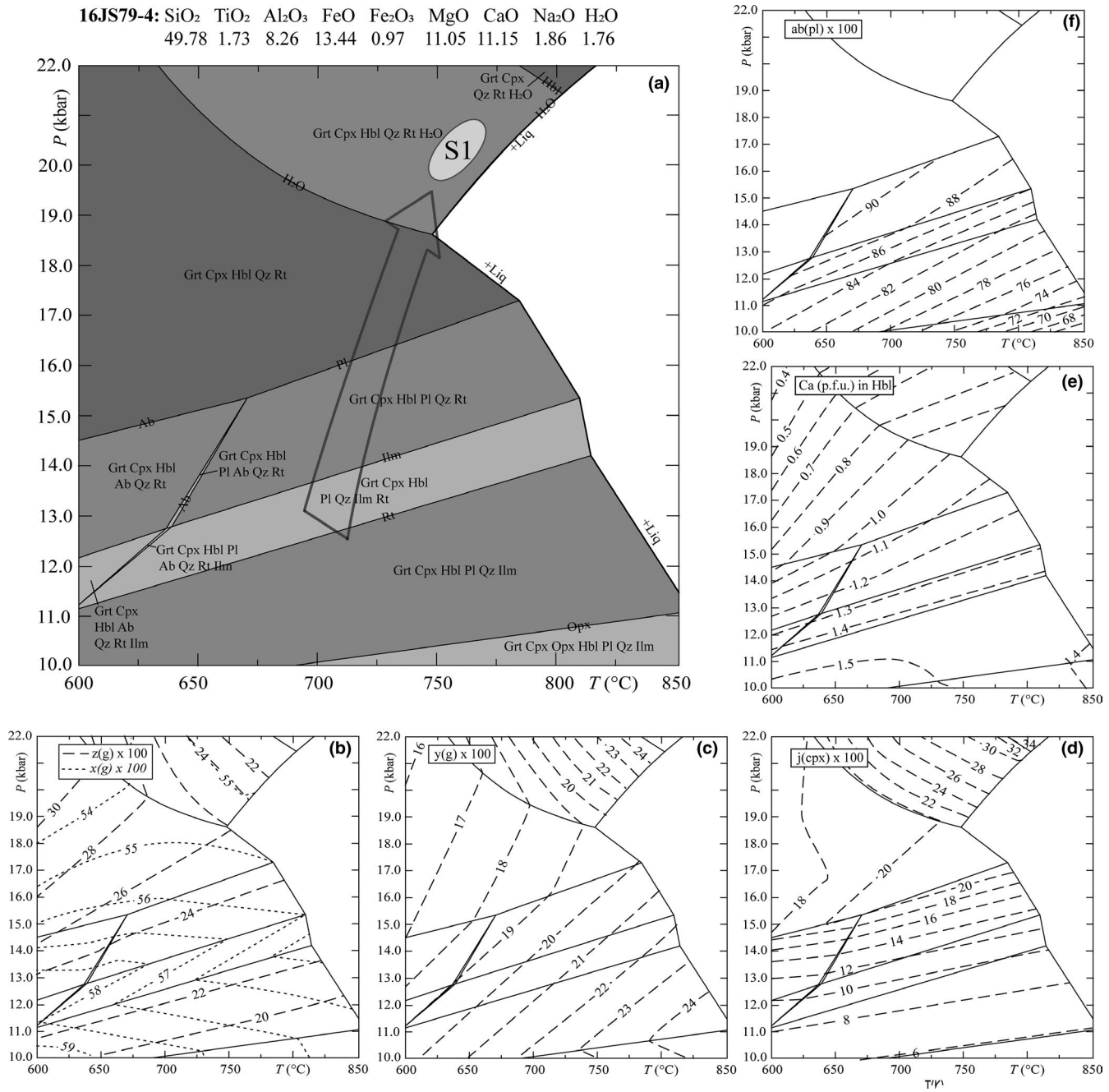

FIGURE 9 (a) *P–T* pseudosection calculated for the bulk-rock composition of the eclogite 16JS79-4. (b–f) The pseudosection contoured with calculated composition isopleths of z(g), x(g) in garnet, j(cpx) in clinopyroxene, Ca (p.f.u.) in hornblende and ab(pl) in plagioclase. The circles indicate areas of *P–T* equilibration based on comparison of the observed assemblages and mineral compositions with calculated assemblages (a) and isopleths (b–f). See text for details

can be explained either by core versus rim fractionation of Lu from Sm in garnet which underwent long-lasting crystallization (Lapen et al., 2003) or by the higher closure temperature for the Lu–Hf system compared to the Sm–Nd system (Anczkiewicz, Thirlwall, Alard, Rogers, & Clark, 2012; Scherer, Cameron, & Blichert-Toft, 2000; Walczak et al., 2017).

The Lu–Hf system in garnet, in the absence of melt and fluids, withstands temperatures in excess of 900°C (Anczkiewicz et al., 2007, Walczak et al., 2017). Thus, taking into account rather small Lu and Hf zonation in the crystals, and the ~775°C peak metamorphic temperature, we suggest that the obtained Lu–Hf ages reflect the average age of garnet formation during prograde metamorphism.

By contrast, the estimated peak temperature in the studied eclogites is at, or slightly above, the proposed closure temperature for the Sm–Nd system in garnet, estimated to be ~700 or 750°C (Tirone et al., 2005; Van Orman, Grove,

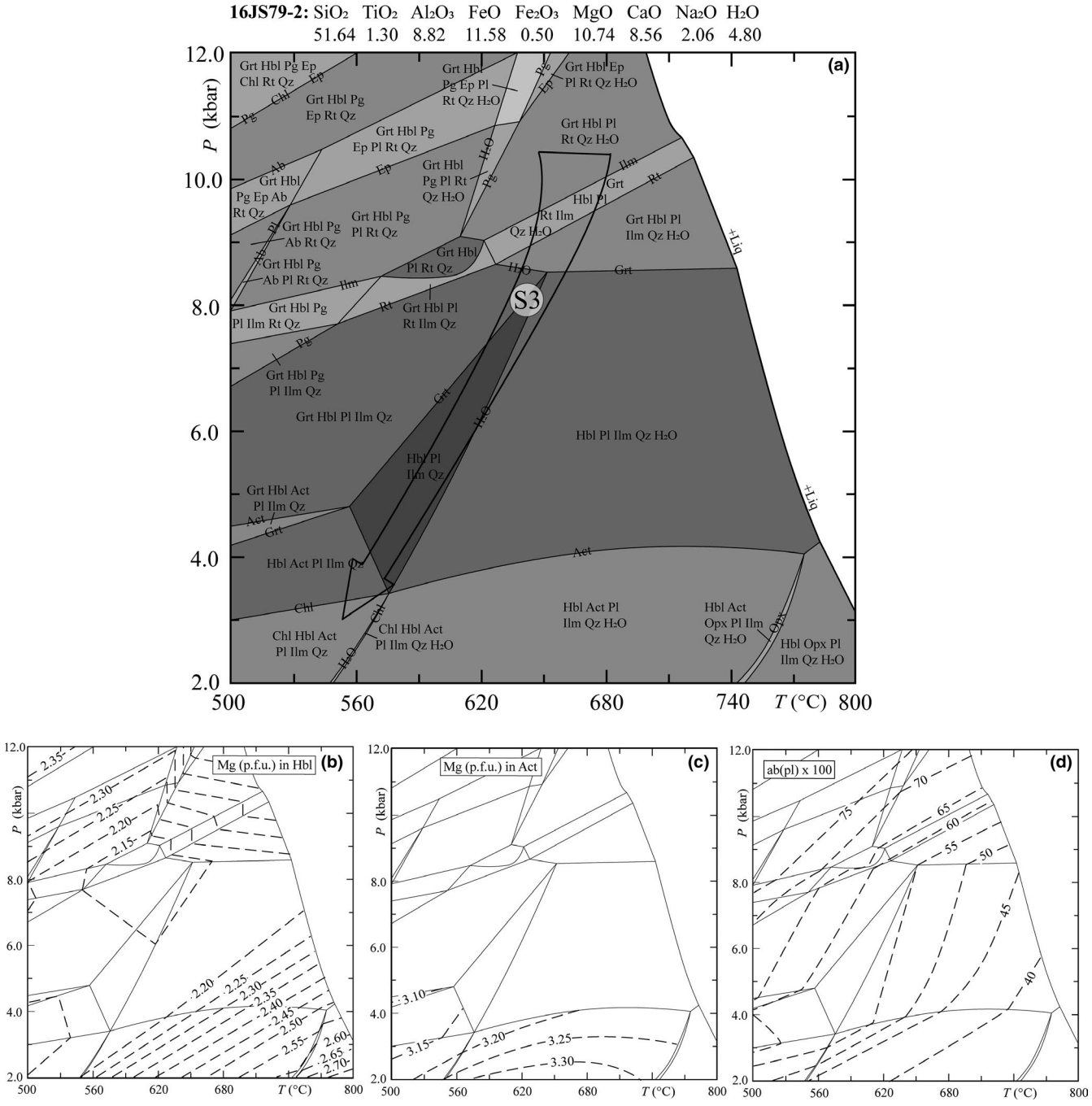

FIGURE 10 (a) *P–T* pseudosection calculated for the bulk-rock composition of the amphibolite 16JS79-2. (b–d) The pseudosection is contoured with calculated composition isopleths of z(g) in garnet, Mg (p.f.u.) in hornblende and ab(pl) in plagioclase. The circles indicate areas of *P–T* equilibration based on comparison if the observed assemblages and mineral compositions with calculated assemblages (a) and isopleths (b–d). See text for details

Shimizu, & Layne, 2002). The existence of preserved relic growth zonation in major elements combined with characteristic and locally strong zonation of garnet rims (sample 16JS79-4; Figure 12h) in Sm and Nd suggest that the Sm–Nd ages reflect crystallization near-peak conditions recorded by rims or very early cooling stage. The retrogressed rims observed in garnet from eclogite samples 16JS79-4 and XIGB04 (Figure 7a,b) are thin compared to garnet core and mantle, which crystallized under eclogite facies metamorphism. Thus, we consider that the garnet rims represent only a limited part of the volume of the garnet and that they did not affect significantly our garnet ages.

The existing U–Pb zircon data of 465 ± 10 Ma (Liu, Chen, et al., 2010; Liu, Gao, et al., 2010), 467 ± 16 Ma (Qu et al., 2011) and 466 ± 27 Ma (Saktura et al., 2017) are characterized by rather large uncertainties and are overlapping with our garnet Lu–Hf and Sm–Nd ages which provide new constraints on the timing on garnet crystallization

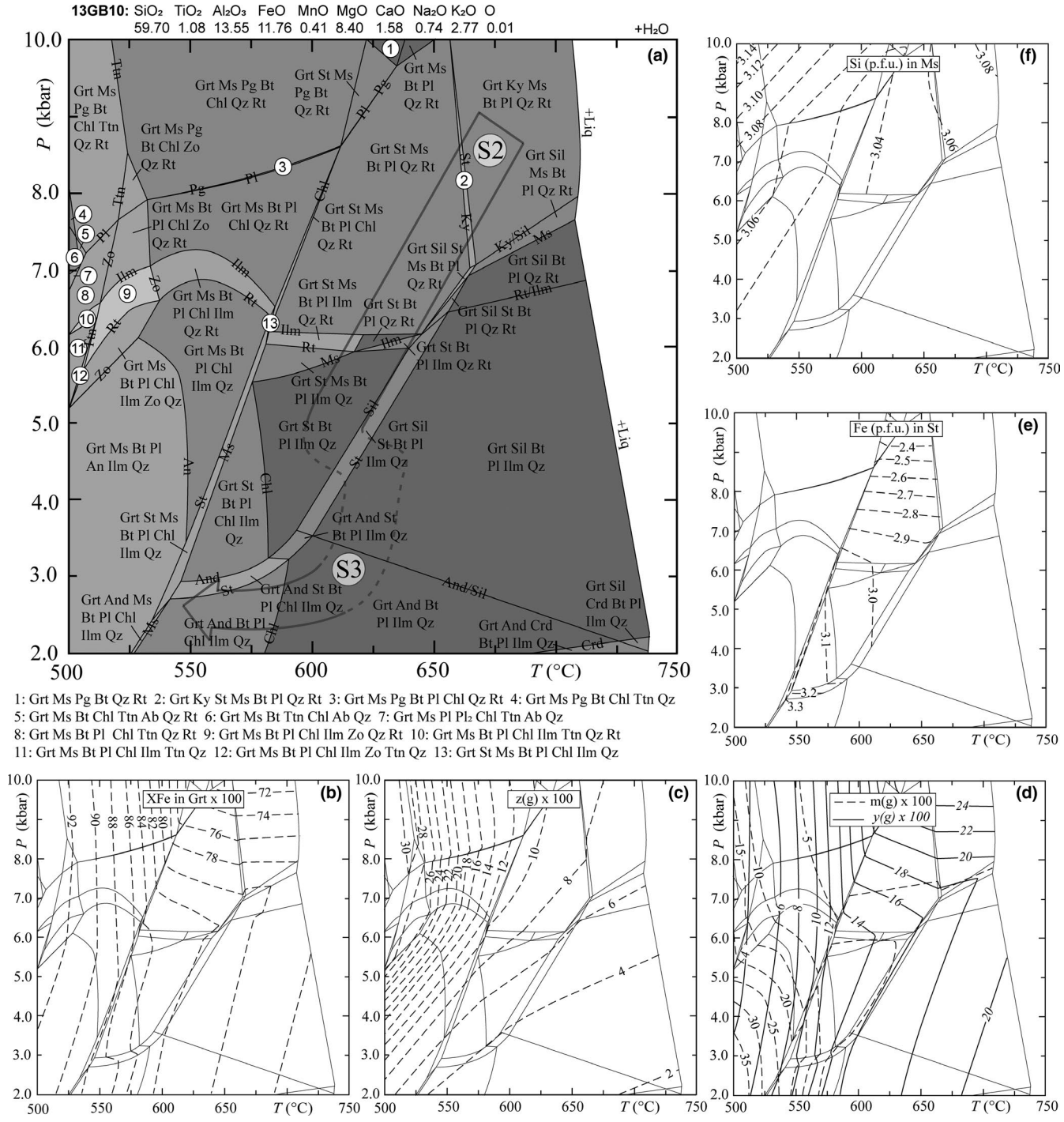

FIGURE 11 (a) *P–T* pseudosection calculated for the bulk-rock composition of the metagreywacke 13GB10. (b–f) The pseudosection is contoured with calculated garnet volume (vol.%) isopleths, compositional isopleths of *X*Fe, z(g) and m(g) in garnet, Fe (p.f.u.) in staurolite and Si (p.f.u.) in muscovite. The circles indicate areas of *P–T* equilibration based on comparison if the observed assemblages and mineral compositions with calculated assemblages (a) and isopleths (b–d). See text for details

during prograde and peak metamorphism under eclogite facies conditions. Coeval garnet and zircon crystallization during HP metamorphism is further supported by zircon/garnet trace element distribution coefficients calculated for the Gubaoquan eclogite dated at 465.0 ± 3.8 Ma in Soldner et al. (2019).

8 | MONAZITE GEOCHRONOLOGY AND TRACE ELEMENT CHEMISTRY

In metagreywacke 13GB10, 11 monazite grains were chosen for further structural, textural and geochronological studies.

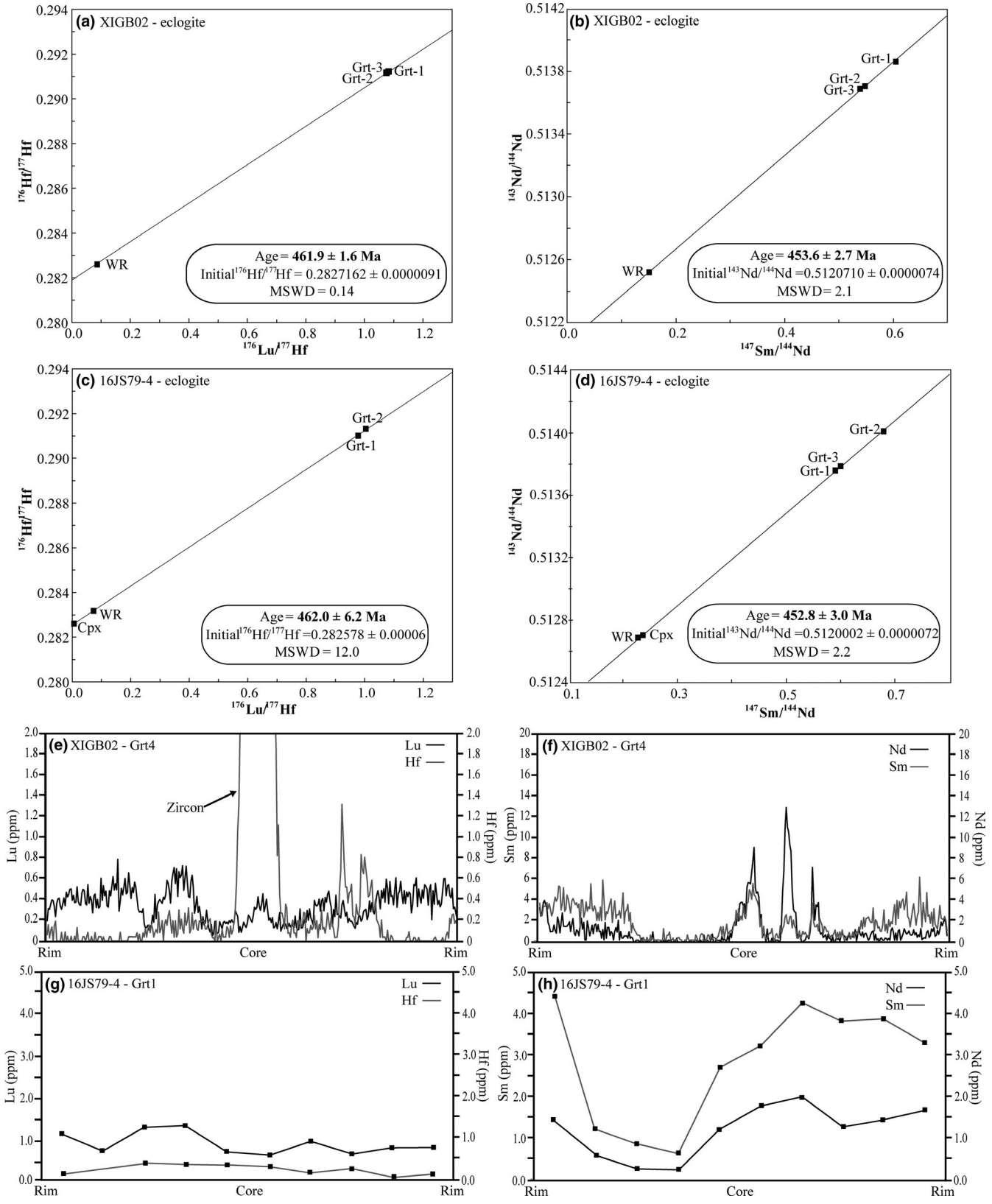

FIGURE 12 (a) Lu–Hf and (b) Sm–Nd isochrons for the eclogite XIGB02. (c) Lu–Hf and (d) Sm–Nd isochrons for the eclogite 16JS79-4. LA–ICP–MS scans along representative garnet 4 (e, f) in XIGB02, and garnet 1 in 16JS79-4 (g, h). Lu and Hf (ppm) are presented in (e,g). Sm and Nd (ppm) are presented in (f,h). (f) Hf (ppm) is also presented for a zircon inclusion in garnet 4 in XIGB02

TABLE 5 In-situ monazite U–Pb dating results in metagreywackes 13GB10 and 13GB01

		Isotope ratios								Ages						Th	U
Spot#	Type	$^{207}Pb/^{206}Pb$	±1σ	$^{207}Pb/^{235}U$	±1σ	$^{206}Pb/^{238}U$	±1σ	$^{208}Pb/^{23Th}$	±1σ	$^{207}Pb/^{235}U$	±1σ	$^{206}Pb/^{238}U$	±1σ	$^{208}Pb/^{232Th}$	±1σ	ppm	ppm
13GB10																	
YZ-1-1	Mnz rim	0.05879	0.00332	0.56865	0.03335	0.07143	0.00156	0.02340	0.00052	457	22	445	9	468	10	17,860	1,040
YZ-1-2	Mnz core	0.06066	0.00406	0.57728	0.03747	0.07151	0.00199	0.02149	0.00040	463	24	445	12	430	8	23,299	861
YZ-26-3	Mnz rim	0.05888	0.00476	0.55528	0.04111	0.07045	0.00168	0.02085	0.00036	448	27	439	10	417	7	32,805	660
YZ-24-1	Mnz rim	0.05961	0.00318	0.56398	0.02762	0.07029	0.00113	0.02157	0.00031	454	18	438	7	431	6	59,468	1,191
YZ-24-2	Mnz core	0.05985	0.00418	0.56436	0.03773	0.07089	0.00144	0.02198	0.00038	454	24	441	9	439	8	57,023	999
YZ-24-3	Mnz core	0.05565	0.00341	0.53491	0.03270	0.07048	0.00142	0.02279	0.00042	435	22	439	9	456	8	58,204	1,183
YZ-24-5	Mnz core	0.05605	0.00323	0.54636	0.03158	0.07053	0.00141	0.02054	0.00037	443	21	439	8	411	7	60,213	1,086
YZ-22-1	Mnz core	0.06109	0.00423	0.64324	0.04328	0.07815	0.00154	0.02304	0.00034	504	27	485	9	460	7	37,076	995
YZ-13-2	Mnz core	0.06062	0.00541	0.57644	0.04848	0.07077	0.00158	0.02248	0.00045	462	31	441	10	449	9	23,094	716
YZ-15-1	Mnz rim	0.05695	0.00404	0.54114	0.04018	0.06990	0.00165	0.02227	0.00053	439	26	436	10	445	11	16,484	655
XZ-10-1	Mnz core	0.06144	0.00434	0.58147	0.04345	0.07118	0.00231	0.02272	0.00056	465	28	443	14	454	11	23,869	885
XZ-11-1	Mnz core	0.05675	0.00297	0.54499	0.02786	0.07047	0.00141	0.02066	0.00044	442	18	439	8	413	9	52,443	1,141
XZ-12-1	Mnz core	0.05749	0.00315	0.54078	0.02986	0.06877	0.00154	0.02093	0.00040	439	20	429	9	419	8	53,571	1,023
XZ-19-1	Mnz core	0.06255	0.00480	0.56862	0.04265	0.07046	0.00208	0.02275	0.00055	457	28	439	13	455	11	30,960	723
XZ-21-2	Mnz rim	0.05950	0.00292	0.56159	0.02859	0.07002	0.00155	0.02210	0.00050	453	19	436	9	442	10	46,726	1,555
XZ-21-3	Mnz rim	0.05893	0.00358	0.56027	0.03709	0.06911	0.00138	0.02280	0.00062	452	24	431	8	456	12	43,554	1,163

(Continues)

TABLE 5 (Continued)

		Isotope ratios								Ages						Th	U
Spot#	Type	$^{207}Pb/^{206}Pb$	±1σ	$^{207}Pb/^{235}U$	±1σ	$^{206}Pb/^{238}U$	±1σ	$^{208}Pb/^{23Th}$	±1σ	$^{207}Pb/^{235}U$	±1σ	$^{206}Pb/^{238}U$	±1σ	$^{208}Pb/^{232Th}$	±1σ	ppm	ppm
XZ-31-1	Mnz rim	0.05912	0.00642	0.53120	0.05195	0.06928	0.00230	0.02409	0.00084	433	34	432	14	481	17	17,247	999
13GB01																	
YZ-1-2	Mnz rim	0.05965	0.00385	0.56090	0.03637	0.06963	0.00152	0.02155	0.00042	452	24	434	9	431	8	46,314	935
YZ-2-1	Mnz rim	0.05868	0.00389	0.53907	0.03468	0.06858	0.00195	0.02204	0.00047	438	23	428	12	441	9	64,511	797
YZ-2-2	Mnz core	0.06023	0.00473	0.57497	0.04161	0.07201	0.00175	0.02205	0.00039	461	27	448	11	441	8	52,278	547
YZ-7-1	Mnz rim	0.05888	0.00400	0.54717	0.03441	0.06989	0.00133	0.02180	0.00030	443	23	436	8	436	6	44,490	945
YZ-7-2	Mnz core	0.05377	0.00322	0.51407	0.03074	0.07106	0.00140	0.02166	0.00036	421	21	443	8	433	7	44,396	902
YZ-7-3	Mnz rim	0.05971	0.00380	0.54743	0.03309	0.06796	0.00133	0.02336	0.00051	443	22	424	8	467	10	30,898	1,129
YZ-9-1	Mnz rim	0.05768	0.00283	0.53353	0.02412	0.06893	0.00102	0.02199	0.00033	434	16	430	6	440	7	51,687	1,834
YZ-20-1	Mnz rim	0.05927	0.00369	0.54926	0.03237	0.06841	0.00147	0.02333	0.00038	445	21	427	9	466	8	41,791	1,407
YZ-31-1	Mnz core	0.05615	0.00313	0.55367	0.03143	0.07154	0.00141	0.02199	0.00039	447	21	445	8	440	8	57,768	1,145
YZ-32-1	Mnz rim	0.05898	0.00348	0.55034	0.03244	0.06800	0.00135	0.01947	0.00039	445	21	424	8	390	8	56,925	958
YZ-35-2	Mnz rim	0.05773	0.00404	0.52081	0.03387	0.06734	0.00144	0.02052	0.00040	426	23	420	9	411	8	46,890	858
YZ-38-2	Mnz rim	0.05922	0.00449	0.53516	0.03860	0.06823	0.00166	0.02050	0.00037	435	26	425	10	410	7	37,511	687
YZ-38-3	Mnz rim	0.05840	0.00403	0.53634	0.03404	0.06874	0.00153	0.01999	0.00035	436	23	429	9	400	7	64,568	1,039
YZ-38-4	Mnz rim	0.05936	0.00483	0.56576	0.04176	0.06955	0.00158	0.02030	0.00035	455	27	433	10	406	7	59,321	1,085
YZ-46-1	Mnz core	0.05507	0.00315	0.53600	0.03000	0.07121	0.00163	0.02056	0.00038	436	20	443	10	411	8	71,684	1,426
YZ-46-2	Mnz rim	0.05842	0.00298	0.55751	0.02897	0.06989	0.00153	0.02158	0.00039	450	19	436	9	431	8	48,976	1,144

Most grains are xenomorphic, ranging from 25 to 120 μm and have different textural positions: included in biotite (Figure 13h) and plagioclase porphyroblasts (Figure 13i,j), in contact with garnet (Figure 13g) or within the S3 fabric in the matrix (Figure S2). Core and rim spot analysis have been carried out for larger grains whereas only cores of smaller grains (<30 μm) have been analysed. Twelve spots in cores of three grains included in biotite and five grains occurring in the matrix yield $^{238}U/^{206}Pb$ ages ranging from 485.1 ± 9 Ma to 428.7 ± 9 Ma (Figure 13a; Table 5). If we consider the spot yielding the oldest age of 485.1 ± 9 Ma and the youngest age of 428.7 ± 9 Ma as outliers, a first group of monazite (Mnz cores) represented by eight spots yield a weighted mean $^{238}U/^{206}Pb$ age of 440.5 ± 6.7 Ma (Figure 13b). Six spots in monazite rims of six grains texturally mostly positioned in the S3 fabric yield $^{238}U/^{206}Pb$ ages ranging from 444.8 ± 9 Ma to 430.8 ± 8 Ma (Figure 13a; Table 5). If we consider the spot yielding the oldest age of 444.8 ± 9 Ma as an outlier, this second group of monazite (Mnz rims) yields a weighted mean $^{238}U/^{206}Pb$ age of 435.6 ± 7.3 Ma (Figure 13c). All spots in Mnz cores and Mnz rims are depleted in HREEs compared to LREEs. Mnz core and Mnz rim spots present shallow negative Eu anomalies (Eu/Eu* = 0.38–0.67; Table 6).

In metagreywacke 13GB01, 10 monazites (10–90 μm) were chosen for geochronological study. Matrix monazite is xenomorphic (Figure 13k), grains included in biotite and in plagioclase porphyroblasts are subhedral (Figure 13l). Core and rim spot analysis has been carried out for larger grains whereas only cores of smaller grains (<30 μm) have been analysed. Four spots in cores of monazite included in plagioclase, biotite and in the matrix (Mnz cores) yield $^{238}U/^{206}Pb$ ages ranging from 448.2 ± 10 Ma to 442.6 ± 8 Ma (Figure 13d; Table 5) and a weighted mean $^{238}U/^{206}Pb$ age of 444.7 ± 9.0 Ma (Figure 13e). Twelve spots from nine monazite rims of grains texturally occurring in S3 fabric (Mnz rims) yield $^{238}U/^{206}Pb$ ages ranging from 435.5 ± 8 Ma to 420.1 ± 8 Ma (Figure 13d; Table 5). Mnz rim spots yield a weighted mean $^{238}U/^{206}Pb$ age of 428.7 ± 4.9 Ma (Figure 13f).

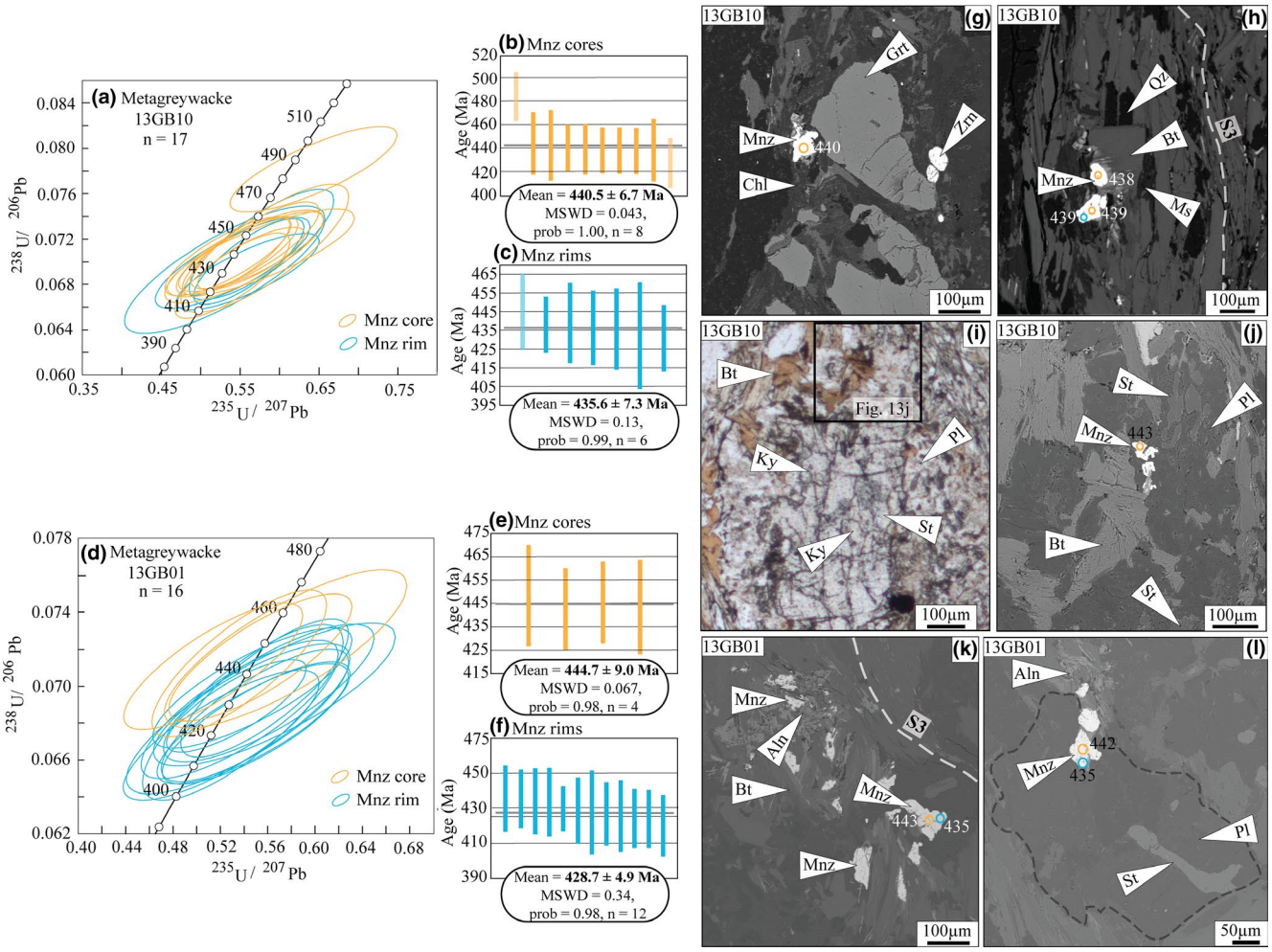

FIGURE 13 Concordia diagrams and $^{206}Pb/^{238}U$-weighted average age plots of metamorphic monazite from in sample 13GB10 (a) and in sample 13GB01 (d). Concordia diagrams and $^{206}Pb/^{238}U$-weighted average age plots of metamorphic monazite in sample 13GB10 (b, c) and in sample 13GB01 (e, f). (g–l) Thin section microphotographs and BSE images of monazite textural positions in samples 13GB10 and 13GB01. Error ellipses and error bars are 2σ in the concordia diagrams. See text for details about monazite textures and age interpretations

All spots in Mnz cores and Mnz rims are depleted in HREEs compared to LREEs. Mnz core and Mnz rim spots present shallow negative Eu anomalies (Eu/Eu* = 0.50–0.92) except for two spots in one grain included in plagioclase (Eu/Eu* = 0.10–0.11; Figure 14b; Table 6).

8.1 | Interpretation of monazite composition and age

Monazite shows rather homogeneous composition (Figure S2) and both Mnz core (439–445Ma) and Mnz rim (429–432Ma) groups have high HREE concentrations (Figure14a,b). This might imply coeval monazite crystallization and garnet breakdown according to Rubatto, Chakraborty, and Dasgupta (2013). By contrast, Mottram et al. (2014) proposed that high HREE concentrations in monazite indicate monazite rims in equilibrium with garnet rims. In all the metagreywacke samples, HREE concentrations are relatively higher than in Mottram et al. (2014) and minor to insignificant REE concentration differences are observed between garnet mantle and rim (Figure S3a,b). Thus, REE concentrations in garnet mantle (Grt I) and rim (Grt II) have been used to determine the REE distribution coefficients (K_D) between monazite and garnet. The results indicate high K_D between Mnz cores and Mnz rims and garnet mantles and rims, respectively (Figure 14c,d). According to Mottram et al. (2014), high K_D reflects equilibrium between monazite rim and garnet rim. During the retrograde path of a rock, garnet resorption results in the formation of high Y monazite grains or overgrowth (Kohn & Malloy, 2004; Pyle & Spear, 1999). However, Y contents in monazite do not significantly increase from Mnz cores to Mnz rims when plotted against metamorphic age (Figure S3c). Thus, we favour the hypothesis that Mnz cores and Mnz rims are in equilibrium with garnet mantle and rim, respectively, rather than that they reflect garnet breakdown. Equilibrium between monazite and garnet mantle is supported by the textural position of monazite grains in contact with garnet (Figure 13g) and included in plagioclase together with kyanite and staurolite (Figure 13i,j,l). Hacker, Kylander-Clark, and Holder (2018) showed that monazite–garnet pairs formed at different temperatures are characterized by different HREE partitioning coefficients. Thus, K_D can be further interpreted here in terms of temperature of crystallization. The similar K_D for Mnz core and rim in sample 13GB10 suggests that all monazite and garnet grains might have crystallized together at temperatures between 500 and 600°C (Figure 14c). In Figure14d, sample 13GB01 is characterized by higher K_D for Mnz core and garnet mantle compared to Mnz rim and garnet rim. This suggests that the pairs formed by monazite core and garnet mantle might have crystallized between 700 and 600°C which is consistent with crystallization during S2 above 5 kbar. This is supported by the textural position of monazite grains included in plagioclase together with kyanite and staurolite (Figure13i,j,l). In contrast, pairs formed by Mnz rim and garnet rim might have (re)crystallized between 600 and 500°C within S3 during late exhumation.

9 | DISCUSSION

In the following sections, structural, metamorphic, isotopic and published geochemistry data are compiled into *P–T–t–D* paths for both the Gubaoquan eclogite and host metagreywacke and then compared in order to discuss the early Palaeozoic tectonic history of the Beishan Orogen.

9.1 | Constraining *P–T–t–D* early Palaeozoic evolution

We show that there is no eclogite facies mineral fabric preserved in the Gubaoquan eclogite, which reveals mostly isotropic texture typical for HT eclogites. However, our petrological investigations show prograde metamorphic evolution from amphibolite facies at 12–13 kbar and 675–700°C to peak eclogite facies mineral assemblage M1 with estimated *P–T* conditions of 20–21 kbar and 750–775°C (Figure 15a). These data point to a scenario of progressive burial of mafic crust from initially hot field metamorphic gradient of 15°C/km to reach a gradient of 11°C/km. Such an exceptional early thermal state of mafic crust preceding HP event was so far described in the Bohemian Massif (Štípská & Powell, 2005), Athabasca granulite terrane (Dumond, Williams, Baldwin, & Jercinovic, 2017), Western Alps and Norwegian Caledonides (Austrheim 1990; Lardeaux & Spalla, 1991). In the first two cases this peculiar thermal evolution was interpreted as a thickening of previously thinned continental mafic crust in a back-arc setting during a single orogenic cycle. By contrast, the Alpine and Caledonian examples showed polycyclic eclogitization of an old granulite facies basement. For both models it is important to know the nature of the protolith of the Gubaoquan eclogite to decide whether it shows an oceanic or continental mafic lower crust affinity. The Gubaoquan eclogite protolith has been previously interpreted as originating from subducted oceanic crust due to its E-MORB and N-MORB signatures (Qu et al., 2011). However, commonly reported mid-Proterozoic protolith ages ranging from 860 to 890 Ma (Liu, Chen, et al., 2010; Liu, Gao, et al., 2010; Qu et al., 2011; Saktura et al., 2017) indicate a possible continental origin for the Gubaoquan eclogite. This hypothesis is further corroborated by (a) slightly to strongly negative whole-rock $\varepsilon_{Nd}(t)$ and $\varepsilon_{Hf}(t)$ in zircon signatures reported by Qu et al. (2011) and Soldner et al. (2019); and (b) high Nb contents, high $(Nb/La)_N$ and low Zr/Nb ratios, which are typical of back-arc basalts formed beneath

TABLE 6 Representative trace element compositions of monazite in metagreywackes 13GB10 and 13GB01

Sample	13GB10														
Spot	#10−1	#11−1	#12−1	#19−1	#21−2	#21−3	#31−1	#1−1	#1−2	#26−3	#24−1	#24−2	#24−3	#24−5	#22−1
Mnz type	Mnz core	Mnz core	Mnz core	Mnz core	Mnz rim	Mnz rim	Mnz rim	Mnz rim	Mnz core	Mnz rim	Mnz rim	Mnz core	Mnz core	Mnz core	Mnz core
(ppm)															
Y	22,167	24,254	22,534	25,355	13,554	17,969	28,359	30,975	35,285	29,071	16,562	14,604	13,649	15,518	33,957
La	145,829	144,754	143,574	140,122	147,674	140,633	137,852	188,638	188,556	197,911	192,998	198,688	196,988	188,679	175,080
Ce	269,557	252,591	259,027	262,095	268,382	269,488	249,338	289,670	277,506	289,190	289,723	302,044	301,720	296,312	281,028
Pr	28,456	25,458	26,268	26,672	27,305	27,408	24,256	31,386	32,169	32,245	33,128	32,749	33,035	31,807	31,929
Nd	104,855	102,199	103,790	105,347	106,187	104,748	97,457	122,363	119,495	127,638	127,506	124,825	124,469	125,884	120,895
Sm	21,460	19,002	18,651	19,346	18,565	20,274	23,636	30,934	30,320	27,789	24,414	23,568	23,630	23,940	28,606
Eu	3,741	3,139	3,677	4,264	3,766	4,056	4,547	4,643	4,227	5,385	4,220	3,975	4,210	4,053	5,350
Gd	24,404	22,528	18,272	22,639	14,646	16,724	30,797	40,240	37,839	25,289	17,728	16,377	16,096	16,963	31,203
Tb	3,127	3,272	2,622	3,291	1,715	2,205	4,211	5,205	4,850	2,994	2,146	1,853	1,815	1,979	4,277
Dy	10,682	12,628	9,696	11,955	6,088	8,130	14,651	16,621	17,077	11,397	7,307	6,495	6,015	6,617	15,367
Ho	1,026	1,190	965	1,228	581	813	1,292	1,518	1,731	1,349	728	663	608	682	1,570
Er	1,198	1,225	1,234	1,533	663	948	1,454	1,774	2,084	2,280	943	861	785	886	2,028
Tm	85	72	105	126	51	70	100	124	177	245	82	72	70	78	177
Yb	325	267	491	588	241	313	397	581	847	1,154	474	387	371	385	941
Lu	30	23	48	59	27	34	35	54	87	121	57	44	42	44	114
Hf	1.8	1.5	1.6	1.3	0.0	1.2	1.0	4.1	4.6	1.8	0.6	1.1	0.5	0.8	6.7
Ta	0.05	0.10	0.00	0.18	0.13	0.11	0.13	0.12	0.12	0.11	0.08	0.09	0.00	0.00	0.22
ΣREE	636,943	612,607	610,955	624,622	609,444	613,813	618,384	764,731	752,253	754,058	718,015	727,207	723,501	713,827	732,526
Eu/Eu*	0.50	0.46	0.60	0.62	0.67	0.65	0.52	0.40	0.38	0.61	0.59	0.59	0.62	0.58	0.54

Note: Normalization to chondrite in Sun and McDonough (1989). Eu/Eu* = $2*Eu_N/(Sm_N+Gd_N)$.'

stretched continental margins (Soldner et al., 2019). Therefore, and in agreement with Saktura et al. (2017), we suggest that the protolith of the Gubaoquan eclogite corresponds to mid-Proterozoic mafic lower crust that experienced HT metamorphic event prior to its thickening and eclogitization. The age of 886 ± 4 Ma for this metamorphism was previously estimated by U–Pb dating of zircon rims for which Ti-in-zircon thermometry yielded temperature of 680–710°C (Liu, Chen, et al., 2010; Liu, Gao, et al., 2010). Therefore, we propose that the studied eclogite reflects burial of an old granulitic lower crust of a mid-Proterozoic continent. The burial started at least at 462 Ma as indicated by Lu–Hf garnet ages presented in this work and peak metamorphic conditions reached ~775°C and 20–21 kbar at *c*. 453 Ma as indicated by Sm–Nd garnet ages presented in this work. Prolonged garnet and zircon crystallization during eclogite facies metamorphism inferred from our Lu–Hf and Sm–Nd ages is similar to long-lived eclogite facies metamorphic events described in North Qinling (Cheng et al., 2012) and North Qaidam (Mattinson, Wooden, Liou, Bird, & Wu, 2006).

The metamorphic conditions of the S2 fabric from conventional thermobarometry applied to garnet rims and amphibole in symplectites suggest crystallization at 9–12 kbar and 645–730°C during early retrogression (Table 3). The studied eclogite lens is surrounded by metagreywacke that shows good preservation of S2 fabric in its immediate vicinity implying that the eclogite itself experienced the D2 event. Even if the microstructural criteria for direct relationships between the S2 schistosity and growth of the index minerals are lacking, we suggest that that kyanite porphyroclasts in the S3 matrix or kyanite, rutile and staurolite inclusions in andalusite and plagioclase document their syn-D2 origin. Based on these assumptions and pseudosection calculations (Figure 11), we suggest that the D2-M2 event is marked by peak metamorphic conditions of 8–8.5 kbar and ~670°C in metagreywacke, followed by decompression to staurolite stability (Figure 15b). U–Pb ages of 445–440 Ma for Mnz core populations can be attributed to this event, which can be interpreted as a timing of maximum burial of the metagreywackes.

Our field structural study shows structural coherency of the pervasive S3 fabric in the orthogneiss, metagreywacke and in the amphibolitized rims of the studied eclogite body. The S3 fabric in the amphibolite is marked by recrystallized amphibole–plagioclase matrix for which equilibration conditions of 10−12 kbar and 620−690°C were calculated, followed by retrogression still in amphibolite facies conditions at 2−3 kbar and 530−550°C (Figure 15a). We also showed that the metagreywacke underwent retrogression from peak metamorphic conditions via the stability field of staurolite, heating to the stability field of sillimanite and subsequent

		13GB01															
#13–2	#15–1	#1–2	#2–1	#2–2	#7–1	#7–2	#7–3	#9–1	#20–1	#31–1	#32–1	#35–2	#38–2	#38–3	#38–4	#46–1	#46–2
Mnz core	Mnz rim	Mnz rim	Mnz rim	Mnz core	Mnz rim	Mnz core	Mnz rim	Mnz rim	Mnz rim	Mnz core	Mnz rim	Mnz rim	Mnz rim	Mnz rim	Mnz rim	Mnz core	Mnz rim
32,677	37,764	32,085	19,045	18,386	31,518	29,840	31,971	24,349	37,601	26,102	24,629	23,949	24,383	18,992	25,488	10,524	21,855
199,877	188,436	165,843	164,973	172,786	164,397	169,227	161,945	168,205	169,320	169,071	170,687	181,443	176,401	171,332	174,053	182,636	180,376
296,538	276,959	277,761	278,568	287,320	277,046	272,925	277,024	287,715	267,245	286,870	283,653	296,046	302,015	289,266	285,782	287,113	286,737
31,776	33,051	30,762	31,006	31,348	30,620	31,211	29,214	31,038	31,635	31,099	32,747	33,151	33,420	33,439	33,284	34,749	34,268
125,863	131,389	118,309	123,012	126,447	118,304	125,581	115,322	121,310	118,338	120,954	128,940	131,870	128,184	131,005	131,290	131,549	129,027
26,183	32,094	22,269	21,996	21,234	22,019	21,355	22,402	20,766	23,554	22,807	22,809	19,652	22,117	21,496	21,988	20,615	22,751
5,248	6,763	4,801	785	692	4,623	4,741	4,564	4,755	4,154	4,936	5,110	5,158	4,783	5,283	5,314	4,723	3,871
25,300	35,546	21,960	20,673	20,292	20,123	18,790	26,375	17,304	26,911	20,099	16,824	13,382	19,279	15,540	14,849	11,309	18,330
3,177	4,884	3,004	2,573	2,368	2,714	2,598	4,107	2,418	4,128	2,778	2,407	1,659	2,697	1,968	1,986	1,203	2,565
12,467	16,991	12,174	9,553	8,125	10,924	10,359	15,730	9,461	16,939	10,428	9,415	6,728	10,487	7,627	8,457	4,179	9,900
1,527	1,888	1,435	994	924	1,346	1,347	1,476	1,087	1688	1,201	1,103	983	1,147	839	1,042	475	986
2,494	2,326	2,185	1,441	1,302	2,532	2,498	1,987	1,763	2,269	1,804	1,806	1,918	1,636	1,331	2,105	824	1,369
249	186	222	102	103	263	253	189	172	148	173	171	201	124	143	249	86	105
1,109	855	1,032	420	389	1,290	1,235	885	924	539	890	941	1,084	603	795	1,523	584	434
115	89	115	39	37	143	146	102	100	52	106	127	128	72	98	211	66	44
0.9	1.7	1.4	0.8	1.0	0.5	1.6	0.8	2.1	1.7	2.5	1.2	0.7	1.2	2.5	1.0	0.0	1.2
0.32	0.11	0.04	0.01	0.00	0.08	0.08	0.00	0.05	0.17	0.10	0.04	0.06	0.11	0.04	0.00	0.00	0.10
764,602	769,224	693,960	675,181	691,754	687,864	692,109	693,294	691,369	704,523	699,321	701,370	717,353	727,350	699,157	707,621	690,637	712,621
0.62	0.61	0.66	0.11	0.10	0.66	0.71	0.57	0.75	0.50	0.69	0.76	0.92	0.69	0.84	0.85	0.86	0.56

retrogression to the andalusite and chlorite stability fields to ~2.5 kbar and 525–550°C (Figure 15b). The D3 deformation event therefore corresponds to a joint exhumation of both eclogite and metagreywacke. The timing of the D3 exhumation in metagreywacke is dated at 436–429 Ma using in-situ U–Pb dating of Mnz rims (Figure 15b). Due to the well-established structural continuity of S3 in metagreywacke and amphibolite as well as their coherent *P–T* evolution, we consider similar timing for the S3 development in metagreywacke and retrogressed eclogite.

The comparison of the calculated *P–T–t–D* paths for both eclogite and host metagreywacke indicates that their metamorphic evolutions are structurally and temporally decoupled or unshared during the early M1 and D2-M2 stages of the Beishan Palaeozoic orogeny. In contrast, their tectonometamorphic evolution was coupled along their retrogression during the D3 exhumation event. This complex early Palaeozoic evolution of the Beishan Orogen portrayed in Figure 16 can be explained using tectonic models applied previously for Palaeozoic continental collisional zones in Europe (e.g. Štípská et al., 2012, 2006).

The Ordovician (465–453 Ma) eclogite facies M1 metamorphism affects exclusively the mafic lower crust due to homogeneous thickening of deeply underthrust crust during continental subduction along cold gradient of 11°C/km (stage A in Figure 16a,b). This model is characteristic for eclogitization of continental crust in collisional orogens (e.g. Dewey, Ryan, & Andersen, 1993) and development of a continental wedge in which the deeply underthrust rocks are exhumed (Jolivet et al., 2005). In the studied example, the eclogitized lower crust corresponds to a Grenville age basaltic underplate formed in a back-arc setting prior to Palaeozoic orogeny (Soldner et al., 2019). After 453 Ma, early retrogression and cooling of the eclogite was associated with the onset of syn-D2 exhumation of this lower crust, while middle and upper crustal metagreywackes and gneisses were buried down to a depth of at least 30km. The juxtaposition of rocks from different crustal levels occurred along a metamorphic field gradient of 16–21°C/km (stage B in Figure16b), which corresponds to typical collisional setting as exemplified by the European Variscan belt (e.g. Chopin et al., 2012; Štípská et al., 2012, 2006). In this model the crustal-scale folding related to horizontal shortening leads to simultaneous burial of middle crust and exhumation of lower crust, that can bring the two contrasting lithologies to similar depth level. In analogy to these models, the Beishan orogeny D2 upright folding was related to formation of the penetrative S2 schistosity and passive amplification of folded lower–middle crust surface that tightly juxtaposed rocks from different crustal levels between 453 and 440 Ma (stage B in Figure 16a).

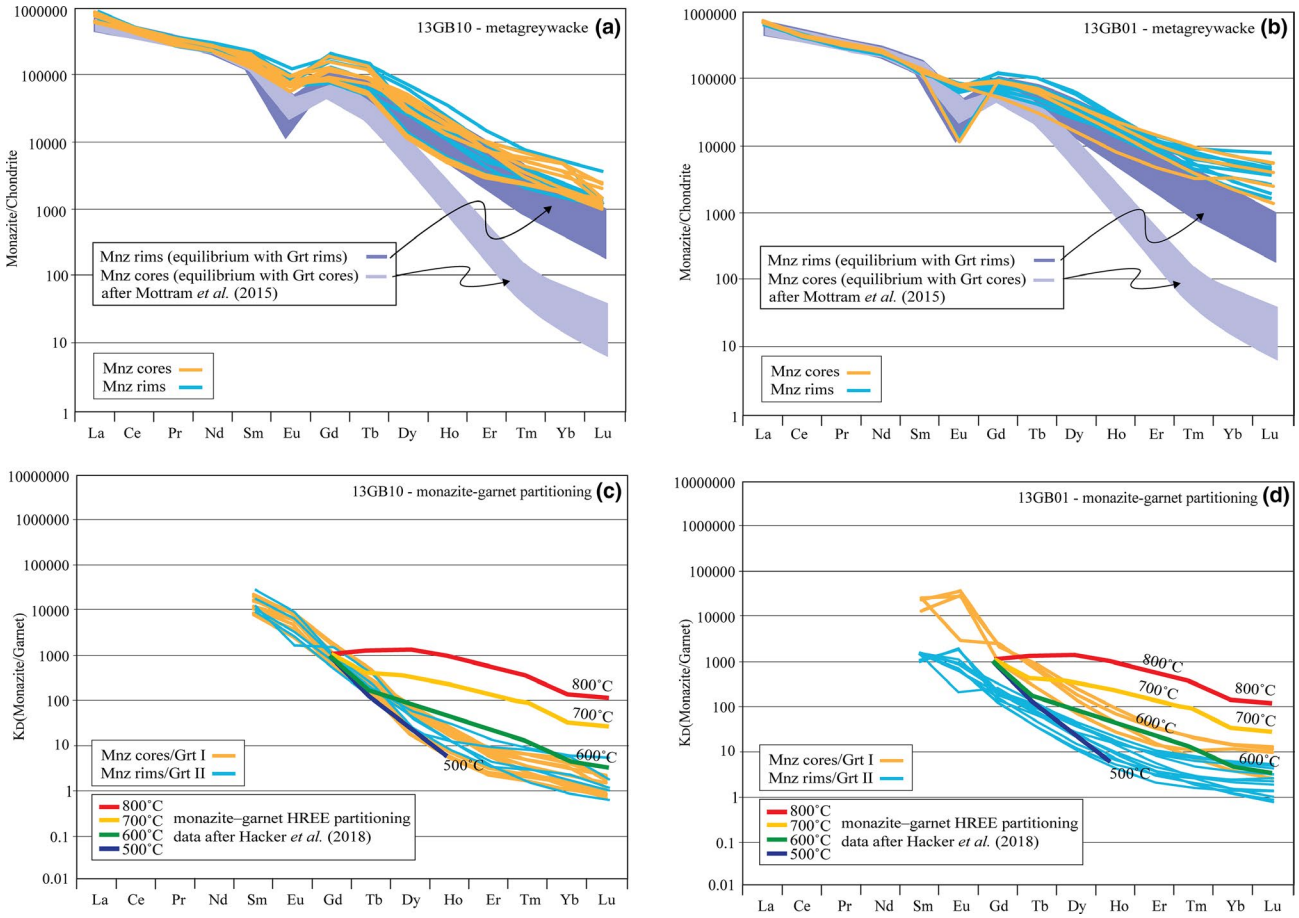

FIGURE 14 Chondrite-normalized REE patterns of metamorphic monazite in samples (a) 13GB10 and (b) 13GB01. Shown are monazite chondrite-normalized REE patterns from Mottram et al. (2014; dark and light blue). Monazite/garnet distribution coefficients (K_D) for (c) sample 13GB10 and (d) sample 13GB01. Temperature-dependent monazite–garnet HREE partitioning calculated from Y-HREE relationships from Hacker et al. (2018) are shown. See text for details

Finally, the Beishan orogeny was characterized by an episode of N–S-directed horizontal shortening responsible for the F3 folding of the steep N–S trending S2 fabric and formation of ubiquitous subvertical E–W trending fabric S3. This D3 event was accompanied by the intrusion of granodiorite in the Gubaoquan area dated at 438–424 Ma and other post-collisional granites distributed largely in the Beishan region (438–397 Ma; He, Zong, Jiang, Xiang, & Zhang, 2014; Wang et al., 2018; Yu et al., 2016; Yuan et al., 2018; Zhao, Guo, & Wang, 2007). Massive heat input related to intrusions of numerous granitoids forming more than 50% of map surface (Figure1b) is related to syn-D3 heating recorded in metagreywacke and was coeval with Buchan type syn-D3 metamorphism dated at 436–429 Ma in this study (stage C in Figure16a). At this stage metamorphic gradient reached almost 47°C/km (stage C in Figure16b) and was connected with compressional deformation, thus excluding an extensional setting. Such tectonic environment is typical for deformation of Japan-type magmatic arcs firmly established on continental crust (e.g. Žák et al., 2009). The D3 transposition led to dismembering of previously juxtaposed rocks and exhumation of the whole complex to supracrustal levels. The end of the tectonometamorphic history of the Beishan Orogen is constrained by 429 Ma biotite ^{40}Ar–^{39}Ar cooling age (Qu et al., 2011) and zircon U–Pb crystallization age of 424±8.6 Ma of undeformed leucogranitic vein (Saktura et al., 2017).

Reworking of N–S trending fabrics by E–W trending ones was reported in northern Beishan by Tian et al. (2013) and interpreted in terms of an important switch in tectonic contraction direction during Late Palaeozoic. We argue here that the last E–W trending fabric corresponds to a tectonic event (436–429 Ma) reflecting exhumation and cooling of the Beishan complex. This is supported by our petrochronological data, but also by the *c*. 429 Ma cooling of the whole system (Qu et al., 2011) while the presence of undeformed 281 Ma dolerite dykes (Zhang et al., 2015) suggests that the studied area was consolidated and unaffected by Permo-Triassic N–S shortening. Altogether, this indicates that the Beishan complex in the Gubaoquan area evolved independently of the CAOB system to the north during Early Palaeozoic.

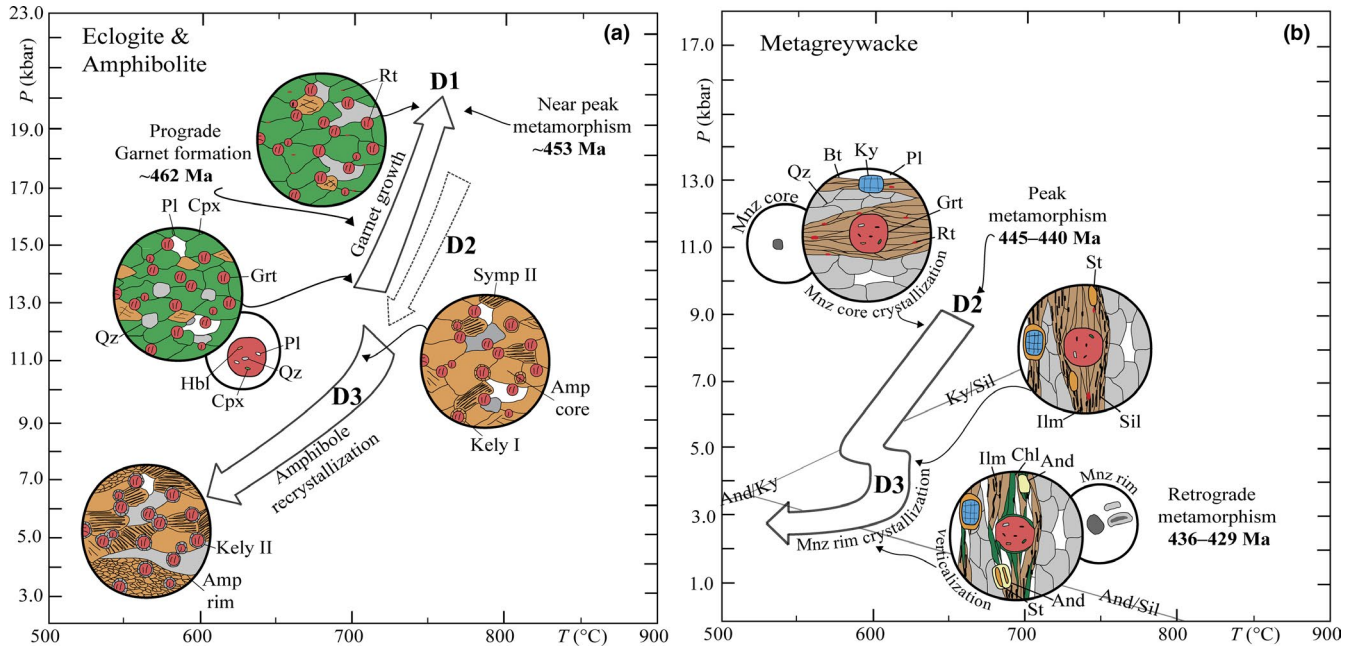

FIGURE 15 Summary of the *P–T–t–D* paths with interpretative sketches representing mineralogical successions, monazite crystallization and microstructural evolution in (a) eclogite and amphibolite and (b) host metagreywacke. *P–T* paths of all samples are from Figures 9 to 11 and constrained with garnet Lu–Hf, Sm–Nd and in-situ monazite U–Pb dating results

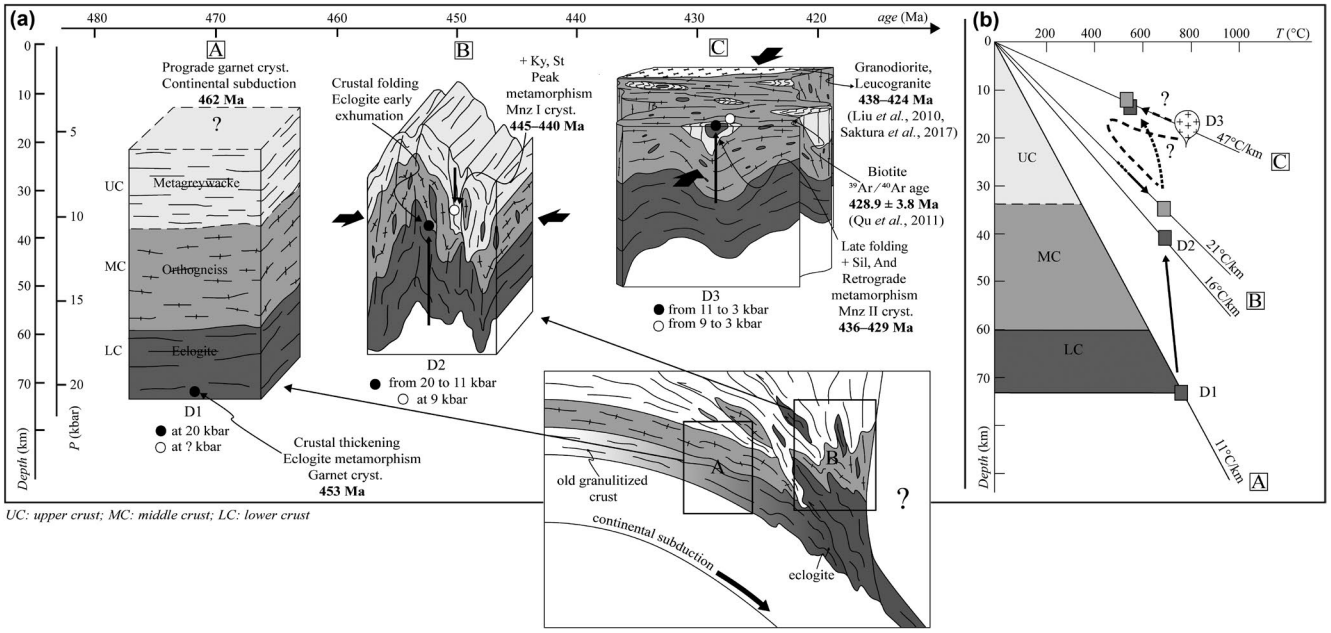

FIGURE 16 (a) Evolutionary model during stages A, B and C proposed based on crustal structures developed during the D1, D2 and D3 deformation events and partly decoupled *P–T–t–D* paths of eclogite and metagreywacke. Shown is the position of the proposed crustal model at the scale of a subducting continental crust. (b) Thermal regime during stages A, B and C and evolution of different orogenic levels of the crust during the D1, D2 and D3 deformation events

9.2 | Nature of the Beishan Orogen

The Beishan Orogen has been regarded as one of the last Palaeozoic accretionary orogen terminations in the south of the CAOB which occurred in end-Permian to early Triassic by the final closure of the Palaeo-Asian Ocean (Xiao, Huang, Han, Sun, & Li, 2010; Xiao, Mao, et al., 2010; Xiao et al., 2009, 2015). In this context, the Gubaoquan eclogite is considered as a relict of the Palaeo-Asian oceanic crust which opened in the Neoproterozoic and subducted under the Shuangyingshan (or Huaniushan) arc during Ordovician. Biotite ^{40}Ar–^{39}Ar age of *c*. 429 Ma of eclogite host gneiss

was interpreted as reflecting the final exhumation of the eclogite within the upper plate (Qu et al., 2011) whereas Nb-enriched basalt, dacite and adakite were interpreted as formed in consequence of slab melting during ongoing subduction at 451 Ma, 442 Ma and 424–374 Ma respectively (Mao, Xiao, Fang, et al., 2012; Song et al., 2016).

However, the *P–T–t–D* histories of both the Gubaoquan eclogite and host metagreywacke point to an Ordovician continental subduction or burial followed by two Silurian upright folding events. The deformation styles and *P−T* records are typically related to continental collisional setting, which is compatible with a recent recognition of Precambrian crust in the Beishan Orogen (He, Klemd, Yan, Lu, & Zhang, 2018; He, Klemd, Yan, & Zhang, 2018; Zheng et al., 2018). The tectonometamorphic evolution described in this paper is neither consistent with Pacific-type accretionary orogens (e.g. Collins, Belousova, Kemp, & Murphy, 2011) nor with Siluro-Devonian thermo-mechanical evolution proposed for the Altai part of the CAOB (e.g. Jiang et al., 2019), but resembles closely the collisional orogens such as the Variscan and Caledonian systems in Europe (e.g. Jolivet et al., 2005; Schulmann et al., 2014). The mechanism of transformation of old mafic crust into eclogite and its exhumation in form of detachment folds that are dismembered and mixed with downgoing middle crust (Figure 16a) is a characteristic mechanism for continental collisional systems (e.g. Závada et al., 2018). Based on age and position of the Beishan Orogen at the southern edge of the CAOB, it is more likely that it formed along the northern edge of Gondwana due to collision of unknown continental blocks or as an intracontinental orogen. Therefore its formation was independent of the processes forming the Kazakh and Mongolian parts of the CAOB that were in Early Palaeozoic times formed by peri-Pacific accretion (Jiang et al., 2017; Wilhem, Windley, & Stampfli, 2012).

10 | CONCLUSIONS

- Two fabrics S2 and S3 are recognized in the Gubaoquan area. S2 is a N–S trending steep fabric folded by inclined F3 folds and transposed by steep E–W trending fabric S3.
- Eclogites record a prograde *P–T* path with peak at 20–21 kbar and 750–775°C and retrogression in the amphibolite facies through 10–12 kbar and 620–690°C to 2–3 kbar and 530–550°C. The garnet-whole rock-clinopyroxene Lu–Hf ages of 461.9 ± 1.6 Ma and 462.0 ± 6.2 Ma reflect average age of garnet formation while the Sm–Nd ages of 453.6 ± 2.7 Ma and 452.8 ± 3.0 Ma reflect near-peak metamorphic crystallization.
- Metagreywackes record peak metamorphism at 8–8.5 kbar and ~670°C and retrogression to ~2.5 kbar and 525–550°C corresponding to development of the S3 fabrics. In-situ monazite U–Pb dating of Mnz cores and rims is interpreted to date the peak metamorphism and retrogression at 445–440 Ma and 436–429 Ma, respectively.
- Continental subduction (D1) initiated before *c*. 462 Ma and is responsible for the formation of the Gubaoquan eclogite. The *P−T−t−D* paths of the eclogite and metagreywacke were unshared until their juxtaposition at mid-crustal levels. This was achieved from the late Ordovician to early Silurian by a first crustal folding episode (D2). Final exhumation shared by eclogite and host rocks took place during a second Silurian crustal folding event (D3).
- The Beishan Orogen represents a collisional interior-type orogen probably located in the northern part of Gondwana.

ACKNOWLEDGEMENTS

We gratefully acknowledge the financial support of the National Key R&D Program of China (grant no. 2017YFC0601205-2), NSFC projects (41573025, 41711530147), the CNRS-NSFC project PRC1413 and the International Partnership Program of Chinese Academy of Sciences (Grant no. 132744KYSB20190039). Schulmann Karel and Štípská Pavla acknowledge the support of the Czech National Grant Agency program EXPRO (GACR 19-27682X). A Guangdong Special Support Program to Y.D. Jiang is also acknowledged. This is a contribution No. IS-2852 from GIGCAS. We are grateful to Huang Zongying, Koziarska Marta and Shu Chutian for their help with analytical work. Xing Changming, Zhang Le and Wu Dan are thanked for helping with the EDS-microprobe and LA-ICP-MS analysis and M. Racek for performing the EBSD analyses and its interpretation. Richard Palin, Wenjiao Xiao and an anonymous reviewer are thanked for their constructive reviews, and Julie Baldwin is thanked for her editorial work.

ORCID

Jérémie Soldner https://orcid.org/0000-0002-4096-431X
Pavla Štípská https://orcid.org/0000-0001-9782-9568

REFERENCES

Anczkiewicz, R., Platt, J. P., Thirlwall, M. F., & Wakabayashi, J. (2004). Franciscan subduction off to a slow start: Evidence from high-precision Lu–Hf garnet ages on high grade-blocks. *Earth and Planetary Science Letters*, *225*(1-2), 147–161. https://doi.org/10.1016/j.epsl.2004.06.003.

Anczkiewicz, R., Szczepański, J., Mazur, S., Storey, C., Crowley, Q., Villa, I. M., … Jeffries, T. E. (2007). Lu–Hf geochronology and trace element distribution in garnet: Implications for uplift and exhumation of ultra-high pressure granulites in the Sudetes, SW Poland. *Lithos*, *95*, 363–380. https://doi.org/10.1016/j.lithos.2006.09.001

Anczkiewicz, R., Thirlwall, M., Alard, O., Rogers, N. W., & Clark, C. (2012). Diffusional homogenization of light REE in garnet from the Day Nui Con Voi Massif in N-Vietnam: Implications for Sm–Nd geochronology and timing of metamorphism in the Red River shear zone. *Chemical Geology*, *318*, 16–30. https://doi.org/10.1016/j.chemgeo.2012.04.024

Andersen, T. B., Jamtveit, B., Dewey, J. F., & Swensson, E. (1991). Subduction and eduction of continental crust: Major mechanisms during continent-continent collision and orogenic extensional collapse, a model based on the south Norwegian Caledonides. *Terra Nova*, *3*, 303–310. https://doi.org/10.1111/j.1365-3121.1991.tb00148.x

Austrheim, H. (1990). The granulite eclogite facies transition: A comparison of experimental work and a natural occurrence in the Bergen Arcs, western Norway. *Lithos*, *25*, 163–169. https://doi.org/10.1016/0024-4937(90)90012-P

BGMRG (Bureau of Geology and Mineral Resources of Gansu Province) (1993). *Regional Geology of Gansu Province. People's Republic of China, Ministry of Geology and Mineral Resources: Geological Memoirs, Series 1, No. 19*. Beijing, China: Geological Publishing House, 690 pp. (in Chinese).

Brown, M. (2007). Metamorphic conditions in orogenic belts: A record of secular change. *International Geology Review*, *49*, 193–234. https://doi.org/10.2747/0020-6814.49.3.193

Cawood, P. A., Kröner, A., Collins, W. J., Kusky, T. M., Mooney, W. D., & Windley, B. F. (2009). Accretionary orogens through Earth history. *Geological Society, London*, *318*(1), 1–36. https://doi.org/10.1144/SP318.1

Cesare, B., & Grobety, B. (1995). Epitaxial replacement of kyanite by staurolite: A TEM study of the microstructures. *American Mineralogist*, *80*, 78–86. https://doi.org/10.2138/am-1995-1-208

Cheng, H., Zhang, C., Vervoort, J. D., Li, X., Li, Q., Wu, Y., & Zheng, S. (2012). Timing of eclogite facies metamorphism in the North Qinling by U-Pb and Lu–Hf geochronology. *Lithos*, *136–139*, 46–59. https://doi.org/10.1016/j.lithos.2011.06.003

Chopin, C., Henry, C., & Michard, A. (1991). Geology and petrology of the coesite-bearing terrain, Dora Maira massif, Western Alps. *European Journal of Mineralogy*, *3*, 263–292. https://doi.org/10.1127/ejm/3/2/0263

Chopin, F., Schulmann, K., Skrzypek, E., Lehmann, J., Dujardin, J. R., Martelat, J. E., … Pitra, P. (2012). Crustal influx, indentation, ductile thinning and gravity redistribution in a continental wedge: Building a Moldanubian mantled gneiss dome with underthrust Saxothuringian material (European Variscan belt). *Tectonics*, *31*, TC1013. https://doi.org/10.1029/2011TC002951

Collett, S., Štípská, P., Schulmann, K., Peřestý, V., Soldner, J., Anczkiewicz, R., … Kylander-Clark, A. (2018). Combined Lu-Hf and sm-nd geochronology of the mariánské lázně complex: New constraints on the timing of eclogite- and granulite-facies metamorphism. *Lithos*, *304–307*, 74–94. https://doi.org/10.1016/j.lithos.2018.02.007

Collins, W. J., Belousova, E. A., Kemp, A. I. S., & Murphy, J. B. (2011). Two contrasting phanerozoic orogenic systems revealed by hafnium isotope data. *Nature Geoscience*, *4*, 333–337. https://doi.org/10.1038/ngeo1127

Connolly, J. A. D. (2005). Computation of phase equilibria by linear programming: A tool for geodynamic modelling and its application to subduction zone decarbonation. *Earth and Planetary Science Letters*, *236*, 524–541.

Dewey, J. F., Ryan, P. D., & Andersen, T. B. (1993). Orogenic uplift and collapse, crustal thickness, fabrics and metamorphic phase changes: The role of eclogites. *Geological Society, London, Special Publications*, *76*(1), 325–343.

Dobretsov, N. L., & Buslov, M. M. (2007). Late Cambrian-Ordovician tectonics and geodynamics of central Asia. *Russian Geology & Geophysics*, *48*(1), 71–82. https://doi.org/10.1016/j.rgg.2006.12.006

Dumond, G., Williams, M. L., Baldwin, J. A., & Jercinovic, M. J. (2017). Backarc origin for Neoarchean ultrahigh-temperature metamorphism, eclogitization, and orogenic root growth. *Geology*, *45*, 943–946. https://doi.org/10.1130/G39254.1

Ernst, W. G. (2001). Subduction, ultrahigh-pressure metamorphism, and regurgitation of buoyant crustal slices – Implications for arcs and continental growth. *Physics of the Earth & Planetary Interiors*, *127*, 253–275. https://doi.org/10.1016/S0031-9201(01)00231-X

Ernst, W. G. (2005). Alpine and Pacific styles of Phanerozoic mountain building: Subduction-zone petrogenesis of continental crust. *Terra Nova*, *17*, 165–188.

Gao, J., & Klemd, R. (2003). Formation of HP–LT rocks and their tectonic implications in the western Tianshan Orogen, NW China: Geochemical and age constraints. *Lithos*, *66*, 1–22. https://doi.org/10.1016/S0024-4937(02)00153-6

Gao, J., Li, M., Xiao, X., Tang, Y., & He, G. (1998). Paleozoic tectonic evolution of the Tianshan Orogen, northwestern China. *Tectonophysics*, *287*, 213–231.

Gerya, T. V., Perchuk, L. L., Triboulet, C., Audrem, C., & Sez'Ko, A. I. (1997). Petrology of the Tumanshet zonal metamorphic complex, eastern Sayan. *Petrology*, *5*, 503–533.

Graham, C. M., & Powell, R. (1984). Agarnet–hornblende geothermometer: Calibration, testing, and application to the Pelona Schist, Southern California. *Journal of Metamorphic Geology*, *2*, 13–31. https://doi.org/10.1111/j.1525-1314.1984.tb00282.x

Grant, J. A., & Weiblen, P. W. (1971). Retrograde zoning in garnet near the second sillimanite isograd. *American Journal of Science*, *270*, 281–296. https://doi.org/10.2475/ajs.270.4.281

Green, E. C. R., White, R. W., Diener, J. F. A., Powell, R., Holland, T. J. B., & Palin, R. M. (2016). Activity composition relations for the calculation of partial melting equilibria for metabasic rocks. *Journal of Metamorphic Geology*, *34*, 845–869.

Guiraud, M., Powell, R., & Rebay, G. (2001). H_2O in metamorphism and unexpected behaviour in the preservation of metamorphic mineral assemblages. *Journal of Metamorphic Geology*, *19*, 445–454. https://doi.org/10.1046/j.0263-4929.2001.00320.x

Hacker, B., Kylander-Clark, A., & Holder, R. (2018). REE partitioning between monazite and garnet: Implications for petrochonology. *Journal of Metamorphic Geology*, *37*, 227–237.

Hacker, B. R., Ratschbacher, L., Webb, L., Ireland, T., Walker, D., & Shuwen, D. (1997). U/Pb zircon ages constrain the architecture of the ultrahigh-pressure Qinling-Dabie Orogen, China. *Earth and Planetary Science Letters*, *161*, 215–230. https://doi.org/10.1016/S0012-821X(98)00152-6

He, Z. Y., Klemd, R., Yan, L. L., Lu, T. Y., & Zhang, Z. M. (2018). Mesoproterozoic juvenile crust in microcontinents of the Central Asian Orogenic Belt: Evidence from oxygen and hafnium isotopes in zircon. *Scientific Reports*, *8*, 5054. https://doi.org/10.1038/s41598-018-23393-4

He, Z. Y., Klemd, R., Yan, L. L., & Zhang, Z. M. (2018). The origin and crustal evolution of microcontinents in the Beishan orogen of the southern Central Asian Orogenic Belt. *Earth-Science Reviews*, *185*, 1–14. https://doi.org/10.1016/j.earscirev.2018.05.012.

He, Z.-Y., Zong, K.-Q., Jiang, H.-Y., Xiang, H., & Zhang, Z.-M. (2014). Early Paleozoic tectonic evolution of the southern Beishan orogenic collage: Insights from the granitoids. *Acta Petrologica Sinica*, *30*, 2324–2338 (in Chinese with English abstract).

Heinrich, C. A. (1982). Kyanite-eclogite to amphibolite facies evolutionof hydrous mafic and pelitic rocks, Adula Nappe, Central Alps. *Contributions to Mineralogy and Petrology*, *81*, 30–38.

Holland, T., & Blundy, J. (1994). Non-ideal interactions in calcic amphiboles and their bearing on amphibole-plagioclase thermometry. *Contributions to Mineralogy and Petrology*, *116*, 433–447. https://doi.org/10.1007/BF00310910

Holland, T. J. B., & Powell, R. (2011). An improved and extended internally consistent thermodynamic dataset for phases of petrological interest, involving a new equation of state for solids. *Journal of Metamorphic Geology*, *29*, 333–383. https://doi.org/10.1111/j.1525-1314.2010.00923.x

Jiang, C. Y., Xia, M. Z., Yu, X., Dai, D. X., Wei, W., & Ye, S. F. (2007). Liuyuan trachybasalt belt in the northeastern Tarim Plate: Products of asthenosphere mantle decompressional melting. *Acta Petrologica Sinica*, *23*, 1765–1778. (in Chinese with English abstract).

Jiang, Y. D., Schulmann, K., Kröner, A., Sun, M., Lexa, O., Janoušek, V., … Hanžl, P. (2017). Neoproterozoic-Early Paleozoic Peri-Pacific accretionary evolution of the Mongolian Collage System: Insights from geochemical and U-Pb Zircon data from the ordovician sedimentary wedge in the Mongolian Altai. *Tectonics*, *36*, 2305–2331. https://doi.org/10.1002/2017TC004533

Jiang, Y. D., Schulmann, K., Sun, M., Weinberg, R. F., Štípská, P., Li, P. F., … Xiao, W. J. (2019). Structural and geochronological constraints on Devonian suprasubduction tectonic switching and Permian collisional dynamics in the Chinese Altai, Central Asia. *Tectonics*, *38*, 253–280. https://doi.org/10.1029/2018TC005231

Jolivet, L., Raimbourg, H., Labrousse, L., Avigad, D., Leroy, L., Austrheim, H., & Andersen, T. B. (2005). Softening triggered by eclogitization, the first step toward exhumation during continental subduction. *Earth and Planetary Science Letters*, *237*, 532–547.

Khain, E. V., Bibikova, E. V., Salnikova, E. B., Kröner, A., Gibsher, A. S., Didenko, A. N., … Fedotova, A. A. (2003). The Palaeo-Asian ocean in the Neoproterozoic and early Paleozoic: New geochronologic data and palaeotectonic reconstructions. *Precambrian Research*, *122*, 329–358.

Kohn, M. J., & Malloy, M. A. (2004). Formation of monazite via prograde metamorphic reactions among common silicates: Implications for age determinations. *Geochimica et Cosmochimica Acta*, *68*, 101–113. https://doi.org/10.1016/S0016-7037(03)00258-8

Kohn, M. J., & Spear, F. S. (1990). Two new geobarometers for garnet amphibolites, with applications to southeastern Vermont. *American Mineralogist*, *75*, 89–96.

Koons, P. O., Rubie, D. C., & Fruch-Green, G. (1987). The effects of disequilibrium and deformation on the mineralogical evolution of quartz diorite during metamorphism in the eclogite facies. *Journal of Petrology*, *28*, 679–700. https://doi.org/10.1093/petrology/28.4.679

Krogh Ravna, E. J. (2000). The garnet-clinopyroxene Fe2+-Mg geothermometer: an updated calibration. *Journal of Metamorphic Geology*, *18*, 211–219.

Kylander-Clark, A. R., Hacker, B. R., Johnson, C. M., Beard, B. L., Mahlen, N. J., & Lapen, T. J. (2007). Coupled Lu–Hf and Sm–Nd geochronology constrains prograde and exhumation histories of high-and ultrahigh-pressure eclogites from western Norway. *Chemical Geology*, *242*, 137–154. https://doi.org/10.1016/j.chemgeo.2007.03.006

Lapen, T. J., Johnson, C. M., Baumgartner, L. P., Mahlen, N. J., Beard, B. L., & Amato, J. M. (2003). Burial rates during prograde metamorphismof an ultra-high-pressure terrane: An example from Lago di Cignana, western Alps, Italy. *Earth and Planetary Science Letters*, *215*, 57–72. https://doi.org/10.1016/S0012-821X(03)00455-2

Lardeaux, J. M., & Spalla, M. I. (1991). From granulites to eclogites in the Sesia zone (Italian Western Alps): A record of the opening and closure of the Piedmont ocean. *Journal of Metamorphic Geology*, *9*, 35–59. https://doi.org/10.1111/j.1525-1314.1991.tb00503.x

Li, D. Y., Xiao, Y. L., Li, W. Y., Zhu, X., Williams, H. M., & Li, Y. L. (2016). Iron isotopic systematics of UHP eclogites respond to oxidizing fluid during exhumation. *Journal of Metamorphic Geology*, *34*, 987–997. https://doi.org/10.1111/jmg.12217

Lin, J., Liu, Y. S., Yang, Y. H., & Hu, Z. C. (2016). Calibration and correction of LA-ICP-MS and LA-MC-ICP-MS analyses for element contents and isotopic ratios. *Solid Earth Sciences*, *1*, 5–27. https://doi.org/10.1016/j.sesci.2016.04.002

Liu, X. C., Chen, B. L., Jahn, B. M., Wu, G. G., & Liu, Y. S. (2010). Early Paleozoic (ca. 465 Ma) eclogites from Beishan (NW China) and their bearing on the tectonic evolution of the southern Central Asian Orogenic Belt. *Journal of Asian Earth Sciences*, *42*, 715–731. https://doi.org/10.1016/j.jseaes.2010.10.017

Liu, X. Y., & Wang, Q. (1995). Tectonics of orogenic belts in the Beishan Mountains, western China and their evolution. *Geoscience Studies*, *28*, 37–48. (in Chinese with English abstract).

Liu, Y. S., Gao, S., Hu, Z. C., Gao, C. G., Zong, K., & Wang, D. B. (2010). Continental and oceanic crust recycling-induced melt-peridotite interactions in the trans-North China orogen: U-Pb dating, Hf isotopes and trace elements in zircons from mantle xenoliths. *Journal of Petrology*, *51*, 537–571. https://doi.org/10.1093/petrology/egp082

Liu, Y. S., Hu, Z. C., Gao, S., Gunther, D., Xu, J., Gao, C. G., & Chen, H. H. (2008). In situ analysis of major and trace elements of anhydrous minerals by LA-ICP-MS without applying an internal standard. *Chemical Geology*, *257*, 34–43. https://doi.org/10.1016/j.chemgeo.2008.08.004

Lombardo, B., & Rolfo, F. (2000). Two contrasting eclogite types in the Himalayas: Implications for the Himalayan orogeny. *Journal of Geodynamics*, *30*, 37–60. https://doi.org/10.1016/S0264-3707(99)00026-5

Ludwig, K. R. (2003). Isoplot 3.00: A geochronological toolkit for Microsoft Excel. *Berkeley Geochronology Center Special Publication*, *4*, 70–.

Lugmair, G. W., & Marti, K. (1978). Lunar initial $^{143}Nd/^{144}Nd$: Differential evolution of the lunar crust and mantle. *Earth and Planetary Science Letters*, *39*, 349–357. https://doi.org/10.1016/0012-821X(78)90021-3

Mao, Q. G., Xiao, W. J., Fang, T. H., Wang, J. B., Han, C. M., Sun, M., & Yuan, C. (2012). Late Ordovician to early Devonian adakites and Nb-enriched basalts in the Liuyuan area, Beishan, NW China: Implications for early Paleozoic slab-melting and crustal growth in the southern Altaids. *Gondwana Research*, *22*, 534–553. https://doi.org/10.1016/j.gr.2011.06.006

Mao, Q. G., Xiao, W., Windley, B. F., Han, C., Qu, J., Ao, S., … Guo, Q. (2012). The Liuyuan complex in the Beishan, NW China: A Carboniferous-Permian ophiolitic fore-arc sliver in the southern Altaids. *Geological Magazine*, *149*, 483–506. https://doi.org/10.1017/S0016756811000811

Marmo, B. A., Clarke, G. L., & Powell, R. (2002). Fractionation of bulk rock composition due to porphyroblast growth: Effects on eclogite facies mineral equilibria, Pam Peninsula, New Caledonia. *Journal of Metamorphic Geology*, *20*, 151–165. https://doi.org/10.1046/j.0263-4929.2001.00346.x

Mattinson, C. G., Wooden, J. L., Liou, J. G., Bird, D. K., & Wu, C. L. (2006). Age and duration of eclogite-facies metamorphism, North Qaidam HP/UHP Terrane, Western China. *American Journal of Science*, *306*, 678–711. https://doi.org/10.2475/09.2006.01

Mei, H. L., Yu, H. F., & Li, Q. (1997). Preliminary litho-tectonic framework of early Precambrian rocks in Dunhuang-Beishan area, Gansu,

west China. *Precambrian Research*, *20*, 47–54. (in Chinese with English abstract).

Mei, H., Yu, H., Li, Q., Lu, S., Li, H., Zuo, Y., … Liu, J. (1998). The first discovery of eclogite and Palaeoproterozoic granitoids in the Beishan area, northwestern Gansu Province, China. *Chinese Science Bulletin*, *43*, 2105–2111 (in Chinese).

Molina, J. F., Moreno, J. A., Castro, A., Rodríguez, C., & Fershtater, G. B. (2015). Calcic amphibole thermobarometry in metamorphic and igneous rocks: New calibrations based on plagioclase/amphibole Al-Si partitioning and amphibole/liquid Mg partitioning. *Lithos*, *232*, 286–305. https://doi.org/10.1016/j.lithos.2015.06.027

Mottram, C. M., Warren, C. J., Regis, D., Roberts, N. M. W., Harris, N. B. W., Argles, T. W., & Parrish, R. R. (2014). Developing an inverted Barrovian sequence: Insights from monazite petrochronology. *Earth and Planetary Science Letters*, *403*, 418–431. https://doi.org/10.1016/j.epsl.2014.07.006

Newton, R. C., Charlu, T. V., & Kleppa, O. J. (1980). Thermochemistry of the high structural state plagioclases. *Geochemica Cosmochimica Acta*, *44*, 933–941. https://doi.org/10.1016/0016-7037(80)90283-5

Nie, F. J., Jiang, S. H., Bai, D. M., Wang, X. L., Su, X. X., Li, J. C., … Zhao, X. M. (2002). *Met allogenic studies and ore prospecting in the conjunction area of inner mongolia autonomous Region, Gansu Province and Xinjiang Uygur Autonomous Region (Beishan Mt.), Northwest China*. Beijing, China: Geological Publishing House.

Orozbaev, R. T., Takasu, A., Bakirov, A. B., Tagiri, M., & Sakiev, K. S. (2010). Metamorphic history of eclogites and country rock gneisses in the Aktyuz area, Northern Tien-Shan, Kyrgyzstan: A record from initiation of subduction through to oceanic closure by continent–continent collision. *Journal of Metamorphic Geology*, *28*, 317–339. https://doi.org/10.1111/j.1525-1314.2010.00865.x

Palin, R. M., Reuber, G. S., White, R. W., Kaus, B. J. P., & Weller, O. M. (2017). Subduction metamorphism in the Himalayan ultrahigh-pressure Tso Morari massif: An integrated geodynamic and petrological modelling approach. *Earth and Planetary Science Letters*, *467*, 108–119. https://doi.org/10.1016/j.epsl.2017.03.029

Proyer, A. (2003). The preservation of high-pressure rocks during exhumation: Metagranites and metapelites. *Lithos*, *70*, 183–194. https://doi.org/10.1016/S0024-4937(03)00098-7

Pyle, J., & Spear, F. S. (1999). Yttrium zoning in garnet, coupling of major and accessory phases during metamorphic reactions. *Geological Materials Research*, *1*, 1–49.

Qu, J. F., Xiao, W. J., Windley, B. F., Han, C. M., Mao, Q. G., Ao, S. J., & Zhang, J. E. (2011). Ordovician eclogites from the Chinese Beishan: Implications for the tectonic evolution of the southern Altaids. *Journal of Metamorphic Geology*, *29*, 803–820. https://doi.org/10.1111/j.1525-1314.2011.00942.x

Ravna, E. K. (2000). Distribution of Fe^{2+} and Mg between coexisting garnet and hornblende in synthetic and natural systems: An empirical calibration of the garnet–hornblende Fe–Mg geothermometer. *Lithos*, *53*, 265–277. https://doi.org/10.1016/S0024-4937(00)00029-3

Rebay, G., Powell, R., & Diener, J. F. A. (2010). Calculated phase equilibria for a MORB composition in a P-T range, 450–650°C and 18–28 kbar: The stability of eclogite. *Journal of Metamorphic Geology*, *28*, 635–645.

Rubatto, D., Chakraborty, S., & Dasgupta, S. (2013). Time scales of crustal melting in the Higher Himalayan Crystallines (Sikkim, Eastern Himalaya) inferred from trace element-constrained monazite and zircon chronology. *Contributions to Mineralogy and Petrology*, *165*, 349–372. https://doi.org/10.1007/s00410-012-0812-y

Rubie, D. C. (1986). The catalysis of mineral reactions by water and restrictions on the presence of aqueous fluid during metamorphism. *Mineralogical Magazine*, *50*, 399–415. https://doi.org/10.1180/minmag.1986.050.357.05

Safonova, I. Y., & Santosh, M. (2014). Accretionary complexes in the Asia-Pacific region: Tracing archives of ocean plate stratigraphy and tracking mantle plumes. *Gondwana Research*, *25*, 126–158. https://doi.org/10.1016/j.gr.2012.10.008

Saktura, W. M., Buckman, S., Nutman, A. P., Belousova, E. A., Yan, Z., & Aitchison, J. C. (2017). Continental origin of the Gubaoquan eclogite and implications for evolution of the Beishan Orogen, Central Asian Orogenic Belt, NW China. *Lithos*, *294–295*, 20–38. https://doi.org/10.1016/j.lithos.2017.10.004

Scherer, E. E., Cameron, K. L., & Blichert-Toft, J. (2000). Lu–Hf garnet geochronology: Closure temperature relative to the Sm–Nd system and the effects of trace mineral inclusions. *Geochimica et Cosmochimica Acta*, *64*, 3413–3432. https://doi.org/10.1016/S0016-7037(00)00440-3

Scherer, E., Munker, C., & Mezger, K. (2001). Calibration of the lutetiul-hafnium clock (vol. 293, 693, 2001). *Science*, *293*, 1766–1766.

Schulmann, K., Lexa, O., Janousek, V., Lardeaux, J. M., & Edel, J. B. (2014). Anatomy of a diffusive cryptic suture zone: An example from the Bohemian Massif, European Variscides. *Geology*, *42*, 275–278.

Smit, M. A., Scherer, E. E., Bröcker, M., & vanRoermund, H. L. (2010). Timing of eclogite facies metamorphism in the southernmost Scandinavian Caledonides by Lu–Hf and Sm–Nd geochronology. *Contributions to Mineralogy and Petrology*, *159*, 521–539. https://doi.org/10.1007/s00410-009-0440-3

Soldner, J., Yuan, C., Schulmann, K., Štípská, P., Jiang, Y., Zhang, Y., & Wang, X. (2019). Grenvillean evolution of the Beishan Orogen, NW China: Implications for development of an active Rodinian margin. *Geological Society of America Bulletin*.

Song, D., Xiao, W., Windley, B. F., Han, C., & Yang, L. (2016). Metamorphic complexes in accretionary orogens: Insights from the Beishan collage, southern Central Asian Orogenic Belt. *Tectonophysics*, *688*, 135–147. https://doi.org/10.1016/j.tecto.2016.09.012

Štípská, P., Chopin, F., Skrzypek, E., Schulmann, K., Pitra, P., Lexa, O., … Žáčková, E. (2012). The juxtaposition of eclogite and mid-crustal rocks in the Orlica-Śnieżnik dome, Bohemian Massif. *Journal of Metamorphic Geology*, *30*(2), 213–234. https://doi.org/10.1111/j.1525-1314.2011.00964.x

Štípská, P., Hasalová, P., Powell, R., Závada, P., Schulmann, K., Racek, M., … Chopin, F. (2019). The effect of melt infiltration on metagranitic rocks: The Śnieżnik dome, Bohemian Massif. *Journal of Petrology*, *60*, 591–618.

Štípská, P., Pitra, P., & Powell, R. (2006). Separate or shared metamorphic histories of eclogites and surrounding rocks? An example from the bohemian massif. *Journal of Metamorphic Geology*, *24*, 219–240. https://doi.org/10.1111/j.1525-1314.2006.00634.x

Štípská, P., & Powell, R. (2005). Constraining the P-T path of a Morb-type eclogite using pseudosections, garnet zoning and garnet-clinopyroxene thermometry: An example from the Bohemian massif. *Journal of Metamorphic Geology*, *238*, 725–743. https://doi.org/10.1111/j.1525-1314.2005.00607.x

Štípská, P., Schulmann, K., Lehmann, C., Lexa, M. J., & Tomurhuu, O. (2010). Early Cambrian eclogites in SW Mongolia: Evidence that the Paleo-Asian Ocean suture extends further east than expected. *Journal of Metamorphic Geology*, *28*, 915–933.

Štípská, P., Schulmann, K., & Powell, R. (2008). Contrasting metamorphic histories of lenses of high-pressure rocks and host migmatites with a flat orogenic fabric (Bohemian Massif, Czech Republic): A result of tectonic mixing within horizontal crustal flow?*Journal of Metamorphic Geology*, *26*, 623–646. https://doi.org/10.1111/j.1525-1314.2008.00781.x

Sun, S. S., & McDonough, W. F. (1989). Chemical and isotopic systematics of oceanic basalts: Implications for mantle composition and processes. *Geological Society of London Special Publication*, *42*, 313–345. https://doi.org/10.1144/GSL.SP.1989.042.01.19

Thirlwall, M. F., & Anczkiewicz, R. (2004). Multidynamic isotope ratio analysis using MC–ICP– MS and the causes of secular drift in Hf, Nd and Pb isotope ratios. *International Journal of Mass Spectrometry*, *235*, 59–81. https://doi.org/10.1016/j.ijms.2004.04.002

Tian, Z., Xiao, W., Shan, Y., Windley, B., Han, C., Zhang, J. E., & Song, D. (2013). Mega-fold interference patterns in the Beishan orogen (NW China) created by change in plate configuration during Permo-Triassic termination of the Altaids. *Journal of Structural Geology*, *52*, 119–135. https://doi.org/10.1016/j.jsg.2013.03.016

Tirone, M., Ganguly, J., Dohmen, R., Langenhorst, F., Hervig, R., & Becker, H. W. (2005). Rare earth diffusion kinetics in garnet: Experimental studies and applications. *Geochimica et Cosmochimica Acta*, *69*, 2385–2398. https://doi.org/10.1016/j.gca.2004.09.025

Tomkins, H. S., Powell, R., & Ellis, D. J. (2007). The pressure dependence of the zirconium-in rutile thermometer. *Journal of Metamorphic Geology*, *25*, 703–713. https://doi.org/10.1111/j.1525-1314.2007.00724.x

Tuccillo, M. E., Essene, E. J., & van derPlujim, B. A. (1990). Growth and retrograde zoning in garnets from high-grade metagreywackes: Implications for pressure-temperature paths. *Geology*, *18*, 839–942.

Van Orman, J. A., Grove, T. L., Shimizu, N., & Layne, G. D. (2002). Rare earth element diffusion in a natural pyrope single crystal at 2.8 GPa. *Contributions to Mineralogy and Petrology*, *142*, 416–424.

Volkova, N. I., & Sklyarov, E. V. (2007). High-pressure complexes of Central Asian Fold Belt: Geologic setting, geochemistry, and geodynamic implications. *Russian Geology and Geophysics*, *48*, 83–90. https://doi.org/10.1016/j.rgg.2006.12.008

Walczak, K., Anczkiewicz, R., Szczepański, J., Rubatto, D., & Košler, J. (2017). Combined garnet and zircon geochronology of the ultra-high temperatures metamorphism: Constraints on the rise of the Orlica-Śnieżnik Dome, NE Bohemian Massif, SW Poland. *Lithos*, *292–293*, 388–400.

Waldbaum, D. R., & Thompson, J. B. (1968). Mixing properties of Sanidine crystalline solutions. 2. Calculations based on volume data. *American Mineralogist*, *53*, 2000–2017.

Wang, X., Yuan, C., Zhang, Y., Long, X., Sun, M., Wang, L., … Lin, Z. (2018). S-type granite from the Gongpoquan arc in the Beishan Orogenic Collage, southern Altaids: Implications for the tectonic transition. *Journal of Asian Earth Sciences*, *153*, 206–222. https://doi.org/10.1016/j.jseaes.2017.07.037

White, R. W., Powell, R., Holland, T. J. B., Johnson, T. E., & Green, E. C. R. (2014). New mineral activity–composition relations for thermodynamic calculations in metapelitic systems. *Journal of Metamorphic Geology*, *32*, 261–286. https://doi.org/10.1111/jmg.12071

White, R. W., Powell, R., Holland, T. J. B., & Worley, B. A. (2000). The effect of TiO_2 and Fe_2O_3 on metapelitic assemblages at greenschist and amphibolite facies conditions: Mineral equilibria calculations in the system K_2O-FeO-MgO-Al_2O_3-SiO_2-H_2O-TiO_2-Fe_2O_3. *Journal of Metamorphic Geology*, *18*, 497–511. https://doi.org/10.1046/j.1525-1314.2000.00269.x

Whitney, D. L., & Evans, B. W. (2010). Abbreviations for names of rock-forming minerals. *American Mineralogist*, *95*, 185–187. https://doi.org/10.2138/am.2010.3371

Whitney, D., Teyssier, C., Toraman, E., Seaton, N. C. A., & Fayon, A. K. (2011). Metamorphic and tectonic evolution of a structurally continuous blueschist-to-Barrovian terrane, Sivrihisar Massif, Turkey. *Journal of Metamorphic Geology*, *29*, 193–212. https://doi.org/10.1111/j.1525-1314.2010.00915.x

Wilhem, C., Windley, B. F., & Stampfli, G. M. (2012). The Altaids of central Asia: A tectonic and evolutionary innovative review. *Earth-Science Reviews*, *113*, 303–341. https://doi.org/10.1016/j.earscirev.2012.04.001

Xiao, W., Huang, B., Han, C., Sun, S., & Li, J. (2010). A review of the western part of the Altaids: A key to understanding the architecture of accretionary orogens. *Gondwana Research*, *18*, 253–273. https://doi.org/10.1016/j.gr.2010.01.007

Xiao, W. J., Mao, Q. G., Windley, B. F., Han, C. M., Qu, J. F., Zhang, J. E., … Li, J. L. (2010). Paleozoic multiple accretionary and collisional processes of the Beishan orogenic collage. *American Journal of Science*, *310*, 1553–1594. https://doi.org/10.2475/10.2010.12

Xiao, W., Windley, B., Huang, B., Han, C., Yuan, C., Chen, H., … Li, J. (2009). End-Permian to mid-Triassic termination of the accretionary processes of the southern Altaids: Implications for the geodynamic evolution, Phanerozoic continental growth, and met allogeny of Central Asia. *International Journal of Earth Sciences*, *98*, 1189–1217. https://doi.org/10.1007/s00531-008-0407-z

Xiao, W., Windley, B. F., Sun, S., Li, J., Huang, B., & Han, C. (2015). A tale of amalgamation of three Permo-Triassic collage systems in Central Asia: oroclines, sutures, and terminal accretion. *Annual Review of Earth and Planetary Sciences 43*(1), 477–507.

Yang, J. S., Wu, C. L., Chen, S. Y., Shi, R. D., & Zhang, J. X. (2006). Neoproterozoic eclogitic metamorphic age of the Beishan eclogite of Gansu, China: Evidence from SHRIMP U-Pb isotope dating. *Geology in China*, *33*, 317–325. (in Chinese with English abstract).

Young, D. J., & Kylander-Clark, A. R. C. (2015). Does crust transform during eclogite facies metamorphism?*Journal of Metamorphic Geology*, *33*, 331–357.

Yu, J., Guo, L., Li, J., Li, Y., Smithies, R. H., Wingate, M. T., … Chen, S. (2016). The petrogenesis of sodic granites in the Niujuanzi area and constraints on the Paleozoic tectonic evolution of the Beishan region, NW China. *Lithos*, *256*, 250–268. https://doi.org/10.1016/j.lithos.2016.04.003

Yuan, Y., Zong, K., He, Z., Klemd, R., Jiang, H., Zhang, W., … Zhang, Z. (2018). Paleozoic crustal growth and tectonic evolution of the Northern Beishan Orogen, southern Central Asia Orogenic Belt. *Lithos*, *302*, 189–202.

Žák, J., Dragoun, F., Verner, K., Chlupáčová, M., Holub, F. V., & Kachlík, V. (2009). Forearc deformation and strain partitioning during growth of a continental magmatic arc: The northwestern margin of the Central Bohemian Plutonic Complex, Bohemian Massif. *Tectonophysics*, *469*, 93–111. https://doi.org/10.1016/j.tecto.2009.01.035

Závada, O., Schulmann, K., Racek, M., Hasalová, P., Jeřábek, P., Weinberg, R. F., … Roberts, A. (2018). Role of strain localization and melt flow on exhumation of deeply subducted continental crust. *Lithosphere*, *10*, 217–238. https://doi.org/10.1130/L666.1

Zhang, Y., Yuan, C., Sun, M., Long, X., Xia, X., Wang, X., & Huang, Z. Y. (2015). Permian doleritic dikes in the Beishan Orogenic Belt, NW

China: Asthenosphere–lithosphere interaction in response to slab breakoff. *Lithos*, *233*, 174–192. https://doi.org/10.1016/j.lithos.2015.04.001

Zhao, Z. H., Guo, Z. J., Han, B. F., Wang, Y., & Liu, C. (2006). Comparative study on Permian basalts from eastern Xinjiang-Beishan area of Gansu province and its tectonic implications. *Acta Petrologica Sinica*, *22*, 1279–1293. (in Chinese with English abstract).

Zhao, Z., Guo, Z., & Wang, Y. (2007). Geochronology, geochemical characteristics and tectonic implications of the granitoids from Liuyuan area, Beishan, Gansu province, Northwest China. *Acta Petrologica Sinica*, *23*, 1847–1860 (in Chinese with English abstract).

Zheng, R., Li, J., Xiao, W., & Zhang, J. (2018). Nature and provenance of the Beishan complex, southernmost Central Asian Orogenic Belt. *International Journal of Earth Sciences*, *4*, 1–27. https://doi.org/10.1007/s00531-017-1525-2

Zong, K., Klemd, R., Yuan, Y., He, Z., Guo, J., Shi, X., … Zhang, Z. (2017). The assembly of Rodinia: The correlation of early Neoproterozoic (ca. 900 Ma) high-grade metamorphism and continental arc formation in the southern Beishan Orogen, southern Central Asian Orogenic Belt (CAOB). *Precambrian Research*, *290*, 32–48. https://doi.org/10.1016/j.precamres.2016.12.010

Zuo, G. C., Liu, Y. K., & Liu, C. Y. (2003). Framework and evolution of the tectonic structure in Beishan area across Gansu Province, Xinjiang Autonomous region and Inner Mongolia Autonomous Region. *Acta Geologica Gansu*, *12*, 1–15 (in Chinese with English abstract).

Zuo, G. C., Zhang, S. L., He, G. Q., & Zhang, Y. (1991). Plate tectonic characteristics during the early Paleozoic in Beishan near the Sino-Mongolian border region, China. *Tectonophysics*, *188*, 385–392. https://doi.org/10.1016/0040-1951(91)90466-6

Zuo, G. C., Zhang, S. L., Wang, X., Jin, S. Q., He, G. Q., Zhang, Y., … Bai, W. C. (1990). *Plate Tectonics and Met allogenic Regularities in Beishan Region*. Beijing, China: Peking University Publishing House, 226 pp.

SUPPORTING INFORMATION

Additional supporting information may be found online in the Supporting Information section.

Figure S1. (a) BSE image of epitaxial staurolite around kyanite in sample 13GB10. Kikuchi bands of (b) staurolite rims and (c) kyanite cores.

Figure S2. BSE images and compositional maps of analyzed detrital and metamorphic monazite grains in metagreywacke 13GB10 and 13GB01.

Figure S3. Chondrite-normalized REE patterns of garnet in samples (a) 13GB10 and (b) 13GB01. (c) Y versus age diagram for metamorphic monazite in samples 13GB10 and 13GB01.

Table S1. Zr in rutile contents and calculated temperatures from thermometry for eclogite 16JS79-4.

Table S2. Major element compositions of eclogite, amphibolite and metagreywacke.

Appendix S1. Analytical methods.

How to cite this article: Soldner J, Štípská P, Schulmann K, et al. Coupling of *P–T–t–D* histories of eclogite and metagreywacke—Insights to late Ordovician–Silurian crustal folding events recorded in the Beishan Orogen (NW China). *J Metamorph Geol*. 2020;38:555–591. https://doi.org/10.1111/jmg.12531